

6-7-2019

Dynamics of Falling Droplet Under Effects of Electric Fields

Esmail Ghasemisahebi
eghas001@fiu.edu

Follow this and additional works at: <https://digitalcommons.fiu.edu/etd>



Part of the [Electro-Mechanical Systems Commons](#)

Recommended Citation

Ghasemisahebi, Esmail, "Dynamics of Falling Droplet Under Effects of Electric Fields" (2019). *FIU Electronic Theses and Dissertations*. 4262.
<https://digitalcommons.fiu.edu/etd/4262>

This work is brought to you for free and open access by the University Graduate School at FIU Digital Commons. It has been accepted for inclusion in FIU Electronic Theses and Dissertations by an authorized administrator of FIU Digital Commons. For more information, please contact dcc@fiu.edu.

FLORIDA INTERNATIONAL UNIVERSITY

Miami, Florida

DYNAMICS OF FALLING DROPLET UNDER EFFECTS OF ELECTRIC FIELDS

A dissertation submitted in partial fulfillment of the

Requirements for the degree of

DOCTOR OF PHILOSOPHY

in

MECHANICAL ENGINEERING

by

Esmail Ghasemisahebi

2019

To: Dean John L. Volakis
College of Engineering and Computing

This dissertation, written by Esmail Ghasemisahebi, and entitled Dynamics of Falling Droplet under Effects of Electric Fields, having been approved in respect to style and intellectual content, is referred to you for judgment.

We have read this dissertation and recommend that it be approved.

Yiding Cao

Norman Munroe

Ali Siahpush

Arif Sarwat

Cheng-Xian Lin, Major Professor

Date of Defense: June 07, 2019

The dissertation of Esmail Ghasemisahebi is approved.

Dean John L. Volakis
College of Engineering & Computing

Andrés G. Gil
Vice President for Research and Economic Development
and Dean of the University Graduate School

Florida International University, 2019

© Copyright 2019 by Esmail Ghasemisahebi

All rights reserved.

DEDICATION

I dedicate this thesis to my parents, sisters, and friends. Without their patience, understanding, support, and most of all love, the completion of this work would not have been possible.

ACKNOWLEDGMENTS

I wish to thank the members of my committee for their support, guidance and valuable suggestions. Here I will appreciate the time and dedication of Dr. Arif Sarwat from the Department of Electrical & Computer Engineering, Prof. Yiding Cao and Prof. Norman Munroe from the Department of Mechanical & Materials Engineering and Dr. Ali Siahpush from the Department of Engineering & Technology at Southern Utah University. My special thanks go to my major professor Dr. Cheng-Xian (Charlie) Lin for his constant support, time and guidance. I am also grateful for the financial support of the Florida International University for the Dissertation Year Fellowships. Finally, I want to extend my appreciation to all the faculty members and staff of the Department of Mechanical and Materials Engineering at Florida International University.

ABSTRACT OF THE DISSERTATION

DYNAMICS OF FALLING DROPLET UNDER EFFECTS OF ELECTRIC FIELDS

by

Esmail Ghasemiahebi

Florida International University, 2019

Miami, Florida

Professor Cheng-Xian Lin, Major Professor

Physical properties and especially the size of drops are important parameters in many industrial and medical applications. High voltage electric field is one of the effective means to control the final size of drops during the fabrication process which could greatly influence the quality of the product. Therefore a detailed study of electric field effect on a liquid drop is very important. In this work, the deformation and fragmentation of a falling droplet under gravity and electric forces have been studied numerically and analytically. The electric force is used as an effective external controlling mechanism to influence the deformation of a drop. The three-dimensional deformation of a falling droplet is studied numerically using an open-source volume-of-fluid solver, Gerris, with dynamic adaptive grid refinement and direct numerical simulation (DNS). The current numerical results are compared with previously published analytical and experimental data in the literature, and excellent agreements between the results are obtained. In addition, the numerical results are compared with the current analytical solution developed in this work. The results are presented for a broad range of Bond numbers (Bo) from low Bond numbers (drop with small deformation) to large Bond numbers (drop breakup and fragmentation). The results revealed that the electric field can be used as a powerful controlling tool in delaying and expediting the falling drop breakup process. The results also showed that falling drop deforms severely by increasing Bo number which

leads to the breakup and fragmentation as compared to the cases of low Bo number in which the drop deforms mildly without breakup. The numerical results are presented for various values of density ratios and electrical conductivity and permittivity. Within the investigated parameter ranges, the comparison of the results shows a great agreement between the analytical solutions and the direct numerical simulation (DNS) results.

TABLE OF CONTENTS

CHAPTER	PAGE
1 Chapter 1: Introduction to Falling Drop	1
1.1 Motivation and Hypothesis.....	1
1.1.1 Motivation	1
1.1.2 Hypothesis	3
1.2 Literature Review	3
1.3 Research objectives	8
1.4 Outline of the Dissertation.....	9
2 Chapter 2: Governing Equations	11
2.1 Numerical method	15
3 Chapter 3: Numerical Modeling and Validation	17
3.1 Problem definition and geometry	17
3.2 Numerical method	18
3.3 Grid Study.....	18
3.4 Validation of numerical results obtained by Gerris for fluid flow field	19
3.5 Validation of numerical results obtained by Gerris for the electric field	23
3.6 Numerical results for low Bo and Ga number	27
3.7 Numerical simulation for high Bo and Ga number	31
4 Chapter 4: Analytical Solution	36
4.1 Drops under electric field	37
4.2 Steady drop deformation.....	59
4.3 Transient droplet deformation:	66
4.4 Falling drops	73
5 Chapter 5: Coalescence of Two Falling Drops.....	90
5.1 Coalescence of two falling without electric field effects.....	90
5.2 Coalescence of two falling drops under electric field effects	91
5.2.1 Distance effects.....	91
5.2.2 Electric field strength effects	93
5.3 Near Wall Deformation of Falling Droplets under the Effect of Electric Field	94
6 Chapter 6: Conclusion and recommendations	99
6.1 Conclusion	99

6.2	Recommendations.....	102
	VITA.....	108

LIST OF TABLES

TABLE	PAGE
Table 1. Electrical properties related to Figure 20.	65
Table 2. The three studied cases (systems).....	72
Table 3. Analytical relationships obtained up to this section	78

LIST OF FIGURES

FIGURE	PAGE
Figure 1. The interface of two fluid mediums.	13
Figure 2. Schematic of the problem and the boundary conditions.	17
Figure 3. Grid independence study of the model for the falling drop; cross section at $t=3$	19
Figure 4. Comparison of current numerical results and previously published experimental data [38] for various values of Reynolds and Bond numbers.....	20
Figure 5. Comparison of current numerical results and previously published experimental data [38] for various values of Reynolds and Bond numbers.....	21
Figure 6 . Drop deformation for different density ratios for $Ga = 40$, $Bo = 5$ and $\mu_r = 10$	22
Figure 7. The computational domain for the study of the EHD deformation on the droplet.	23
Figure 8. Comparison of the numerical results and the theoretical prediction at conductivity ratio $C=5$	24
Figure 9. Comparison of the numerical results and the theoretical prediction when $Ca_E = 0.2$ and $Q= 2$	25
Figure 10. Drop deformation under effect of electric field (a) $Q=10$, (b) $Q=1$, and (c) $Q=20$ for $C=5$ and $Ca_E = 0.2$	26
Figure 11. Deformation of the drop for various values of electric capillary number at permittivity ratio $Q=5$	27
Figure 12. Effects of EHD on drop for, $Ga = 40$, $Bo = 5$ $Ca_E=0.11$, $\rho_r=2$, $\mu_r=10$ for (a) $Q=25$, $C= 5$ and (b) $Q=5$, $C= 15$ from $t=1$ to $t=6$	28
Figure 13. Effects of EHD on drop for, $Ga = 40$, $Bo = 5$ $Ca_E=0.11$, $\rho_r=5$, $\mu_r=10$ for (a) $Q=25$,	29
Figure 14 . Effect of EHD force on terminal velocity for $Ga = 40$, $Bo = 5$, $Ca_E =0.028$, $\rho_r =1.1$,.....	30
Figure 15 . Effect of EHD force on terminal velocity for $Ga = 40$, $Bo = 5$, $Ca_E =0.11$, $\rho_r =1.1$,.....	30
Figure 16. Initial deformation of the drop into bag shape for $Bo=98$, $Ga= 24$ and $\rho_r =10$	31
Figure 17. Time sequence deformation of the falling drop for $Ca_E =0.028$	35

Figure 18. Schematic of a droplet under electric field.....	36
Figure 19. Different areas associated with the deformation of the drop at a critical frequency.....	65
Figure 20. Deformation form with increasing frequency for different areas.	66
Figure 21. Total deformation function in terms of time for $R=100, \lambda = 0.1, a_w=1E4$,.....	71
Figure 22. Deformation rate of the field in two modes of zero and 60 (left) and deformation ratio at each frequency to deformation at a frequency of 60 (right).....	72
Figure 23. How to move the fluid around and inside the droplet for system 2 based on the increase of the dimensionless number W	84
Figure 24. Movement of fluid around and within the droplet for system 3 based on the increase of the dimensionless number W	86
Figure 25. Drop deformation in the two systems, effects of EHD and falling.	87
Figure 26. Comparison of the analytical solution calculated in this study against the current direct numerical solution using Gerris.....	88
Figure 27. The number of necessary series terms to reach the converted solution for the deformation function	89
Figure 28. The geometry for two drops.....	90
Figure 29. The coalescence of two falling drops without the electrical field effects.	91
Figure 30. The coalescence of two falling drops under electric fields at different distances from each other at $Ca_E = 0.4$ and $t=2$	92
Figure 31. The coalescence of two falling drops under electric fields at different distances from each other at $Ca_E = 0.4$ and $t=2$ to $t=6$	93
Figure 32. The coalescence of two falling drops under electric fields at different distances from each other at different electric fields, $d=0.5r$ and $t=2$ to $t=6$	93
Figure 33. The coalescence of two falling drops under different electric fields at $d=r$ and $t=4$	94
Figure 34. The schematic of the problem and the boundary conditions.....	95
Figure 35. The Effects of EHD on drop for, $Ga = 40, Bo = 5, Ca_E=0.11, \rho_r=2, \mu_r=10$ for (a) wall boundary condition applied and (b) $Q=25, C= 5$ from $t=1$ to $t=6$	96
Figure 36. The effects of EHD on drop for, $Ga = 40, Bo = 5, Ca_E=0.11, \rho_r=5, \mu_r=10$ for (a) for (a) wall boundary condition applied and (b) $Q=25, C= 5$ from $t=1$ to $t=6$	97

Figure 37. Deformation of the falling drop under (a) wall effect and no EHD force (b) EHD force98

ABBREVIATIONS AND ACRONYMS

Bo	Bond number
Ga	Gallilei number
Ca_E	Electric capillary number
C	Ratio of the inner to the outer conductivity
Q	Ratio of the inner to the outer permittivity
D	Analytical total deformation
\vec{t}	Tangent vectors to the free surface
\vec{n}	Normal vector with respect to the interface
\vec{E}	Electric field
p	Pressure (Pa)
\vec{F}_e	Volume electric force (N/C)
δ_s	Dirac delta
t	Time (s)
\vec{u}	Velocity vector (m/s)
$\overline{\overline{T}}$	Viscous stress tensor
$\overline{\overline{D}}$	Deformation tensor

Greek Letters

μ	Viscosity (Pa.s)
ρ	Fluid density (kg/m ³)
ρ_e	Volumetric charge density
λ	Ratio of the inner to the outer viscosities
\vec{J}	Vector current density
φ	Electric potential (V)
κ	Curvature
σ	Surface tension coefficient (N/m)

Subscripts or Superscripts

*	Provisional value
1	Liquid 1 (drop)
2	liquid 2 (outside medium)

1 Chapter 1: Introduction to Falling Drop

1.1 Motivation and Hypothesis

1.1.1 Motivation

As will be discussed and concluded in the literature review section, the main focus of many researchers on this subject was the drop deformation that is surrounded in a medium with a similar density in a stagnant form without considering the effect of gravity for the falling drop which in reality may be an important factor. To this date, a majority of the research is based on the development of empirical models and production of laboratory experimental results. The literature review reveals that there are very few mathematical models published and most of them are semi-empirical approaches for capturing and analyzing the drop deformation especially at the early stages of their deformations. Another challenge is related to how accurately the drop deformation is analyzed for a broad range of density and viscosity, which could be extremely lengthy and complex to be modeled if they are subjected to gravitational and electric fields.

Developing and implementing a numerical tool for modeling the drop deformation is always a significant challenge. This is because tracking a free surface that changes topology is a difficult task to accomplish for an accurate investigation and analysis of an underlined two-phase flow. Multiphase flow, including atomization, has significant applications in science and engineering and plays an important role in a broad range of industries such as aeronautics applications (rockets and aircraft), automotive engineering, pharmaceutical industry, power generation, petro-chemical industry, manufacturing, agriculture and meteorology. Although atomization is widely used and drives the performance of many systems, characterizations of the spray produced still require more detailed research in terms of size and dispersion. Since the prediction of fuel sprays in gas turbines is of critical importance for aero-engine manufacturers to improve the injection process, implementing a mechanism that maximizes the combustion efficiency and reduce the aviation

emissions is very significant. Other concerns are the fuel-air mixing as well as emissions of greenhouse gas and its effect on global warming. As the production of NO_x and CO₂ in gas turbines is affected by the fuel-air mixing in combustion chambers, aero-engine manufacturers are facing challenges finding a tool to reduce the emissions of greenhouse gas through the optimization of the fuel injection. The fuel-gas mixing is primarily driven by the atomization that involves both the initial fragmentation of the bulk liquid into droplets (primary breakup) and the transport and further fragmentation of the drops (secondary breakup). Whereas the secondary breakup is fairly well predicted by the current numerical methods, the accurate simulation of the droplet still remains one of the toughest challenges in computational fluid dynamics (CFD).

Motivated by the limits of existing analytical and numerical methods, in this dissertation an accurate numerical method in CFD will be implemented to capture and predict the two-phase flow nature of drop deformation under both gravitational and electric fields. It is expected these fields will have a significant effect on the shape and location of the droplets. In this work, to analyze and study the real world problem the dynamics of the drop fragmentation have been investigated under gravitational force wherein almost all the application such as fuel injection, metal coating and 3D printing, the droplet is moving and is not stagnant (surrounded by a medium with the same density). The gravitational and electric forces have been implemented in DNS solution to model the real-life physical phenomena to study the behavior of the droplet. It is expected that, under gravitational force, the droplet undergoes various deformations before it eventually reaches fragmentation and is converted to much smaller drops. Moreover, a practical and comprehensive analytical model for the assessment of small deformation of the droplet will be developed for a much quicker way of predicting the drop deformation rather than relying on a complicated, expensive and time consuming experimental work. This analytical solution for a falling drop under electric field provides an excellent tool for faster and easier prediction of the small drop deformation. With an accurate CFD modeling using the capability of a powerful numerical tool such as DNS, the

aeronautical industry would not have to rely solely on comprehensive and expensive experimental test apparatus and thus the design of efficient devices would be more cost-effective. Also, with the recent progress in experimental measurements of the multiphase flows, the combination of the numerical tool with the experimental approach would allow the manufacturers to improve the combustion efficiency. The research of this dissertation would address significant concerns and challenges regarding the quality of fuel sprays in gas turbines to maximize the combustion efficiency, reduce aviation emissions, and related the emissions of greenhouse gases, and lower the fuel consumption, by boosting the fuel-air mixing in combustion chambers.

1.1.2 Hypothesis

In dealing with the above crucial concerns and challenges, it is hypothesized that the size of the drops and their dispersion can be optimized and improved by an auxiliary mechanism such as an extra force imposed on the fluid flow system. It is also hypothesized that an external force such as an electric force can be an applicable controlling mechanism to impact the drop deformation. Preliminary research and case studies of this dissertation have supported the hypothesis by comparing the data of the preliminary study with some previously published experimental work. Another hypothesis is that DNS modeling is a powerful numerical tool to model the drop deformation in the present studies.

1.2 Literature Review

As noted above, the physics and particularly the dynamics of two-phase flow have grown into a major scientific domain with crucial fundamental issues as well as many practical and industrial applications. Fields of interest include drop impact phenomena involved in the study of rain on soils or foliage, inkjet printing and combustion chambers. In particular, atomization processes play an important role in combustion studies. In-depth understanding of physics and dynamics of multiphase flow and in particular two-phase flow is very crucial due to its broad and practical

applications in science and industry and also because of its complexity in scientific research with essential fundamental issues. These applications include atomization in the aerospace industry for modeling the fuel injection in combustion chambers over the gas turbine, different types of combustion processes, drug delivery inside the body, engines with diesel fuels, ink-jet coating process, spray painting and drying, microfluidic applications, heat exchangers evaporation-based, desalination, emulsification, etc. Taylor [1] studied a drop in a fluid field with high velocity to investigate the drop shape and its acceleration. The results showed that equilibrium can only be established in a drop when circulations are set up both in the drop and its surroundings; moreover, his results found a relation between the ratios of the conductivity, viscosity and dielectric constant for the drop and surrounding fluid which permits the drop to remain spherical when subjected to a uniform field. Pilch and Erdman [2] studied the size of a drop during breakup which was influenced by acceleration using the data for the time during which breakup occurs and also the history of the data for velocity. Hinze [3] studied the dispersion procedures to investigate the hydrodynamic principals for particle splitting in which he found out that the splitting of globules is an important phenomenon during the final stages of disintegration processes. Giffen E and Muraszew [4] studied the liquid fuel atomization and Faeth et al. [5] investigated the structure and breakup of sprays. Villermaux [6] thoroughly studied the atomization process and examined the drop, jets and liquid sheets fragmentations and bursting phenomena. Contrary to a lot of studies on drop deformation, very few studies have been done on a mechanism to control the drop behavior. One of these methods is applying an external force such as the electric field. A drop suspended in a viscous liquid undergoes complicated behaviors such as abrupt transitions, breakup, deformation which depends on the magnitude of the electric field and also the properties of the fluids such as surface tension, electrical conductivity, viscosity, and permittivity. Electrohydrodynamics (EHD) field is used as an effective external controlling force to influence the drop's deformation in order to have a much better and more efficient distribution due to their importance in atomization, raindrop size

distribution many other problems of industrial importance. EHD is a multidisciplinary subject that deals with the complicated interaction between fluid mechanics and electric fields in which the coupling between electrostatic and hydrodynamic forces are studied. Melcher [7] provided a thorough review of electrohydrodynamics. EHD can improve the control over spray mechanism to have a much better and finer atomization which is significantly important for the small compact combustion engines and therefore the fuel injection schemes can be developed economically at a much lower price. EHD increases the heat and mass transfer rates and is implemented in inkjet printing and electrowetting which is a driving mechanism for a wide range of fluidic and electro-optic applications for modifying the surface tension of liquids on a solid surface. EHD efficiently improves the atomization of the hydrocarbon fuel which benefits a much wider range of engines and other types of non-combustion applications in the pharmaceutical industry, such as pharmaceutical coating and micro/nano-thin-film deposition. Ryan et al. [8] studied that EHD atomization enhances the breakup of liquid fuel at lower pressures which produce high-quality atomization in which there is no more fuel injection at high pressure required. Bio-fuels are one of the alternatives to the diesel with higher viscosity and water content that requires high pressures to atomize the fuel in the combustion chamber; because of that larger and less efficient engines are required for these types of fuels. EHD atomization is an applicable method for use in small combustion engines which reduces the high fuel injector pressures required by these engines to atomize the bio-oils fuels with high viscosity [9]. Another advantage of the enhancement of the fuel atomization is to more likely have complete combustion during the burn cycle resulting in a better burning and less emission[10]. Moreover, the electric fields in the engine exhaust direct the burn residue such as soot, NO_x to easily cleanable containers as the EHD atomization keep these residues charged[11]. Paknemat et al. [12] studied the effect of electric field on three different types of the drop using a level set method. They conducted their numerical results for a different range of capillary number to observe different modes of breakup under the effect of the DC electric field.

Notz and Basaran [13] numerically investigated the effect of electric field on the formation and deformation of a perfectly conducting drop from a capillary. After validation of their results with the previous analytical and experimental works, they have studied the effect of an electric field with variable strength for the zero-flow rate case. They showed that for small values of change in the strength of the electric field the results of transient calculations are in a good agreement with the previous works. Jung et al. [14] numerically studied the deposition of droplets from a spray under the effect of an electric field. They used a three-dimensional Lagrangian model to study the application of electric fields on the characteristics of deposition pattern such as the spatial distribution and the average thickness distribution. The results of simulations showed that in general for the case with the electric field the deposition thickness in the intervening region of spray is less than the core region for all the control parameters such as moving speed of the nozzle. Van Poppel et al. [15] numerically studied the EHD effect on a high Reynolds number (Re) multiphase regime of a liquid kerosene jet. They used a fully three-dimensional model to simulate the atomization process of a charged liquid jet and compared their results with the previous data. López-Herrera et al. [16] developed a conservative scheme for electrohydrodynamic (EHD) of two-phase problems incorporating the Volume-of-Fluid (VOF) method. They implemented their scheme in a free and open-source software Gerris. They also compared the results obtained from the proposed scheme with the available analytical solution for droplet surrounded by conducting environment which showed a great agreement between the outcomes. Baygents et al. [17] studied the motion of two leaky dielectric drops under the effect of a uniform electric field. They observed a significant deformation near drop contact because of the local enhancement of the electric field. The deformation and burst of the drop are caused by electrical stresses at the drop surface due to the difference between the dielectric properties of the fluids. Up to the pioneering studies by Taylor [18], it was commonly perceived that the fluids are either infinitely conducting or perfect dielectric (insulator). According to the electrostatic theory in either case of infinitely conducting or perfect

dielectric drop suspended in a surrounding perfect dielectric, the net electric stresses at the interface are normal to the interface pointed from the fluid with higher conductivity or permittivity to the one with lower mentioned properties; in this case the drop takes the prolate (large deformation in electric field direction) form due to distribution of these stresses. There is no fluid flow exists at steady state as inequality in tangential electric stresses is excluded in electrostatic theory. Allan and Mason [19] did an extensive experimental study for a broad range of fluid systems in which they showed that conducting drops took the prolate form while some other dielectric drops deformed into oblate (large deformation direction in the perpendicular direction to the electric field) shape. Later, inspired by similar observations of Allan and Mason [19], Taylor [18] mentioned that the fluids should be given finite permittivity and conductivity instead of considering them as either perfect dielectrics or perfect conductors for the free charge gathering at the interfaces of fluid. The effect of electric field on this charge results in unbalance normal and tangential stresses which leads to oblate deformation. At equilibrium, the hydrodynamics stresses have to be balanced by the imbalance in the electrical shear stresses and therefore fluid motion forms inside and outside of the drop due to the hydrodynamic shear stresses. From then on, Taylor's theory has been known as the leaky dielectric theory. By using this theory, Taylor could explain the experimental data of Allan and Mason [19] by solving the electrohydrodynamic equations for the creeping flow. Although, further experimental results obtained by Torza et al. [20] revealed some disagreements between the theory and the experimental data. This theory has been improved by including the higher order terms to Taylor's linearized theory by Ajayi [21]. The electrokinetic effects issue stated by Torza et al. [20] has been investigated by Baygents et al. [22] by replacing the leaky-dielectric model by an electrokinetic one but these modifications did not improve the deformation of the drop significantly. These outcomes demanded more experimental studies by Vizika and Saville [23] to carry out new sets of experimental investigations for obtaining the data in closer agreements with the theory. In spite of existing some discrepancy, generally, it is considered that the theory of leaky-

dielectric is the correct “lumped-parameter” model when there is no net charge the drop [23]. The interest in this topic rooted from the raindrops breakup and deformation [24] and the aerosol deformation effect on optical studies [25]. This interest increased over time due to its various important applications in chemical engineering [26], nuclear physics [27], materials processing [28]. Recently this interest is in the area of microfluidic systems such as liquid jets atomization influenced by electric field in inkjet printing [29], controlling the drop breakup in electrowetting [30], electrorheological fluids [31], pharmaceutical industry, such as pharmaceutical coating and micro/nano-thin-film deposition and improvements of the atomization of the hydrocarbon fuel and many more. Study of stability and deformation of a drop under electric field is therefore an important and ongoing research area. Melcher and Taylor [32] and other researchers [33] and [34], provided a thorough review of governing electro-hydrodynamics laws and their solution for planar interface separating two fluids, a suspended drop in quiescent and creeping flows

1.3 Research objectives

As explained above, detailed knowledge of the droplet’s dynamics and behavior is significant for industrial applications. In this work, the Direct Numerical Simulation (DNS) method using Gerris has been used which can model the droplet break up in detail without any simplification in the physics of the problem. And also for having more optimized and efficient droplet’s distribution, the EHD force has been applied on the falling droplet to be able to control the droplet’s dynamics for better and optimized dispersion. Literature review shows that very few researches have been conducted on complete CFD based simulation of the droplet in detail for various wide ranges of density and viscosity under the electric field. In this research, we will study the dynamics of a droplet in details and the controlling of its behavior by applying the electric field. The main objectives of the present research are controlling the dynamics of a falling droplet by implementing EHD force that incorporated into the fluid flow equations as an external force. The EHD as an

external force has been implemented to the open-source volume-of-fluid solver, Gerris, using direct numerical simulation (DNS). Extensive case studies have been performed using different turbulent CFD models in order to come up with a powerful numerical tool that is able to simulate this complicated problem precisely by other researchers. However, turbulence modeling is a big challenge. Another concern regarding modeling the EHD flows with a proper CFD model is the number of grids and computational time which must be considered methodically. A thorough case study examining different CFD models considering their meshing algorithm and computational time has been done. It has been shown that it is possible to use DNS that has the dynamic adaptive grid refinement feature providing a notable reduction of computational cost for controlling the drop behavior.

In this work, an analytical solution of falling drops under the effect of electric field has been provided and the results have been compared with our numerical DNS data for verification and validation. Validation of the current numerical results of EHD field and falling drop have been investigated by comparing the data with the previously published analytical, experimental and numerical solutions in the literature. In addition the numerical results are also compared with the present analytical solution developed in this work.

1.4 Outline of the Dissertation

The remaining chapters of this dissertation are organized as follow:

- In chapter 2 governing equations of the incompressible fluid flow are described along with numerical methods
- Chapter 3 presents the numerical modeling and validation, definition of the problem studied in this work, explanation of the computational domain and the grid independence study for the falling droplet. Moreover, the validation of numerical results obtained by Gerris for fluid flow and electric fields has been explained.

- In chapter 4, analytical solutions of the problem have been provided in detail for a variety of cases.
- In chapter 5, the coalescence of two falling drops for cases in which the drops are affected with and without external electric fields is provided. Moreover the effects of distances that separated the two drops and also the strength of the electric field have been investigated on the coalescence of the drops. At the end of the chapter the near wall deformation of falling droplets under the effect of the electric field has been studied.
- Chapter 6 presents a summary of the dissertation and the conclusions.

2 Chapter 2: Governing Equations

The continuity and momentum equations of incompressible fluid flow are,

$$\nabla \cdot \vec{u} = 0, \quad (1)$$

$$\rho(\partial_t \vec{u} + \vec{u} \cdot \nabla \vec{u}) = \nabla p + \nabla \cdot (\overline{\overline{T}}) + \sigma \kappa \delta_s \vec{n} + \vec{F}_e \quad (2)$$

where $\vec{u} = (u, v, w)$ is the velocity vector, and $\rho = \rho(\vec{x}, t)$ and $\mu = \mu(\vec{x}, t)$ are the local fluid density and dynamic viscosity, respectively. $\overline{\overline{T}} = 2\mu \overline{\overline{D}}$ is the viscous stress tensor in which $\overline{\overline{D}} = D_{ij} = (\partial_i u_j + \partial_j u_i)/2$ is the deformation tensor. The Dirac delta δ_s states the fact that the surface tension term is concentrated on the interface. σ is the surface tension coefficient, while κ and \vec{n} are the curvature and normal vector with respect to the interface, respectively. Maxwell's electromagnetic equations are required to calculate volume electric force, which is \vec{F}_e . In EHD flows, as mentioned by Saville [33], the equations for electrostatic gives an accurate approximation and the effects of the magnetic field is ignored. The characteristic time for the magnetic phenomena $t_m \propto \mu_M K \ell^2$ where μ_M is the magnetic permeability, K is the conductivity and ℓ the characteristic length. This time is many order of magnitude smaller than the electric relaxation time $t_e \propto \varepsilon/K$. The relaxation time is the characteristic time for electric phenomena where ε is the electric permittivity. Thus we have:

$$\rho_e = \nabla \cdot (\varepsilon \vec{E}) \quad (3)$$

The electric field \vec{E} is assumed to be irrotational. $\nabla \times \vec{E} = 0$. In this equation E is the electric field, where ρ_e is the volumetric charge density. In terms of the electric potential, ϕ gives

$$\nabla \cdot (\varepsilon \nabla \phi) = -\rho_e \quad (4)$$

The bulk-free charge should be implemented for the conservation equation of the,

$$\frac{\partial \rho_e}{\partial t} + \nabla \cdot \vec{J} = 0 \quad (5)$$

where J is electric charge flux defined as:

$$\vec{J} = K\vec{E} + \rho_e \vec{u} \quad (6)$$

The ohmic charge conduction is the first term and the second term is from convection of charges.

Considering the Eq. (3), Eq. (5) can be written as

$$\frac{\partial \rho_e}{\partial t} + \nabla \cdot (\rho_e \vec{u}) = -\frac{K}{\varepsilon} \rho_e + \vec{E} \cdot \left(\frac{K}{\varepsilon} \nabla \varepsilon - \nabla K \right) \quad (7)$$

For homogeneous K and ε , it gives

$$\frac{\partial \rho_e}{\partial t} + \nabla \cdot (\rho_e \vec{u}) = -\frac{K}{\varepsilon} \rho_e \quad (8)$$

The electrostatic Maxwell stress tensor is used to calculate the volumetric electric forces in the bulk \vec{F}_e .

$$\vec{T}_e = \varepsilon \left(\vec{E}\vec{E} - \frac{E}{2} \vec{I} \right) \quad (9)$$

Implementing divergence operator gives

$$\vec{F}_e = \nabla \cdot \vec{T}_e = \rho_e \vec{E} - \frac{1}{2} (E^2 \nabla \varepsilon) \quad (10)$$

The first term presents the electric forces applied on the free charges in fluid, and the electric forces applied on the electric dipoles induced in dielectric mediums is the second term. Figure 1 shows the two-phase flows, media 1 and 2, where the interface separates the immiscible mediums.

$$\|p\| + \vec{n} \cdot \left\| \overline{\overline{T_v}} \right\| \cdot \vec{n} + \vec{n} \cdot \left\| \overline{\overline{T_e}} \right\| \cdot \vec{n} = \sigma \kappa. \quad (14)$$

On the interface, the pressure discontinuous and this is because of the normal components of the electric stresses and also the surface tension. On the interface, $E_n = \vec{E} \cdot \vec{n}$, the normal electric field, is also not continuous

$$\|\varepsilon E_n\| = q \quad (15)$$

where q stands for the gathering of free charge on the interface (charge/unit area). Following equation expresses the tangent component of electrical stress on the interface

$$\vec{t} \cdot \left\| \overline{\overline{T_e}} \right\| \cdot \vec{n} = (\varepsilon_1 E_{n1} - \varepsilon_2 E_{n2}) E_t = q E_t \quad (16)$$

And the normal component on the interface

$$\vec{n} \cdot \left\| \overline{\overline{T_e}} \right\| \cdot \vec{n} = \frac{1}{2} [\varepsilon_1 E_{n1}^2 - \varepsilon_2 E_{n2}^2 - (\varepsilon_1 - \varepsilon_2) E_t^2] \quad (17)$$

Following equation satisfies the charge density q

$$\frac{\partial q}{\partial t} + \vec{u} \cdot \nabla_s q - q \vec{n} \cdot (\vec{n} \cdot \nabla) \cdot \vec{u} + \|KE_n\| = 0 \quad (18)$$

The 2nd term is surface charge convection, surface divergence is shown by ∇_s , the 3rd term is the dilation of the interface and the last term shows how ohmic conduction adds a net charge to the bulk or withdraws the net charge from the bulk.

2.1 Numerical method

For the numerical solution an open-source solver is used for modeling of the incompressible fluid motion. This software is called Gerris which uses the finite volume method. Popinet [35] and [36] developed the software that implements the Volume of Fluid (VOF) method for simulation of the two-phase fluid flows. Using the VOF method the Navier-Stokes equations give

$$\begin{aligned}
\nabla \cdot \vec{u} &= 0, \\
\rho(\partial_t \vec{u} + \vec{u} \cdot \nabla \vec{u}) &= \nabla p + \nabla \cdot (2\mu \vec{D}) + \sigma \kappa \delta_s \vec{n} + \rho g + \vec{F}_e \\
\partial_t c + \nabla \cdot (c \vec{u}) &= 0, \\
\rho(c) &= c \rho_i + (1-c) \rho_o \\
\mu(c) &= c \mu_i + (1-c) \mu_o
\end{aligned} \tag{19}$$

where c stands for volume fraction, $c(\vec{x}, t)$. For the surface tension stress, the Continuum-Surface-Force (CSF) method [37] is implemented.

Second order staggered-in-time discretization combined with a time-splitting projection method is used in Gerris. Time stepping is

$$\frac{c_{n+1/2} - c_{n-1/2}}{\Delta t} + \nabla \cdot (c_n \vec{u}_n) = 0 \tag{20}$$

$$\frac{(\rho_e)_{n+1/2} - (\rho_e)_{n-1/2}}{\Delta t} + \nabla \cdot [(\rho_e)_n \vec{u}_n + K_{n-1/2} \vec{E}_{n-1/2}] = 0 \tag{21}$$

$$\nabla \cdot [\nabla (\varepsilon_{n+1/2} \Phi_{n+1/2})] = -(\rho_e)_{n+1/2} \tag{22}$$

$$\begin{aligned}
\rho_{n+1/2} \left(\frac{\vec{u}_* - \vec{u}_n}{\Delta t} + \vec{u}_{n+1/2} + \nabla \vec{u}_{n+1/2} \right) &= \nabla \cdot \left(\mu_{n+1/2} (\vec{D}_n + \vec{D}_*) \right) \\
+ (\sigma \kappa \delta_s \vec{n})_{n+1/2} &+ (\vec{F}_e)_{n+1/2}
\end{aligned} \tag{23}$$

$$\vec{u}_{n+1} = \vec{u}_* - \frac{\Delta t}{\rho_{n+1/2}} \nabla p_{n+1/2} \tag{24}$$

$$\nabla \cdot \vec{u}_{n+1} = 0 \quad (25)$$

* shows the provisional variables. If the Eq. (24) combine with Eq. (25), they result in

$$\nabla \cdot \left(\frac{\Delta t}{\rho_{n+1/2}} \nabla p_{n+1/2} \right) = \nabla \cdot \vec{u}_* \quad (26)$$

Therefore the Eq. (23) can be written gives:

$$\begin{aligned} \frac{\rho_{n+1/2}}{\Delta t} \vec{u}_* - \nabla \cdot (\mu_{n+1/2} \vec{D}_*) = \\ \nabla \cdot (\mu_{n+1/2} \vec{D}_n) + (\sigma \kappa \delta_s \vec{n})_{n+1/2} + (\vec{F}_e)_{n+1/2} + \rho_{n+1/2} \left(\frac{\vec{u}_n}{\delta t} - \vec{u}_{n+1/2} \cdot \nabla \vec{u}_{n+1/2} \right) = \end{aligned} \quad (27)$$

The expression $\vec{u}_{n+1/2} \cdot \nabla \vec{u}_{n+1/2}$, advection velocity, is calculated by [36].

3 Chapter 3: Numerical Modeling and Validation

3.1 Problem definition and geometry

Figure 2 shows the computational domain used in the current work along with the boundary conditions. The dimensions of the domain and drop are shown in the figure. The width of the computational domain is $40R$ with the height of $160R$ and R is the radius of the drop. A spherical droplet with density and viscosity of ρ_1, μ_1 and radius R falls under the action of gravity g . The initial velocity of the drop is zero. The surrounding medium has a viscosity of μ_2 and density of ρ_2 . Index 1 refers to drop and 2 is for the outside medium. The initial location of the drop and also the size of the computational domain are considered such that the boundaries have a negligible effect on the falling droplet break-up process. Symmetry boundary conditions are applied on the boundaries and the drop falling down under effects of external EHD force which has been applied on the side boundaries.

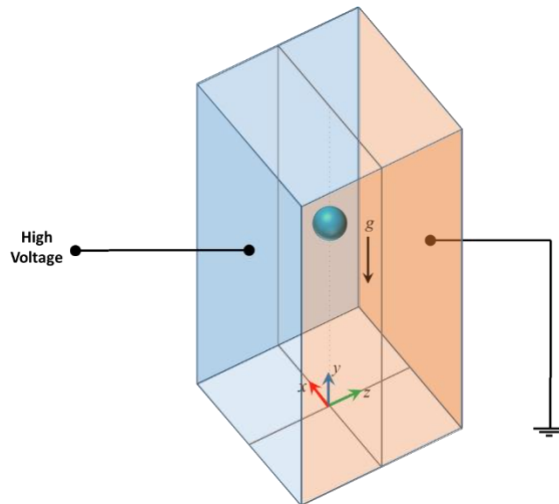


Figure 2. Schematic of the problem and the boundary conditions.

3.2 Numerical method

The open-source solver Gerris has been used [35] and [36]. The VOF is combined with an adaptive quad/octree spatial discretization in Gerris for solving the two-phase incompressible fluid flows. The numerical code solves the governing equations, combining a quad/octree spatial discretization, a projection method, and a multilevel Poisson solver. Advection terms are discretized using the robust second-order upwind scheme. For more detailed the readers are referred to Popinet [35] and [36].

3.3 Grid Study

Figure 3 shows the grid independence study for the falling droplet for three different grid levels of 9, 10 and 11 [35] and [36]. The figure shows the cross-sectional of 3-D drop at $t=3$. The initial grid level is 6 which means Gerris initially creates a regular Cartesian grid with cells in each dimension. The levels 9, 10 and 11 are the maximum refinements of the grids near the interface. The smallest grid size is equal to $1/8$, $1/16$ and $1/32$ of the initial grid for grid levels of 9 (coarse), 10 (medium) and 11 (fine), respectively. It is concluded that grid convergence is achieved for simulations having the medium grid level of 10. Thus all the three-dimensional simulations have been conducted using this grid size. And the non-dimensional time and velocity are $\tilde{t} = (V/R)t$, $\tilde{V} = V/\sqrt{gR}$.

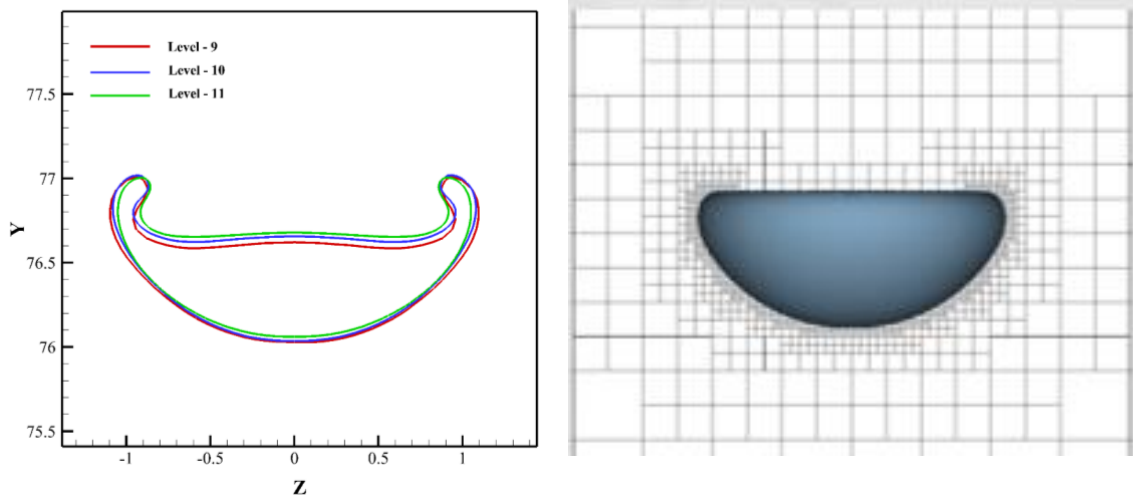
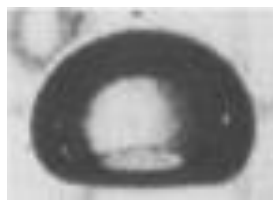


Figure 3. Grid independence study of the model for the falling drop; cross section at $t=3$.

3.4 Validation of numerical results obtained by Gerris for fluid flow field

Presented in Figure 4, the numerical results have been compared with previously published experimental data [38] for bubble deformation as shown in Figure 4. The results show the bubble deformation for different values of Bond and Reynolds numbers and for more detail the readers are referred to [38]. The results shown here are just for the purpose of the validation of the current numerical solution against previously published experimental data [38].



$$Bo^* = 116, Re^* = 6.546$$

(a)



$$Bo^* = 116, Re^* = 8.748$$

(b)

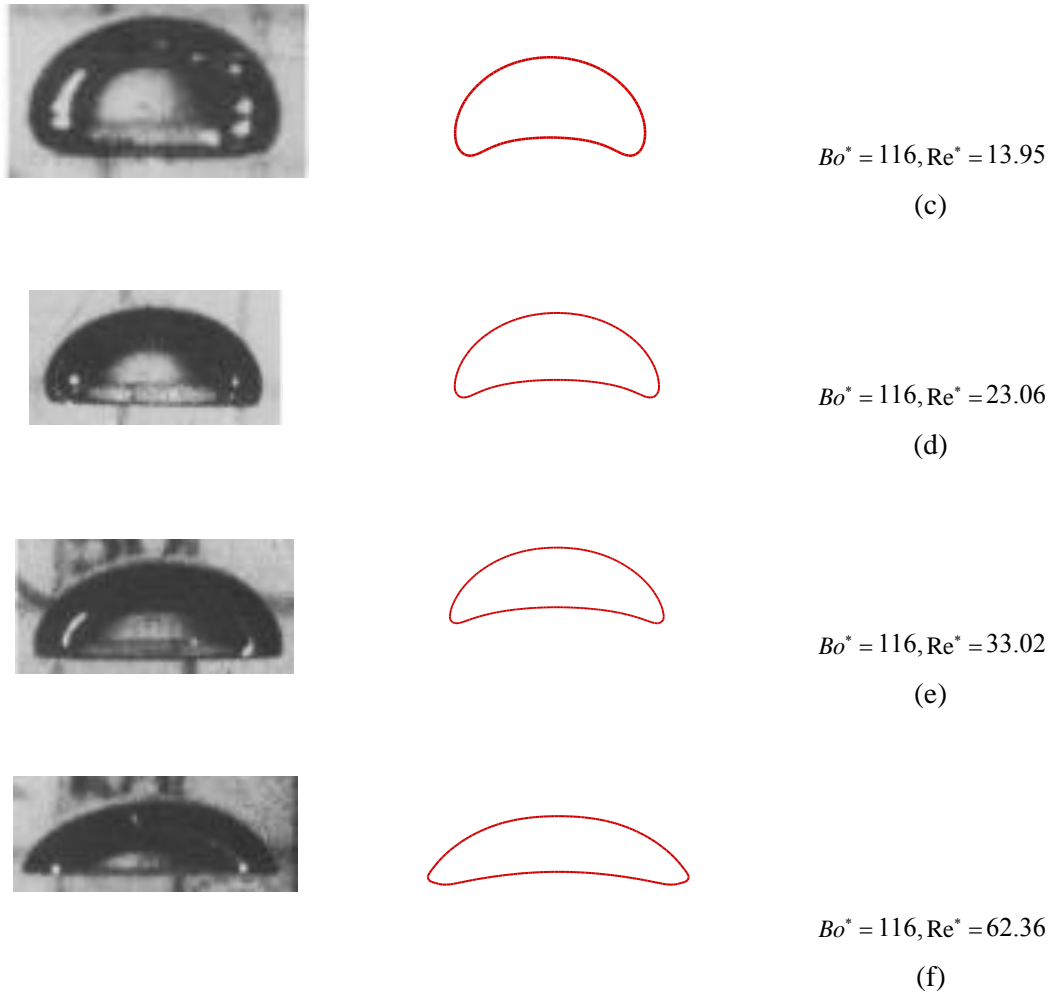


Figure 4. Comparison of current numerical results and previously published experimental data [38] for various values of Reynolds and Bond numbers.

Also in Figure 5 more comparison between the current numerical results obtained by Gerris and the previously published experimental data [38]. Here the results are presented for different Re and Bo numbers. As the figure shows there is a good agreement between the results qualitatively which confirms the accuracy of the current numerical model by Gerris.

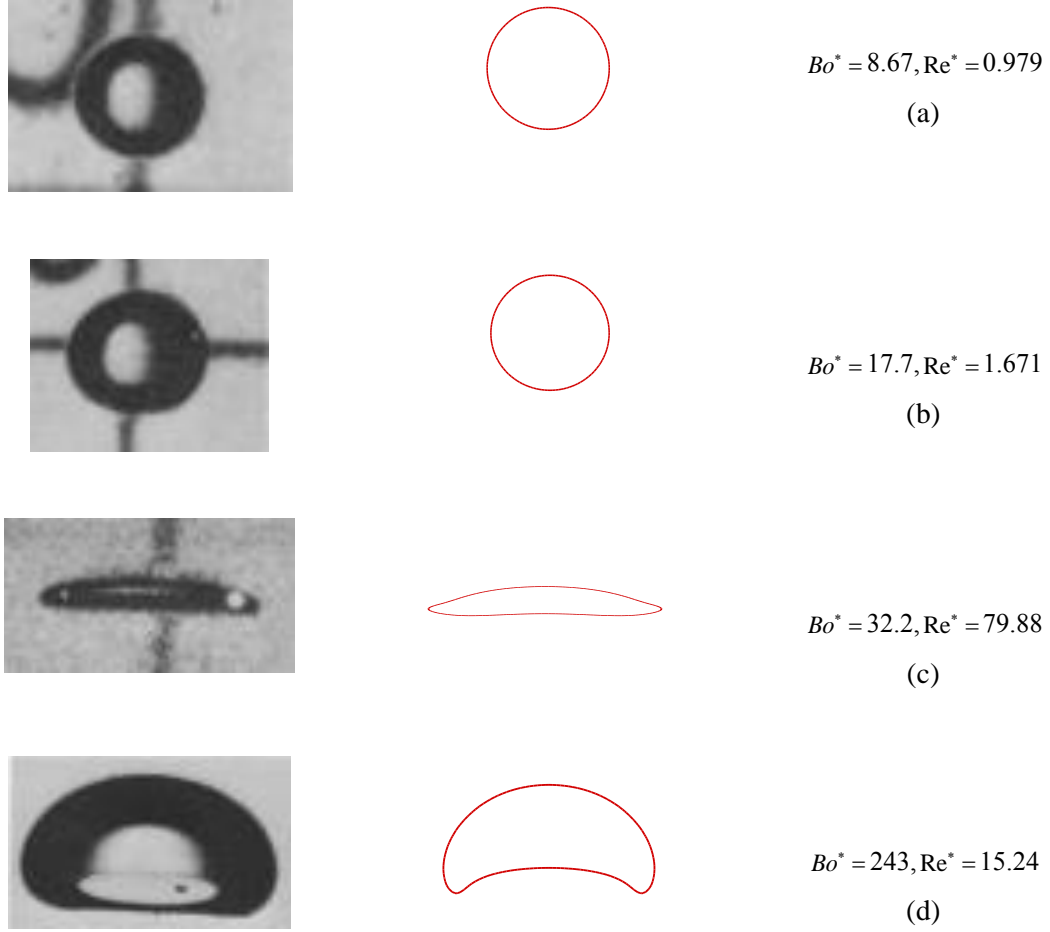
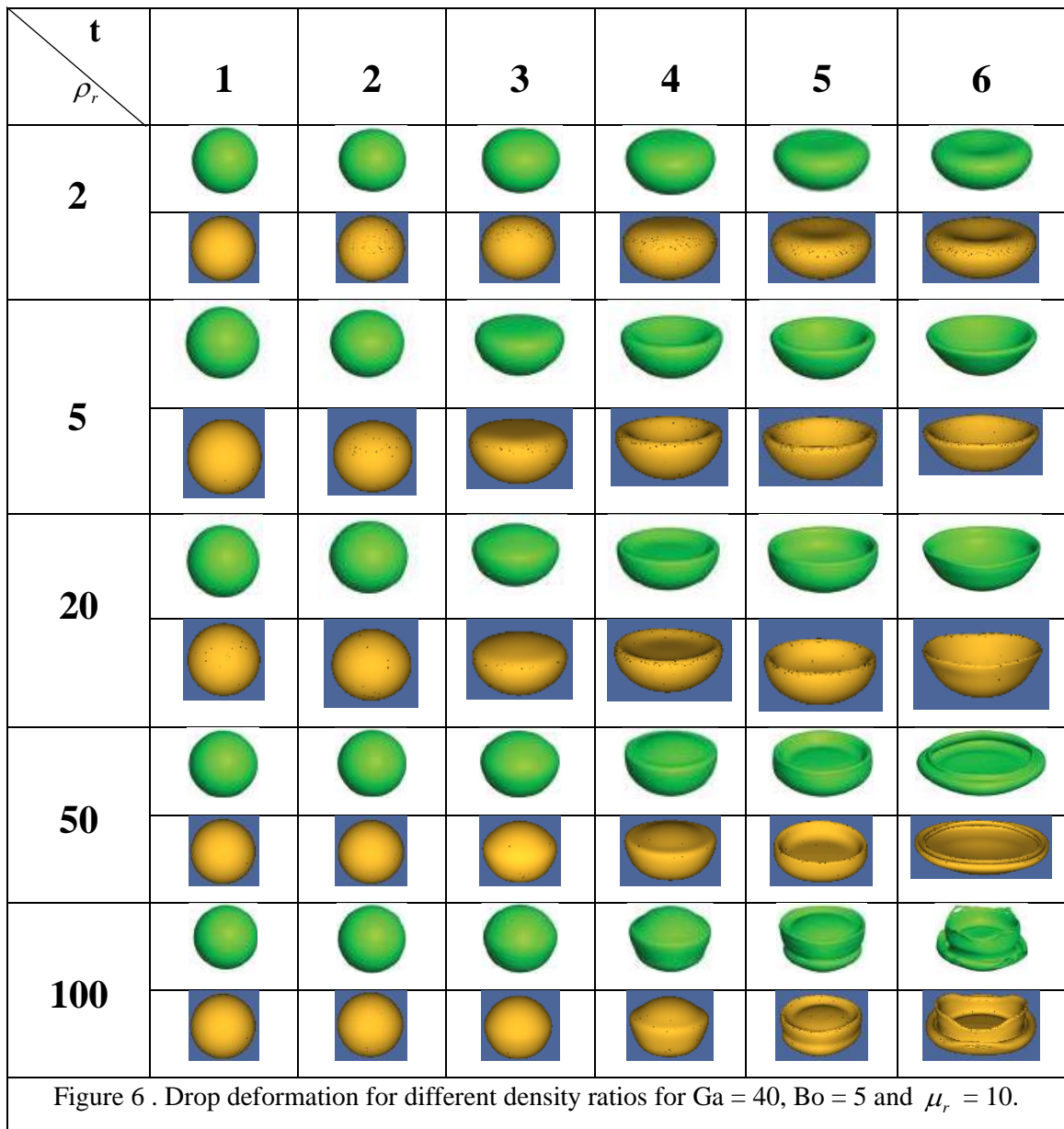


Figure 5. Comparison of current numerical results and previously published experimental data [38] for various values of Reynolds and Bond numbers.

The validity of the numerical results is also studied by comparison of the current results (yellow color) for drop deformation with those by [39] (green color) shown in Figure 6. Results show the drop deformations for a broad range of density ratios for Bond number, $Bo = \rho_o g R^2 / \sigma$ of 5 and the Gallilei number, $Ga = \rho_o R^{3/2} g^{1/2} / \mu_o$ of 40. The results are in excellent agreement with previous results obtained in [39]. As it is shown in the table, the drop remains almost spherical at low ratios of density but it deforms into a dimpled ellipsoidal shape for slightly greater density ratios. The drop tends to take an upward opening cup-like structure for higher values of density ratio. At density ratios $\rho_r = \rho_i / \rho_o$ approximately higher than 20, the surrounding medium tends to

shear off a thin portion of the drop resulting in a thin skirt-like structure which originates from drop periphery. This shearing might happen over the surface of the drop at several locations, resembling a Kelvin-Helmholtz like instability which is more noticeable at greater density ratios ρ_r . For the values of density ratios of 100 or larger, a severe breakup might happen to result in multiple drop fragmentations. These regimes might change which is dependent on other parameters such as Ga, Bo and $\mu_r = \mu_i / \mu_o$.



3.5 Validation of numerical results obtained by Gerris for the electric field

In this section, the numerical results obtained by Gerris for electric field is validated against the analytical data. As shown in Figure 7 the spherical drop either transforms into prolate or oblate depending on properties of the involved fluids as stated by Hua et al. [40]. Liquid 1 and liquid 2 refer to drop (i) and medium (o) respectively.

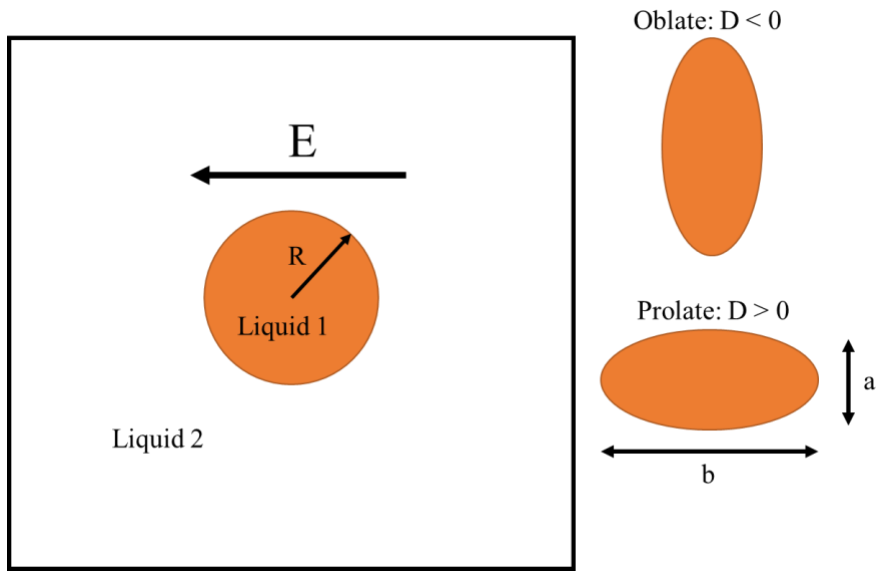


Figure 7. The computational domain for the study of the EHD deformation on the droplet.

Taylor [41] characterizes the total deformation of the droplet by

$$D = \frac{b - a}{a + b} \quad (28)$$

where, b and a are the sizes of the spherical in parallel and perpendicular directions to the electric field respectively. $D > 0$ represents the prolate spheroids while $D < 0$ shows the oblate. Taylor [41] also gave the following equation for D :

$$D = \frac{9}{16} \frac{Ca_E}{(2+C)^2} \left[1 + C^2 - 2Q + \frac{3}{5} (C-Q) \frac{2+3\lambda}{1+\lambda} \right] \quad (29)$$

where $C = \sigma_i/\sigma_o$, $Q = \varepsilon_i/\varepsilon_o$ and $\lambda = \mu_i/\mu_o$ represent the ratio of the inner to the outer conductivities, permittivities and viscosities, respectively. Ca_E is the electric capillary number $Ca_E = E_\infty^2 R \varepsilon_o / \sigma$.

In Figure 8 the numerical results have been compared to Taylor's deformation theory for different permittivity ratios. The numerical results are in good agreement with the analytical data, especially for the region when the droplet deformation is small (Taylor's theory is valid in this region). For large deformations, the numerical results start to deviate from the analytical data, in agreement with previous numerical studies in [40] and [42]. Saville [33] mentioned that for deformations $|D| > 0.07$ numerical results are more accurate than Taylor's theory.

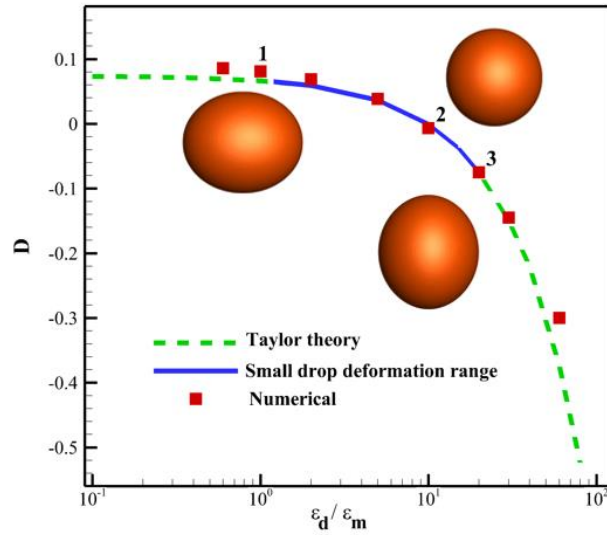


Figure 8. Comparison of the numerical results and the theoretical prediction at conductivity ratio $C=5$.

Figure 9 shows a comparison of the deformation predicted in the numerical simulation and analytical results by Taylor’s theory. For a conductivity ratio of $C=1$, the deformation is nearly zero.

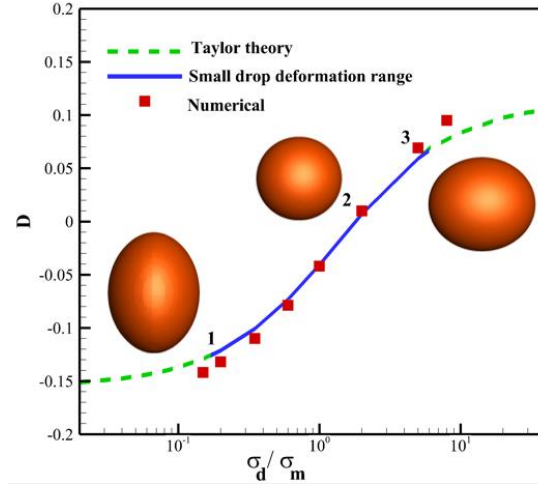


Figure 9. Comparison of the numerical results and the theoretical prediction when $Ca_E = 0.2$ and $Q=2$.

Figure 10 shows the streamlines (Red) and the velocity vectors (Black) for the droplet shape for different permittivity ratios. Figure 10a shows the results for the permittivity ratio of $Q = 10$. At this ratio, drop takes a prolate form. As the permittivity of the droplet increase its shape changes to an oblate form, and for a permittivity ratio of $Q = 1$ the droplet stays almost undeformed as shown in Figure 10b. As can be seen in Figure 10c, for a permittivity ratio greater than 10 ($Q > 10$) the droplet’s shape deforms into an oblate form, for $Q=20$. As depicted in Figure 10 the dynamics of the two-phase flow is in agreement with Taylor’s theory shown in Figure 8. In Figure 10, the corresponding locations of the drop shown in Figure 8 are numbered in 1, 2 and 3 which are correspondent to permittivity ratios of 1, 10 and 20 respectively. The results for the flow fields are also in agreement with the numerical results of Hua et al. [40]. Leaky dielectric fluids have been considered in this study [27]. According to the results shown in Figure 8-Figure 10, it is concluded

that the model presented accurately predicts the electro-hydrodynamic forces on a leaky dielectric droplet immersed in a leaky dielectric fluid.

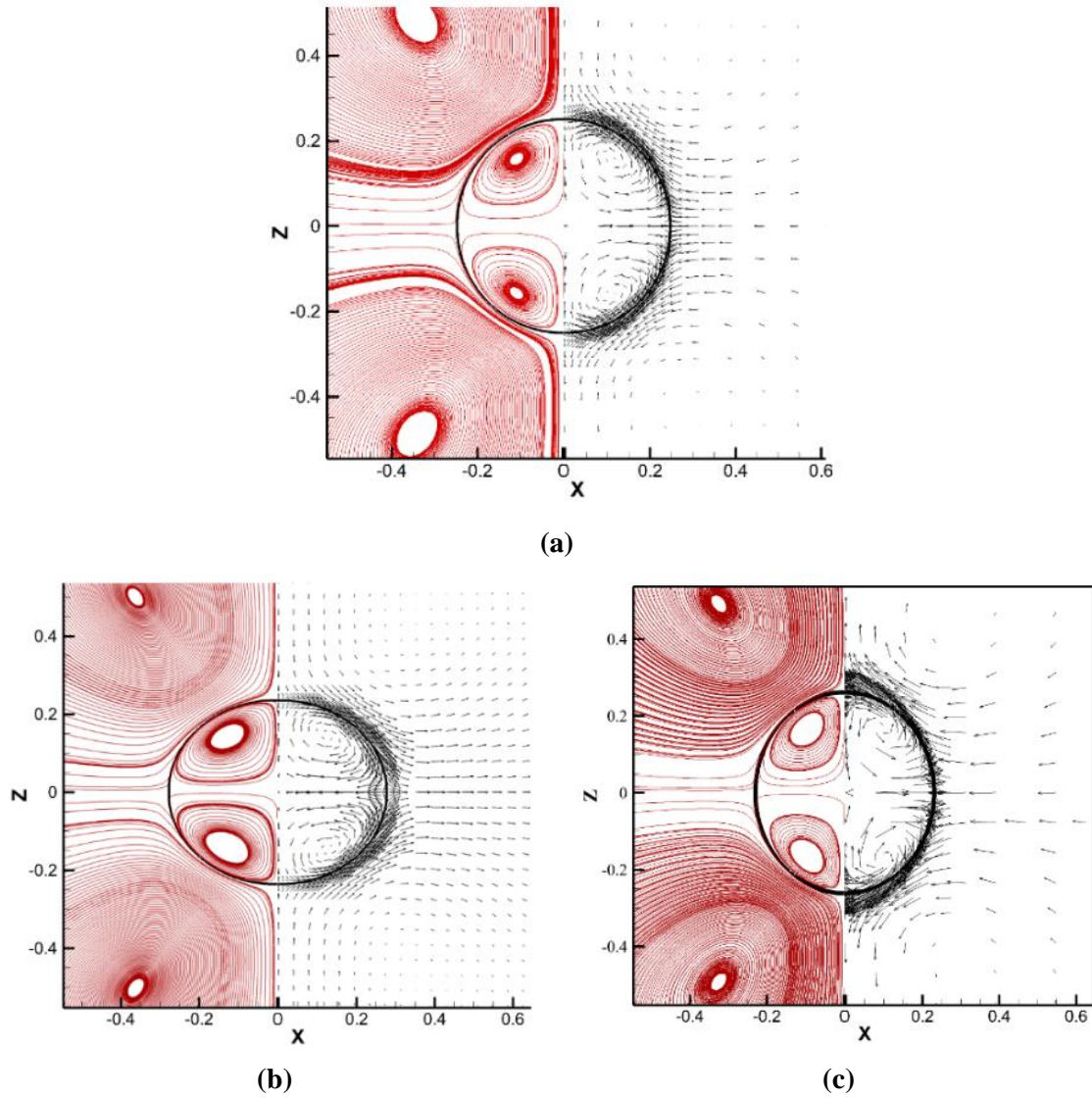


Figure 10. Drop deformation under effect of electric field (a) $Q=10$, (b) $Q=1$, and (c) $Q=20$ for $C=5$ and $Ca_E = 0.2$.

In Figure 11 numerical simulation has been compared to the analytical results of Sherwood [43] which shows the relationship between the droplet deformation and the Ca_E number. The numerical results are in excellent agreement with analytical theory.

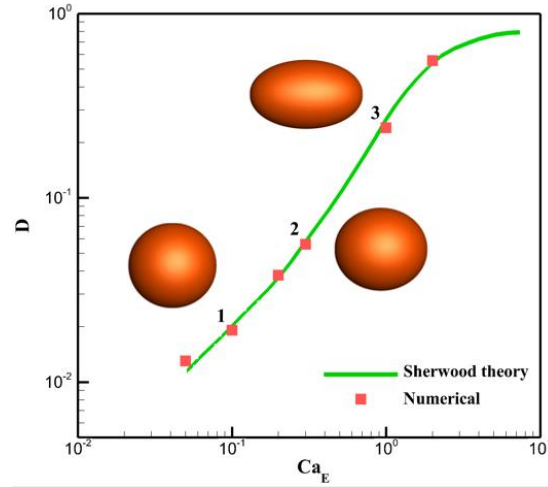


Figure 11. Deformation of the drop for various values of electric capillary number at permittivity ratio $Q=5$.

3.6 Numerical results for low Bo and Ga number

Figure 12 depicts the applicability of EHD as a controlling method to affect the deformation of the falling droplet under gravity. The figure displays time evolution of the falling drop and includes 3 columns in which the results obtained for $Ga = 40$, $Bo = 5$, $\rho_r = 2$, $\mu_r = 10$. Figure 12a displays the timely sequence of the falling drop without being under EHD. The EHD force keeps the drop in ellipsoidal oblate form which is in agreements with previous results mentioned above. EHD delays the deformation of the drop into a bowl-like form. As it is explained later in the current work, the break up the drop initiates by bag formation which generates after becoming the bowl-like shape. In contrast, Figure 12b shows how EHD can expedite the deformation of the drop into bag form by stretching it into the prolate form which is again in agreements with previous findings.

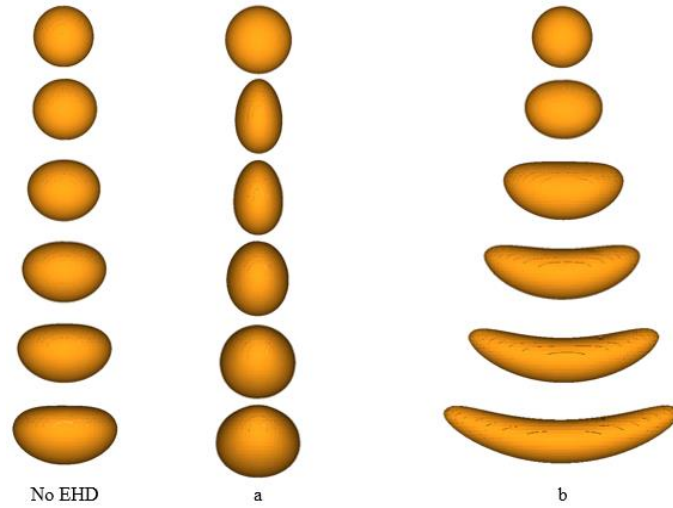


Figure 12. Effects of EHD on drop for, $Ga = 40$, $Bo = 5$, $Ca_E = 0.11$, $\rho_r = 2$, $\mu_r = 10$ for (a) $Q = 25$, $C = 5$ and (b) $Q = 5$, $C = 15$ from $t = 1$ to $t = 6$.

In Figure 13 the more results are shown to present the effects of EHD on the falling drop for different density ratio. Similarly, as shown in Figure 13a, the EHD delays the deformation of the drop into a stretched bowl-like shape and contrary to that EHD speeds up the process of bowl like formation by stretching the drop into the prolate form along the applied electric field.

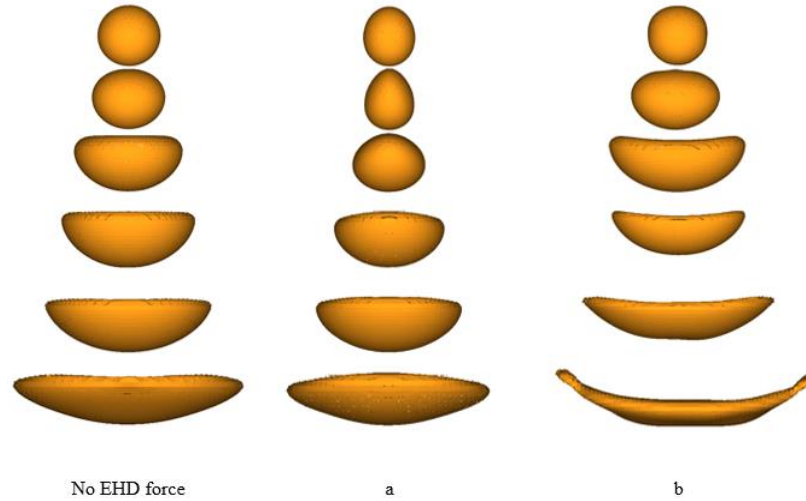


Figure 13. Effects of EHD on drop for, $Ga = 40$, $Bo = 5$, $Ca_E = 0.11$, $\rho_r = 5$, $\mu_r = 10$ for (a) $Q=25$, $C= 5$ and (b) $Q=5$, $C= 15$ from $t=1$ to $t=6$.

Figure 14 shows the effect of EHD force on terminal velocity's variation compared to the case that drop is not influenced by the electric field. Initially, there is not much of a difference between the velocity values and this difference increases as the drop gradually deforms into oblate form. The terminal velocity occurs when the sum of the drag force and the buoyancy is equal to the downward force of gravity acting on the object. Since the drag force heavily depends on the shape and as the area (projected area) of the drop reduces by deforming to oblate shape, therefore, the drag force reduces resulting in higher terminal velocity.

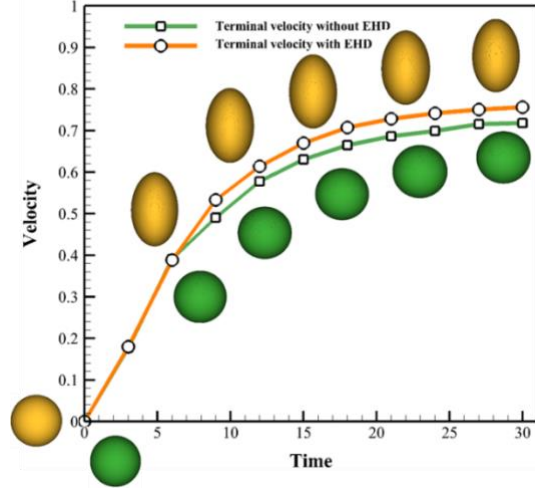


Figure 14 . Effect of EHD force on terminal velocity for $Ga = 40$, $Bo = 5$, $Ca_E = 0.028$, $\rho_r = 1.1$, $\mu_r = 10$ for $Q=5$, $C=25$.

Similarly, for the results shown in Figure 15, the drop takes the prolate form under the influence of the electric field which results in a larger projected area and therefore the magnitude of the drag force increase. The higher the drag force the lower the terminal velocity and as seen in the figure the terminal velocity reduces as the area of the drop increases.

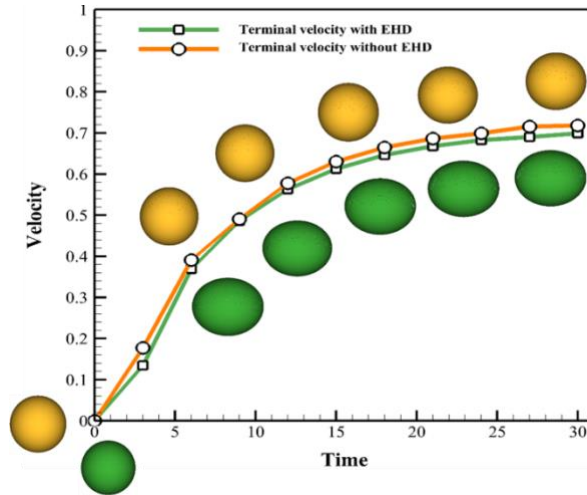


Figure 15 . Effect of EHD force on terminal velocity for $Ga = 40$, $Bo = 5$, $Ca_E = 0.11$, $\rho_r = 1.1$, $\mu_r = 10$ for $Q=25$, $C= 5$.

3.7 Numerical simulation for high Bo and Ga number

Figure 16 and Figure 17 show the numerical results of the time evolution of the drop deformation for $Bo=98$ and $Ga=24$. As shown in Figure 16, initially, the rear part of the drop starts deforming softly caused by the pressure difference as the vertical velocity of top of the drop is greater than the other parts. Therefore, as the front side stays rounded, the rear side of the drop changes to a flat surface. As the falling drop is under constant gravitational force the deformation increases. Thus the drop takes a bowl shape which is the beginning of the bag formation.

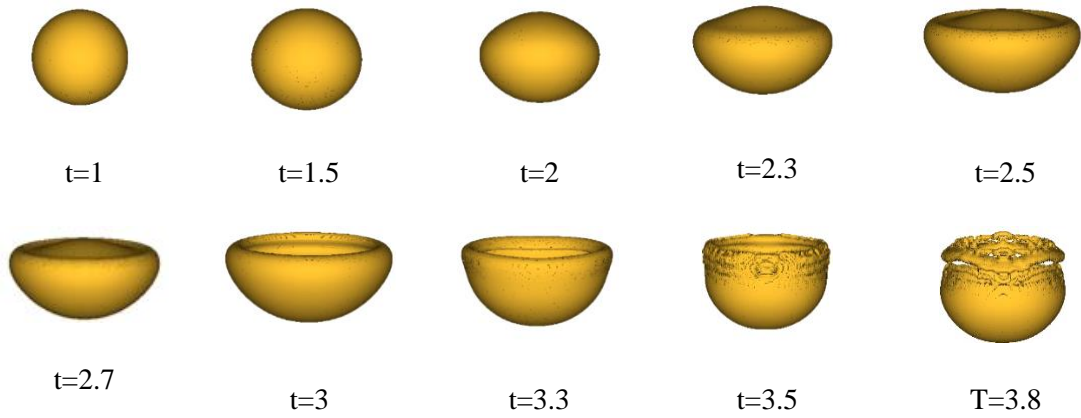


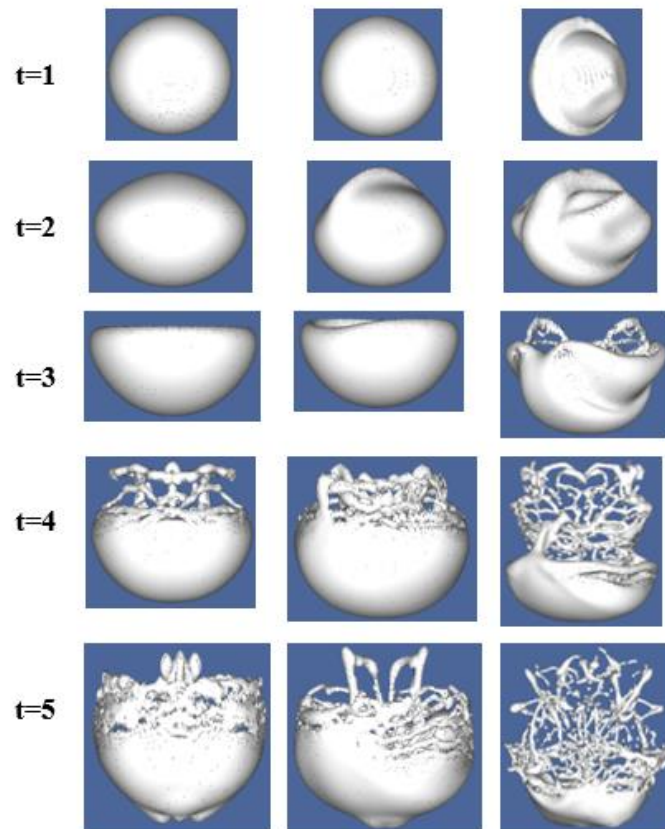
Figure 16. Initial deformation of the drop into bag shape for $Bo=98$, $Ga= 24$ and $\rho_r =10$.

The first column, Figure 17a shows the serial shot of droplet deformation and fragmentation when the electric force is not applied to the boundary of the computational domain. At the early stages, falling drop deforms to an oblate ellipsoid form from its initial spherical shape and then into a bag formation. This deformation is caused by the hydrodynamic pressure which is distributed non-uniformly around the drop that is set into motion by gravity [44]. The surface tension resists the deformation but it is not strong enough to keep the drop un-deformed in its initial stable shape.

Then the bag-shape grows and breaks and after ligaments, liquid bridges and droplets form. During the process of the atomization different types of instabilities such as capillary wave instabilities, Rayleigh–Taylor, and Rayleigh–Plateau take place. This atomization process continues with fragments’ break-up until reaching a stable condition. The similar process of drop deformation is seen in an experimental study by Cao et al.[45]. During the breakup process the bag bursts forming droplets, filaments, the rim on top and a core (The core here is stated as a considerable volume of the original drop is left). During the falling process, the liquid columns in forms of either straight or rounded decompose and form smaller fragments. Instability analysis investigates the bursting and retraction of a liquid sheet analytically. Bermond and Villermaux [46] presented a non-dimensional dispersion relation in which they showed that the film modifies its thickness and afterward is punctured by many holes in different positions which depends on the value of acceleration and the thickness. The holes formed at the interfaces because of the capillary force grow in radial directions as the capillary force acts radially and then attach to the neighbor’s punctures. The process of merging of the punctures leads to a network of attached ligaments which thereafter Bermond and Villermaux [46] into many droplets. The deformation of the falling drop into the bag shape has a similar procedure as those explained by Bermond and Villermaux [46]. In the present study, multiple holes are formed on the bag and then grow generating ligaments and these ligaments then decompose and form small fragments in which they are mostly stable. And at the end, the remaining unstable fragments collapse shortly. The holes are formed mostly closer to the rim at the top the bag which is thinner in the high curvature region compared to the other area and that causes the holes generated close to the torus on top. Afterward, the holes grow until filaments create between them. By development of the punctures, the filaments transform to liquid bridges, linking the core of the drop to the torus on top. Finally, these liquid bridges decompose into small, stable fragments. At this moment, the bag is entirely broken up and a new stage of breakup starts. Compared to the liquid sheet breakup study by [46] there is a notable similarity to

the bag breakup of a droplet. Multiple holes (punctures) perforates the bag then they grow and then the net of ligaments is generated. After the bag breakup, the rim on top, the core and the fragments generated between them remain. Following the bag breakup, a core of the primary drop remains. As shown the interface of the core starts to rupture for the bag breakup caused by the instabilities earlier. A network of ligaments is generated again and disconnected quickly afterward. Because of the fast growth of the capillary waves the ligaments are extremely unstable and therefore a thicker area in the ligament forms leading to creating a neck. By forming necks, the pinch-off mode generates over the ligaments resulting in detaching droplets from them. Fig. 14b shows the results for the falling drop under the electric field for $Q=25$, $k=5$. As seen, by applying EHD force the process of breaking up slows down compared to the case of no EHD force. Until $t=3$ the electric field causes some twist and turn in the shape of the falling drop. As seen from this figure, at $t=4$ the upper rim has not been separated distinctly yet, the fewer number of holes forms, the rupture slows down and still much thicker and stronger ligament exists between the core and the upper rim. And as the time goes on (from $t=5$ to $t=8$), the process of forming holes to perforates the bag, growing and generating the ligament occurs with a slower pace which can be seen at $t=7$. At this time, there is still a noticeable portion of the core left and at $t=8$ the drop structure consists of thick, stronger ligament and bridges which take much longer to be broken in smaller fragmentation and droplets compared to the case of no EHD force. In Fig. 14c electric field (EHD force) expedites the formation of the breakup. Initially, at $t=1$ the spherical shape of the drop takes ellipsoidal form. At $t=2$, it takes a strong twist and after transform into a basket form which is completely different from the bowl-like shape compared to the previous cases. It should be mention that all of these deformations depend on the fluid properties and magnitude of the electric field. At $t=4$ much more holes formed and grow faster; as seen a large portion of the drop transforms into filaments as the process of merging of the punctures speeds up leading to a network of attached ligaments. At $t=5$, only a small portion of the core is left and this amount reduces more and more as time goes on from

$t=6$ to 7. The structure of the breakup becomes much more uniform with smaller fragmentations. The results show that the electric field can be used as a powerful tool in controlling the deformation of the drop.



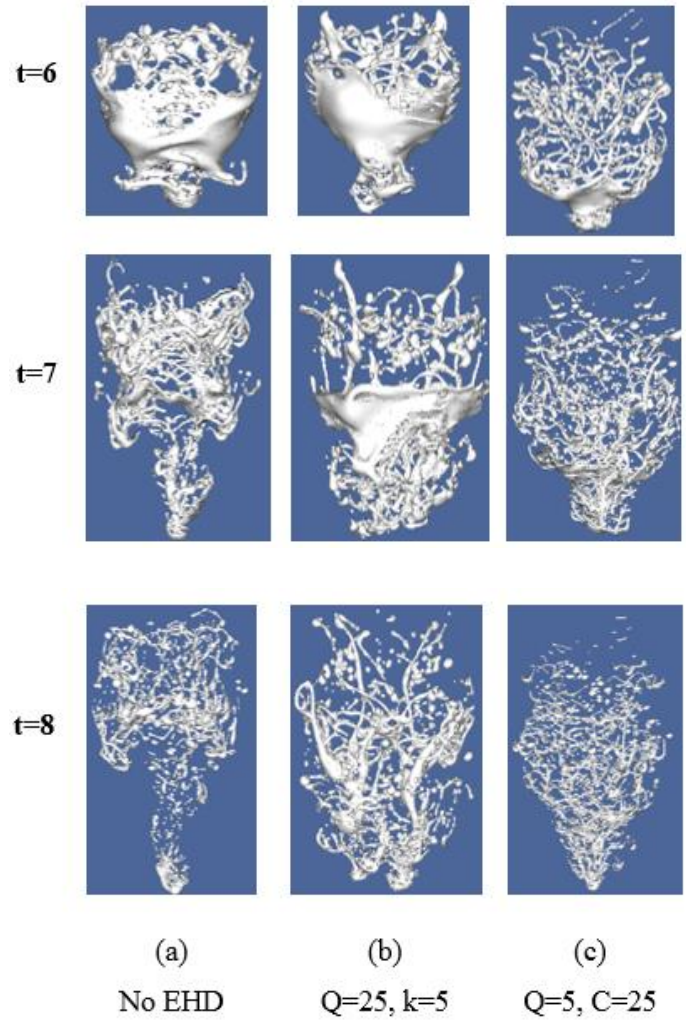


Figure 17. Time sequence deformation of the falling drop for $Ca_E = 0.028$.

4 Chapter 4: Analytical Solution

In this section, detailed analytical solutions of falling drop under effects of electric field have been presented and compared with DNS solution. Figure 18 shows a spherical droplet. The drop is centered and the spherical coordinate system r, θ is at the center of the drop. The motion of the droplet caused by the application of the electric field is negligible and the center of the mass of the drop remains unchanged.

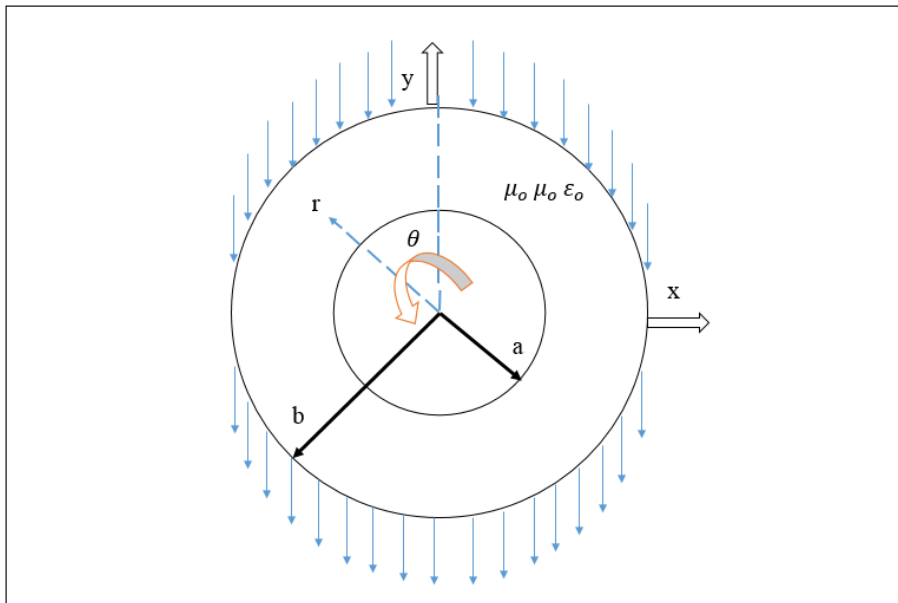


Figure 18. Schematic of a droplet under electric field.

Considering the radial distance from the center (r) and the polar angle (θ) which the positive value is measured in the counterclockwise direction and in relation to the direction of the electric field, we are now trying to solve the problem in the spherical coordinate system. An analytical solution has been presented for defining the deformation of the falling drop under the electric field.

It is worth mentioning that determining the deformation of a droplet under electric field requires the balance of net normal stresses by curvature effect. Here it should be noted that we used the formula which already presented in [20] and [47] to find the stresses induced by the electric field and falling respectively. Before using these relationships, a detailed derivation of these relationships is presented to give a better understanding the way how these stresses were obtained in [20] and [47] and also their physical effect on the governing physic. Then finally we used a balance of stresses to find the profile of the droplet.

4.1 Drops under electric field

In order to investigate the deformation of the droplet in the alternating current state, we first rectify the equations and boundary conditions again to find the potential electric field. So that the electric field is $E = E_o \cos(\omega t)$, $\omega = 2\pi\nu$. E_o is the maximum value of the electric field and ν the angular frequency. When ν is zero the uniform field of DC electric field. The dielectric constant properties k_1, k_2 , and the electrical resistance χ_1, χ_2 are independent of the frequency. In the absence of the electric charge in the environment, the potential equation in both the droplet and oil phase holds, therefore

$$\nabla^2 \Phi_j = 0.0, (j = 1, 2) \quad (30)$$

Followings are the assumptions:

- The amount of electrical potential inside the droplet is limited.
- $\vec{E} = E_o \cos(\omega t)$ in far field (infinite).
- The surface charge density σ is equal to the difference in electrical displacement D.
- On the interface $\Phi_1 = \Phi_2$.

- Current transfer on the interface is negligible and the increase rate σ is equal to the net flow of the charge from the interface.

We introduce the complex electric potential V_i' and V_o' to begin solving so that the real and virtual part of it both applies to the Laplace equation.

$$\begin{aligned}\Phi_i &= \text{Re}(V_i') = \text{Re}(V_i^* e^{i\omega t}) \\ \Phi_o &= \text{Re}(V_o') = \text{Re}(V_o^* e^{i\omega t})\end{aligned}\quad (31)$$

V_i^*, V_o^* mixed functions are not time dependent.

$$\begin{aligned}E_{r_o} &= \frac{-\partial\Phi_o}{\partial r} = -\text{Re}(E_\infty e^{i\omega t}) \cos(\theta) \rightarrow \Phi_o = r \cos(\theta) \text{Re}(E_\infty e^{i\omega t}) \\ E_{\theta_o} &= \frac{-\partial\Phi_o}{r \partial\theta} = -\text{Re}(E_\infty e^{i\omega t}) \sin(\theta) \rightarrow \Phi_o = r \cos(\theta) \text{Re}(E_\infty e^{i\omega t}) \\ \Phi_o(r = \infty) &= r \cos(\theta) \text{Re}(E_\infty e^{i\omega t}) = \text{Re}(V_o^* e^{i\omega t}) \Rightarrow V_o^* = r E_\infty \cos(\theta)\end{aligned}\quad (32)$$

For solving the potential equations we have:

$$\begin{aligned}\nabla^2\Phi &= \frac{1}{r^2} \frac{\partial}{\partial r} \left(r^2 \frac{\partial}{\partial r} \right) + \frac{1}{r^2 \sin(\theta)} \frac{\partial}{\partial \theta} \left(\sin(\theta) \frac{\partial}{\partial \theta} \right) \\ \nabla^2\Phi &= \frac{\partial}{\partial r} \left(r^2 \frac{\partial\Phi}{\partial r} \right) + \frac{1}{\sin(\theta)} \frac{\partial}{\partial \theta} \left(\sin(\theta) \frac{\partial\Phi}{\partial \theta} \right) = 0.0\end{aligned}\quad (33)$$

Using Separation Variable method [48] gives:

$$\begin{aligned}\Phi(r, \theta) &= R(r)Y(\theta), \quad \Phi_r = R'Y, \quad \Phi_\theta = RY' \\ \frac{\partial}{\partial r} \left[r^2 \frac{dR}{dr} Y \right] + \frac{1}{\sin(\theta)} \frac{\partial}{\partial \theta} \left[\sin(\theta) \frac{dY}{d\theta} R \right] &= 0.0 \quad \div RY \\ \frac{1}{R} \frac{d}{dr} \left(r^2 \frac{dR}{dr} \right) + \frac{1}{Y \sin(\theta)} \frac{d}{d\theta} \left(\sin(\theta) \frac{dY}{d\theta} \right) &= 0.0 \\ \left\{ \frac{1}{R} \frac{d}{dr} \left(r^2 \frac{dR}{dr} \right) = \rho, -\frac{1}{Y \sin(\theta)} \frac{d}{d\theta} \left(\sin(\theta) \frac{dY}{d\theta} \right) = \rho \right.\end{aligned}\quad (34)$$

Two equations are obtained in terms of radius and angle. To solve the first equation we will have:

$$2r \frac{dR}{dr} + \frac{d^2R}{dR^2} r^2 = \rho R \Rightarrow r^2 R'' + 2rR' - \rho R = 0.0$$

$$\lambda(\lambda-1) + 2\lambda - \rho = 0.0 \Rightarrow \lambda_1 = \frac{-1}{2} \pm \frac{(4\rho+1)^{\frac{1}{2}}}{2} \quad (35)$$

$$\begin{cases} \lambda_1 + \lambda_2 = -1 \\ \lambda_1 \cdot \lambda_2 = -\rho \end{cases} \Rightarrow \lambda_1 = L, \lambda_2 = -(L+1)$$

$$R(r) = Ar^L + Br^{-(L+1)}$$

The solution of the second equation is:

$$\left(\frac{1}{\sin(\theta)} \frac{d}{d\theta} (\sin(\theta) \frac{dY}{d\theta}) \right) = -Y \rho \times \sin^2(\theta)$$

$$\sin(\theta) \frac{d}{d\theta} (\sin(\theta) \frac{dY}{d\theta}) + Y \rho \sin^2(\theta) = 0.0$$

$$x = \cos(\theta) \rightarrow \frac{dx}{d\theta} = -\sin(\theta), \frac{d}{d\theta} = \frac{d}{dx} \frac{dx}{d\theta}, \frac{d}{d\theta} = \frac{d}{dx} (-\sin(\theta))$$

$$\sin(\theta) \frac{d}{d\theta} = \sin(\theta) \frac{d}{dx} (-\sin(\theta)) = -\frac{d}{dx} \sin^2(\theta) = \frac{d}{dx} (x^2 - 1)$$

$$-(1-x^2) \frac{d}{dx} ((x^2-1) \frac{dY}{dx}) + Y \rho (1-x^2) = 0.0 \quad (36)$$

↓

$$\frac{d}{dx} ((-x^2+1) \frac{dY}{dx}) + Y \rho = 0.0 \Rightarrow \frac{d}{dx} ((-x^2+1) \frac{dY}{dx}) + YL(L+1) = 0.0$$

$$Y = R_m(x) + S_m(x) \Rightarrow$$

$$C_0 \left\{ 1 - \frac{m(m+1)}{2!} x^2 + \dots \right\} + C_1 \left\{ x - \frac{(m-1)(m+2)}{3!} x^3 + \dots \right\}$$

$$Y = \sum_{n=0}^{\infty} \beta_l \cdot P_l(x)$$

$$\Phi(r, \theta) = R(r)Y(\theta) = \sum_{l=0}^{\infty} (A_l r^l + B_l r^{-(l+1)}) \cdot P_l(x) \begin{cases} A_l = A \cdot \beta_l \\ B_l = B \cdot \beta_l \end{cases} \quad (37)$$

where subscript m is even, $R_m(x)$ is a polynomial of degree m , which contains paired powers up to x_m , and $S_m(x)$ remains an infinite series, and when m is odd, $S_m(x)$ is a polynomial of degree m and only contains the powers of odd values to x_m , and $R_m(x)$ remains an infinite series. Here we use the change of variable $x = \cos(\theta)$ so that we have a Legendary Polynomial [48] according to $\cos(\theta)$. The result is

$$p_0(x) = 1, p_1(x) = x, p_2(x) = \frac{(3x^2 - 1)}{2}$$

$$V^* = (A_0 + B_0 r^{-1}) + (A_1 r + B_1 r^{-2}) \cos(\theta) + (A_2 r^2 + B_2 r^{-3}) \frac{(3 \cos(\theta)^2 - 1)}{2} \quad (38)$$

$$V_o^* = (A_1 r + B_1 r^{-2}) \cos(\theta)$$

$$V_i^* = (A_i r + B_i r^{-2}) \cos(\theta) \quad (39)$$

Since, given the first condition of the first potential, the electrical potential must be limited, therefore $B_i = 0$, with respect to the external potential boundary condition in infinity results in:

$$BC_1: \quad V_o^* = (E_\infty r + B r^{-2}) \cos(\theta)$$

$$V_i^* = (Cr) \cos(\theta) \quad (40)$$

$$BC_2: \Phi_i = \Phi_o(r = a) \Rightarrow \text{Re}(V_i^* e^{i\omega t}) = \text{Re}(V_o^* e^{i\omega t})$$

$$V_i^* = V_o^* \Rightarrow E_\infty a + B a^{-2} = Ca \Rightarrow E_\infty + B a^{-3} = C \quad (41)$$

Electric conductivity causes the electric charge to accumulate over time on the interface. If J the surface density and σ represents a charge on the surface, it gives the following:

$$\begin{aligned}
-\varepsilon_o E_r + \varepsilon_i E_n + \sigma_f &= 0.0 \\
-\varepsilon_o k_2 \left(-\frac{\partial V_o^*}{\partial r}\right) + \varepsilon_o k_1 \left(-\frac{\partial V_i^*}{\partial r}\right) + \sigma_f &= 0.0 \\
\varepsilon_o k_2 \operatorname{Re}\left[\frac{\partial V_o^*}{\partial r} e^{i\omega t}\right] - \varepsilon_o k_1 \operatorname{Re}\left[\frac{\partial V_i^*}{\partial r} e^{i\omega t}\right] + \sigma_f &= 0.0 \\
\sigma_f &= \operatorname{Re}[\sigma^* e^{i\omega t}] \\
\varepsilon_o k_2 \frac{\partial V_o^*}{\partial r} - \varepsilon_o k_1 \frac{\partial V_i^*}{\partial r} &= -\sigma^*
\end{aligned} \tag{42}$$

Assuming $\sigma_f = \operatorname{Re}[\sigma^* e^{i\omega t}]$, the two sides of the equation can be simplified as

$$\begin{aligned}
J_r - J_n + \frac{\partial \sigma_f}{\partial t} &= 0.0 \\
\frac{-1}{\chi_2} \operatorname{Re}\left[\frac{\partial V_o^*}{\partial r} e^{i\omega t}\right] + \frac{1}{\chi_1} \operatorname{Re}\left[\frac{\partial V_i^*}{\partial r} e^{i\omega t}\right] + \operatorname{Re}[\sigma^* i \omega . e^{i\omega t}] &= 0.0 \\
\sigma^* i \omega &= \frac{1}{\chi_2} \frac{\partial V_o^*}{\partial r} - \frac{1}{\chi_1} \frac{\partial V_i^*}{\partial r}
\end{aligned} \tag{43}$$

$$\begin{aligned}
\frac{1}{\chi_2} \frac{\partial V_o^*}{\partial r} - \frac{1}{\chi_1} \frac{\partial V_i^*}{\partial r} &= i\omega \left(-\varepsilon_o k_2 \frac{\partial V_o^*}{\partial r} + \varepsilon_o k_1 \frac{\partial V_i^*}{\partial r}\right) \\
B_{C_3} : \frac{\partial V_o^*}{\partial r} \left[\frac{1}{\chi_2} + i\omega \varepsilon_o k_2\right] &= \frac{\partial V_i^*}{\partial r} \left[\frac{1}{\chi_1} + i\omega \varepsilon_o k_1\right]
\end{aligned} \tag{44}$$

$$\begin{aligned}
(E_\infty - 2Ba^{-3}) \left(\frac{1}{\chi_2} + i\omega \varepsilon_o k_2\right) &= C \left(\frac{1}{\chi_1} + i\omega \varepsilon_o k_1\right) \\
\frac{\frac{1}{\chi_2} + i\omega \varepsilon_o k_2}{\frac{1}{\chi_1} + i\omega \varepsilon_o k_1} &= O \Rightarrow (E_\infty - 2Ba^{-3})O = C = (E_\infty + Ba^{-3})
\end{aligned} \tag{45}$$

$$\begin{aligned}
OE_\infty - 2OBa^{-3} &= (E_\infty + Ba^{-3}) \Rightarrow Ba^{-3} = \frac{E_\infty(O-1)}{1+2O} \\
C &= E_\infty + E_\infty \frac{O-1}{1+2O} = E_\infty \left(1 + \frac{O-1}{1+2O}\right) = \frac{3E_\infty O}{1+2O}
\end{aligned}$$

$$A = \frac{O}{2O+1} = \frac{\frac{\frac{1}{\chi_2} + iw \varepsilon_o k_2}{\chi_1}}{\frac{\frac{1}{\chi_2} + iw \varepsilon_o k_2}{2\frac{\chi_2}{\frac{1}{\chi_1} + iw \varepsilon_o k_1} + 1}} = \frac{\frac{1}{\chi_2} + iw \varepsilon_o k_2}{2\left(\frac{1}{\chi_2} + iw \varepsilon_o k_2\right) + \frac{1}{\chi_1} + iw \varepsilon_o k_1} = \dots$$

$$\frac{\frac{\chi_1 + iw \varepsilon_o k_2 \chi_1}{\chi_2}}{1 + iw \varepsilon_o k_1 \chi_1 + 2\frac{\chi_1}{\chi_2} + 2iw \varepsilon_o k_2 \chi_1} = \frac{R + iwa}{(2R + 1) + iwa(q + 2)}$$

$$\left. \begin{array}{l} q = \frac{k_1}{k_2} \\ R = \frac{\chi_1}{\chi_2} \\ a = \varepsilon_o k_2 \chi_1 \\ a = \frac{\varepsilon_{out}}{\sigma_{in}} \end{array} \right\} \quad (46)$$

$$C = 3E_\infty A, Ba^{-3} = 3E_\infty A - E_\infty$$

$$B = E_\infty a^3 (3A - 1) \quad (47)$$

The phrase A is an imaginary phrase.

$$V_o^* = E_\infty \left\{ r + (3A - 1)a^3 r^{-2} \right\} \cos(\theta)$$

$$V_i^* = 3E_\infty A r \cos(\theta) \quad (48)$$

If the frequency is zero, then $A = \frac{R}{2R+1}$ (here $R = \frac{\sigma_o}{\sigma_i}$).

$$V_o^* = E_\infty \left(r + \left(\frac{3R}{2R+1} - 1 \right) a^3 r^{-2} \right) = E_\infty \left(r + \left(\frac{3}{2+R} - 1 \right) a^3 r^{-2} \right)$$

$$V_o^* = E_\infty \left(r + \left(\frac{1-R}{2+R} \right) \frac{a^3}{r^2} \right) \cos(\theta), V_i^* = 3E_\infty \frac{R}{1+2R} r \cos(\theta) \quad (49)$$

$$V_i^* = \frac{3E_\infty}{R+2} r \cos(\theta)$$

In this case, the result of the zero frequency is exactly the same as the solution obtained from the solution above. Next, the electrical stresses on the droplet environment, around, and also on the interface are calculated.

$$\begin{aligned}
E_r &= -\frac{\partial\Phi}{\partial r} = -\text{Re}(V^* e^{i\omega t})_r = -\text{Re}\left(\frac{\partial V^*}{\partial r} e^{i\omega t}\right) \\
E_{ri} &= -3E_\infty A \cos(\theta) e^{i\omega t} \Rightarrow E_{ri} = -3E_\infty \cos(\theta) \text{Re}(A e^{i\omega t}) \\
E_{ro} &= -\text{Re}\left(\frac{\partial V_o^*}{\partial r} e^{i\omega t}\right) = \text{Re}\left[-E_\infty \left\{1 - 2(3A - 1)\left(\frac{a}{r}\right)^3\right\} \cos(\theta) e^{i\omega t}\right]
\end{aligned} \tag{50}$$

$$\begin{aligned}
E_\theta &= -\frac{\partial\Phi}{r\partial\theta} = \frac{-1}{r} \text{Re}\left(\frac{\partial V^*}{\partial\theta} e^{i\omega t}\right) \\
E_{\theta i} &= 3E_\infty \sin(\theta) \text{Re}(A e^{i\omega t}) \\
E_{\theta o} &= \text{Re}\left[E_\infty \left\{1 + (3A - 1)\left(\frac{a}{r}\right)^3\right\} \sin(\theta) e^{i\omega t}\right]
\end{aligned} \tag{51}$$

In order to obtain electrical stress on the interface we need to substitute $r = b$ in the above relations.

$$\begin{aligned}
E_{ri} &= -3E_\infty \cos(\theta) \text{Re}(A e^{i\omega t}) \\
E_{ro} &= \text{Re}\left[-3E_\infty (1 - 2A) \cos(\theta) e^{i\omega t}\right] = -3E_\infty \cos(\theta) \text{Re}\left[(1 - 2A) e^{i\omega t}\right] \\
E_{\theta i} &= 3E_\infty \sin(\theta) \text{Re}(A e^{i\omega t}) \\
E_{\theta o} &= 3E_\infty \sin(\theta) \text{Re}(A e^{i\omega t})
\end{aligned} \tag{52}$$

Therefore, tangential tensions on the interface for droplets and oils are the same that indicates the correct voltage setting on the interface. To calculate the electric charge distribution on the interface, σ is calculated as

$$\begin{aligned}
\sigma_f &= \text{Re}[\sigma^* e^{i\omega t}] \Rightarrow \sigma^*(r=a) \Rightarrow (-\varepsilon_o k_2 \frac{\partial V_o^*}{\partial r} + \varepsilon_o k_1 \frac{\partial V_i^*}{\partial r}) \Big|_{r=a} \\
\sigma^* &= -\varepsilon_o k_2 3E_\infty (1-2A) \cos(\theta) + \varepsilon_o k_1 3E_\infty A \cos(\theta) = \dots \\
&\text{Re} \left[(-\varepsilon_o k_2 3E_\infty (1-2A) + \varepsilon_o k_1 3E_\infty A) \cos(\theta) e^{i\omega t} \right] \\
&\text{Re} [\varepsilon_o k_2 3E_\infty \cdot [A(q+2)-1] \cos(\theta) e^{i\omega t}] \\
A(q+2)-1 &= \frac{(q+2)R + iwa}{(2R+1) + iwa(q+2)} - \frac{(2R+1) + iwa(q+2)}{(2R+1) + iwa(q+2)} = \dots \\
A(q+2)-1 &= \frac{Rq-1}{(2R+1) + iwa(q+2)} \tag{53} \\
(2R+1) + iwa(q+2) &= \sqrt{(2R+1)^2 + (wa(q+2))^2} \exp(i\theta_1) \\
\theta_1 &= \tan^{-1} \left(\frac{wa(q+2)}{(2R+1)} \right) \\
\sigma_f &= \text{Re} [\varepsilon_o k_2 3E_\infty \cdot \left[\frac{Rq-1}{\sqrt{(2R+1)^2 + (wa(q+2))^2}} \exp(-i\theta_1) \right] \cos(\theta) e^{i\omega t}] \\
\sigma_f &= \frac{\varepsilon_o k_2 3E_\infty (Rq-1)}{\sqrt{(2R+1)^2 + (wa(q+2))^2}} \cos(-\theta_1 + \omega t) \cdot \cos(\theta)
\end{aligned}$$

For zero frequency we have the following expression, which indicates that the solution is correct.

$$\sigma_f = \frac{\varepsilon_o k_2 3E_\infty (q-R)}{(R+2)} \cos(\theta) \tag{54}$$

The term A decomposes into two real and imaginary parts therefore

$$\begin{aligned}
A &= \text{Re}_A + i \text{IM}_A \\
\frac{R + iwa}{(2R+1) + iwa(q+2)} &= \frac{A + iB}{C + iD} \frac{C - iD}{C - iD} = \frac{(AC + BD) + i(BC - AD)}{C^2 + D^2} \tag{55}
\end{aligned}$$

$$\text{Re}_A = \frac{R(2R+1) + w^2 a^2 (q+2)}{(2R+1)^2 + w^2 a^2 (q+2)^2}, \text{IM}_A = \frac{aw(1-Rq)}{(2R+1)^2 + w^2 a^2 (q+2)^2} \tag{56}$$

As we have proved in the DC current discussion, the electrical stresses are calculated as.

$$T_{rr}^e = \frac{1}{2} \varepsilon_0 (E_{no}^2 - E_{to}^2) - \frac{1}{2} \varepsilon_i (E_{ni}^2 - E_{ti}^2) \quad (57)$$

$$T_{rr}^e = \frac{\varepsilon_0 k_2}{2} (E_{no}^2 - E_{to}^2) - q (E_{ni}^2 - E_{ti}^2)$$

$$T_{nt}^e = \varepsilon_0 k_2 E_{no} E_{to} - \varepsilon_0 k_1 E_{ni} E_{ti} = \varepsilon_0 k_2 E_t (E_{ro} - q E_{ri}) \quad (58)$$

As the electric charge relationship indicates, the overall charge on the interface is zero and decreases with increasing frequency of electric charge on the interface. Also, in the case where $Rq > 1$, the portion of the droplet encountered with positive voltage is positive and the negative electrode is negatively charged, while for $Rq < 1$, the reverse happens. When $Rq = 1$, the electric charge on the interface is zero. The pure electric stresses on the interface will have a stable portion and a transient portion. Based on the results obtained for electrical potential and tangential and normal stresses,

$$\begin{aligned} T_{rr}^e \Big|_{net} &= T_{rr}^e \Big|_S + T_{rr}^e \Big|_T \\ T_{r\theta}^e \Big|_{net} &= T_{r\theta}^e \Big|_S + T_{r\theta}^e \Big|_T \end{aligned} \quad (59)$$

$$\begin{aligned} E_{ni}^2 &= 9E_\infty^2 \cos^2(\theta) \left| \text{Re}(A e^{i\omega t}) \right|^2 \\ E_{no}^2 &= 9E_\infty^2 \cos^2(\theta) \left| \text{Re}[(1-2A)e^{i\omega t}] \right|^2 \\ E_{\theta}^2 &= 9E_\infty^2 \sin^2(\theta) \left| \text{Re}(A e^{i\omega t}) \right|^2 \end{aligned} \quad (60)$$

$$\begin{aligned} \left| \text{Re}(A e^{i\omega t}) \right|^2 &= \frac{\text{Re}(A^2 e^{2i\omega t})}{2} + \frac{A\bar{A}}{2} \\ \left| \text{Re}[(1-2A)e^{i\omega t}] \right|^2 &= \left(\frac{(1-2A)e^{i\omega t} + (1-2\bar{A})e^{-i\omega t}}{2} \right)^2 \\ \left| \text{Re}[(1-2A)e^{i\omega t}] \right|^2 &= \frac{\text{Re}[(1-2A)^2 e^{2i\omega t}]}{2} + \frac{1-2(A+\bar{A})+4A\bar{A}}{2} \end{aligned} \quad (61)$$

$$\begin{aligned}
T_{rr}^e)_{net} &= \frac{\varepsilon_0 k_2}{2} \{(E_{no}^2 - E_{to}^2) - q(E_{ni}^2 - E_{ti}^2)\} \\
T_{rr}^e)_{net} &= \frac{9E_\infty^2 \varepsilon_0 k_2}{2} \left(\right. \\
&\cos^2(\theta) \frac{\text{Re} \left[((1-2A)^2 e^{2iwt}) \right]}{2} + \frac{1-2(A+\bar{A})+4A\bar{A}}{2} - \\
&\sin^2(\theta) \frac{\text{Re}(A^2 e^{2iwt})}{2} + \frac{A\bar{A}}{2} \\
&-q \\
&\left. \cos^2(\theta) \frac{\text{Re}(A^2 e^{2iwt})}{2} + \frac{A\bar{A}}{2} - \sin^2(\theta) \frac{\text{Re}(A^2 e^{2iwt})}{2} + \frac{A\bar{A}}{2} \right)
\end{aligned} \tag{62}$$

$$\begin{aligned}
&\frac{9E_\infty^2 \varepsilon_0 k_2}{4} (\cos^2(\theta)) : \\
&(1-2A)^2 e^{2iwt} + 1-2(A+\bar{A})+4A\bar{A} + \\
&\text{Re}(A^2 e^{2iwt}) + A\bar{A} + \\
&-q (\text{Re}(A^2 e^{2iwt}) + A\bar{A}) \\
&-q (\text{Re}(A^2 e^{2iwt}) + A\bar{A}) \\
&\frac{9E_\infty^2 \varepsilon_0 k_2}{4} \left(\right. \\
&- \text{Re}(A^2 e^{2iwt}) - A\bar{A} \\
&\left. q (\text{Re}(A^2 e^{2iwt}) + A\bar{A}) \right)
\end{aligned} \tag{63}$$

We already know that \bar{A} is conjugate of A and A is divided into two real and imaginary parts, whose components are known. Therefore, if $A = \alpha + iB$, then it will be $\bar{A} = \alpha - iB$ and $\bar{A}A = \alpha^2 + B^2$, $\bar{A} + A = 2\alpha$. We already obtained α, B . By placing in the above relations, we will have a constant normal stress part. The droplet radius is shown with b.

$$\begin{aligned}
T_{rr}^e)_{steady} &= \cos^2(\theta) \left(1-2(A+\bar{A})+4A\bar{A} + A\bar{A} - 2qA\bar{A} + A\bar{A}(q-1) \right) \\
T_{rr}^e)_{steady} &= \cos^2(\theta) \left\{ A\bar{A}(5-2q) + 1-2(A+\bar{A}) \right\} + A\bar{A}(q-1) \\
T_{rr}^e)_{steady} &= \frac{9E_\infty^2 \varepsilon_0 k_2}{4} \left\{ \frac{(R^2 - 2qR^2 + 1) + a^2 w^2 (q-1)^2}{(2R+1)^2 + a^2 w^2 (q+2)^2} \right\} \cos^2(\theta) + ws \\
ws = (q-1)(\alpha^2 + \beta^2) &= \frac{9E_\infty^2 \varepsilon_0 k_2}{4} \frac{(q-1)(R^2 + a^2 w^2)}{(2R+1)^2 + a^2 w^2 (q+2)^2}
\end{aligned} \tag{64}$$

The transient part of the normal stress is:

$$\begin{aligned}
T_{rr}^e \Big|_{unsteady} &= \text{Re} \left[((1-2A)^2 + A^2 - 2qA^2) e^{2i\omega t} \cos^2(\theta) + (A^2 e^{2i\omega t}) (q-1) \right] \\
((1-2A)^2 + A^2 - 2qA^2) &= A^2(5-2q) - 4A + 1 = F_r^* \\
T_{rr}^e \Big|_{unsteady} &= \frac{9E_\infty^2 \varepsilon_0 k_2}{4} \text{Re} [F_r^* e^{2i\omega t} \cos^2(\theta)] + \omega t \\
\omega t &= \frac{9E_\infty^2 \varepsilon_0 k_2}{4} (q-1) \text{Re} [A^2 e^{2i\omega t}]
\end{aligned} \tag{65}$$

$$\begin{aligned}
T_{r\theta}^e \Big|_{net} &= \varepsilon_0 k_2 E_t (E_{r\theta} - qE_{n\theta}) = \varepsilon_0 k_2 3E_\infty \sin(\theta) \text{Re}(A e^{i\omega t}) \{ \dots \} \\
&- 3E_\infty \cos(\theta) \text{Re} \left[(1-2A) e^{i\omega t} \right] + q 3E_\infty \cos(\theta) \text{Re}(A e^{i\omega t}) \\
&\varepsilon_0 k_2 9E_\infty^2 \sin(\theta) \cos(\theta) \left[-\text{Re}(A e^{i\omega t}) \text{Re}(1-2A) e^{i\omega t} + q (\text{Re}(A e^{i\omega t}))^2 \right] \\
\text{Re}(A e^{i\omega t}) \cdot \text{Re}(1-2A) e^{i\omega t} &= \frac{\text{Re}(A(1-2A) e^{2i\omega t})}{2} + \frac{A - 2A\bar{A} + \bar{A} - 2A\bar{A}}{4} \\
[\dots] &= \text{Re}(2A^2 - A) e^{2i\omega t} + \text{Re}(qA^2 e^{2i\omega t}) + \frac{4A\bar{A} - (A + \bar{A})}{2} \\
2A^2 - A + qA^2 &= \frac{(Rq-1)(R+i\omega a)}{((2R+1) + i\omega a)(q+2)^2} \\
F_\theta^* &= \frac{(R+i\omega a)}{((2R+1) + i\omega a)(q+2)^2}
\end{aligned} \tag{66}$$

$$\begin{aligned}
T_{r\theta}^e \Big|_{unsteady} &= \frac{9\varepsilon_0 k_2 E_\infty^2}{2} \sin(\theta) \cos(\theta) (Rq-1) \text{Re} [F_\theta^* e^{2i\omega t}] \\
T_{r\theta}^e \Big|_{steady} &= \frac{9\varepsilon_0 k_2 E_\infty^2}{2} \sin(\theta) \cos(\theta) \{ 2A\bar{A} - \alpha + qA\bar{A} \} \\
T_{r\theta}^e \Big|_{steady} &= \frac{9\varepsilon_0 k_2 E_\infty^2}{2} \sin(\theta) \cos(\theta) \frac{(Rq-1)R}{(2R+1)^2 + a^2 \omega^2 (q+2)^2}
\end{aligned} \tag{67}$$

As the relations above indicate, $T_{r\theta steady}$ changes sign in $Rq = 1$, and as a result, the flow of fluid on both sides of the interface is affected by this sign change. As mentioned earlier, in $Rq = 1$, the tangent electric stress's constant is zero. When the DC current is used, the resultant electrical stresses on the interface, which indicate the electrical forces applied to the droplet border, are:

$$\begin{aligned}
F_{r\theta} &= \frac{9\varepsilon_0 k_2 E_\infty^2}{2} \sin(\theta) \cos(\theta) \frac{(Rq-1)R}{(2R+1)^2} \\
F_{rr} &= \frac{9E_\infty^2 \varepsilon_0 k_2}{2} \frac{(R^2 - 2qR^2 + 1) \cos^2(\theta) + R^2(q-1)}{(2R+1)^2}
\end{aligned} \tag{68}$$

Due to the fact that the stresses of the electric field by the stresses on the hydrodynamic must be neutralized, therefore:

$$\begin{aligned}
\nabla^2 &= \frac{\partial^2}{\partial r^2} + \frac{\sin(\theta)}{r^2} \left[\frac{\partial}{\partial \theta} \left\{ \frac{1}{\sin(\theta)} \frac{\partial}{\partial \theta} \right\} \right] \\
\psi(r, \theta) &= F(r) \cdot \sin^2(\theta) \cos(\theta) \\
\psi(r, \theta) &= F(r) \cdot (x - x^3) \\
\frac{\partial^2}{\partial r^2} &= F''(x - x^3), \quad \frac{\partial}{\partial \theta} = \frac{\partial}{\partial x} (-\sin(\theta)) \\
\nabla^2 &= \psi_{rr} + \frac{1-x^2}{r^2} \psi_{xx}
\end{aligned} \tag{69}$$

In order to obtain the function F, we must solve the Cauchy-Euler equation [48]. The results is:

$$\begin{aligned}
\psi_{xx} &= -6x, \quad \nabla^2 \psi = F''(x - x^3) + \frac{F}{r^2} (-6x + 6x^3) \\
\nabla^2 \psi &= \left(F'' - \frac{6F}{r^2} \right) (x - x^3) \\
\nabla^4 \psi &= \nabla^2 \psi_{rr} + \frac{1-x^2}{r^2} \nabla^2 \psi_{xx} \\
\nabla^2 \psi_{rr} &= F''' - 6 \left\{ \frac{F''}{r^2} - \frac{2F'}{r^3} + \frac{6F}{r^4} - \frac{2F'}{r^3} \right\} (x - x^3) \\
\frac{1-x^2}{r^2} \nabla^2 \psi_{xx} &= \left(\frac{F''}{r^2} - \frac{6F}{r^4} \right) (-6)(x - x^3) \\
\nabla^4 \psi &= \left[F''' - 12 \frac{F''}{r^2} + 24 \frac{F'}{r^3} \right] (x - x^3) \\
\lambda(\lambda-1)(\lambda-2)(\lambda-3) - 12\lambda(\lambda-1) + 24\lambda &= 0.0 \\
\lambda &= -2, 0, 3, 5 \\
(x - x^3) &= x(1 - x^2) = \cos(\theta)(1 - \cos^2(\theta)) = \cos(\theta) \sin^2(\theta)
\end{aligned} \tag{70}$$

Since the inside velocity of the droplet must be limited, $A = B = 0$ for the droplet inside and, also to limit the tangential and normal velocities at infinity it is required to $C = D = 0$.

$$\begin{aligned}\psi_i &= (Ar^{-2} + B + Cr^3 + Dr^5) \sin^2(\theta) \cos(\theta) \\ \psi_o &= (Ar^{-2} + B + Cr^3 + Dr^5) \sin^2(\theta) \cos(\theta)\end{aligned}\quad (71)$$

$$\begin{aligned}u_r &= \frac{1}{r^2 \sin(\theta)} \frac{\partial \psi}{\partial \theta}, u_\theta = \frac{-1}{r \sin(\theta)} \frac{\partial \psi}{\partial r} \\ \psi_i &= (Cr^3 + Dr^5) \sin^2(\theta) \cos(\theta) \\ \psi_o &= (Ar^{-2} + B) \sin^2(\theta) \cos(\theta)\end{aligned}\quad (72)$$

By determining the form of the flow function, the tangential and normal velocities in and out of the droplet are:

$$\begin{aligned}u_{ri} &= \frac{Cr^3 + Dr^5}{r^2 \sin(\theta)} (2 \cos^2(\theta) \sin(\theta) - \sin^3(\theta)) = \dots \\ u_{ri} &= (Cr + Dr^3)(3 \cos^2(\theta) - 1) \\ u_{ro} &= \frac{Ar^{-2} + B}{r^2 \sin(\theta)} (2 \cos^2(\theta) \sin(\theta) - \sin^3(\theta)) = \dots \\ u_{ro} &= (Ar^{-4} + Br^{-2})(3 \cos^2(\theta) - 1) \\ u_{\theta i} &= \frac{-\cos(\theta) \sin^2(\theta)}{r \sin(\theta)} (3Cr^2 + 5Dr^4) = \dots \\ u_{\theta i} &= \frac{-\sin(2\theta)}{2} (3Cr + 5Dr^3) \\ u_{\theta o} &= \frac{-\cos(\theta) \sin^2(\theta)}{r \sin(\theta)} (-2Ar^{-3}) = \sin(2\theta)Ar^{-4}\end{aligned}\quad (73)$$

In order to obtain the velocity constants, we consider boundary conditions as DC solutions, therefore

$$\begin{aligned}
BC_1 : u_{r_i} = u_{r_o} = 0 \Big|_{r=b} &\Rightarrow \begin{cases} Cb + Db^3 = 0.0 \\ Ab^{-4} + Bb^{-2} = 0.0 \end{cases} \\
BC_2 : u_{\theta_i} = u_{\theta_o} \Big|_{r=b} &\Rightarrow 3Cb + 5Db^3 = -2Ab^{-4}
\end{aligned} \tag{74}$$

Before we apply the two further boundary conditions, we must first obtain $T_{rr}^h, T_{r\theta}^h$.

$$\begin{aligned}
T_{r\theta}^h &= \mu \left[r \frac{\partial}{\partial r} \left(\frac{u_\theta}{r} \right) + \frac{1}{r} \frac{\partial u_r}{\partial \theta} \right] & T_{r\theta}^h &= \mu \left[r \frac{\partial}{\partial r} \left(\frac{u_\theta}{r} \right) + \frac{1}{r} \frac{\partial u_r}{\partial \theta} \right] \\
\text{outside :} & & \text{Inside :} & \\
\left(\frac{u_\theta}{r} \right) &= Ar^{-5} \sin(2\theta) & \left(\frac{u_\theta}{r} \right) &= -(3C + 5Dr^2) \frac{\sin(2\theta)}{2} \\
\frac{\partial}{\partial r} () &= -5Ar^{-6} \sin(2\theta) & \frac{\partial}{\partial r} () &= -(10Dr) \frac{\sin(2\theta)}{2} \\
r() &= -5Ar^{-5} \sin(2\theta) & r() &= -(10Dr^2) \frac{\sin(2\theta)}{2} \\
\frac{\partial u_r}{\partial \theta} &= (Ar^{-4} + Br^{-2})(6 \cos(\theta) \sin(\theta)) & \frac{\partial u_r}{\partial \theta} &= -(Cr + Dr^3) 3 \sin(2\theta) \\
&= -(Ar^{-4} + Br^{-2}) 3 \sin(2\theta) & \frac{1}{r} () &= -(C + Dr^2) 3 \sin(2\theta) \\
\frac{1}{r} () &= -(Ar^{-5} + Br^{-3}) 3 \sin(2\theta) & &
\end{aligned} \tag{75}$$

$$\begin{aligned}
T_{r\theta}^h &= \mu_o [-5Ar^{-5} - 3(Ar^{-5} + Br^{-3})] - \mu_i [-5Dr^2 - 3(C + Dr^2)] \sin(2\theta) \\
T_{r\theta}^h &= [\mu_o (-8Ar^{-5} - 3Br^{-3}) - \mu_i (-3C - 8Dr^2)] \sin(2\theta)
\end{aligned} \tag{76}$$

$$\begin{aligned}
T_{rr}^h &= 2\mu \frac{\partial u_r}{\partial r} \\
&\begin{cases} \text{outside} := (-4Ar^{-5} - 2Br^{-3})(3 \cos^2(\theta) - 1) \\ \text{inside} := (C + 3Dr^2)(3 \cos^2(\theta) - 1) \end{cases} \\
T_{rr}^h \Big|_{net} &= (3 \cos^2(\theta) - 1) [\mu_o (-4Ab^{-5} - 2Bb^{-3}) - \mu_i (C + 3Db^2)]
\end{aligned} \tag{77}$$

$$\begin{aligned}
BC_3 : T_{r\theta}^h + T_{r\theta}^e &= 0.0 \\
\frac{9\varepsilon_0 k_2 E_\infty^2}{4} \sin(2\theta) &\left\{ (Rq-1) \operatorname{Re}[F_\theta^* e^{2i\omega t}] + \frac{(Rq-1)R}{(2R+1)^2 + a^2 \omega^2 (q+2)^2} \right\} \\
-5Ab^{-5}(\mu_i + \mu_o) \sin(2\theta) &= 0.0 \\
BC_{1,2} \Rightarrow &\begin{cases} B = -Ab^{-2} \\ C = Ab^{-5} \Rightarrow T_{r\theta}^h = -5Ab^{-5}(\mu_i + \mu_o) \sin(2\theta) \\ D = -Ab^{-7} \end{cases} \\
5Ab^{-5} &\begin{cases} \text{steady} : \frac{9\varepsilon_0 k_2 E_\infty^2}{4} \frac{(Rq-1)R}{(2R+1)^2 + a^2 \omega^2 (q+2)^2} \frac{1}{\mu_o(1+m)} \\ \text{unsteady} : \frac{9\varepsilon_0 k_2 E_\infty^2}{4} (Rq-1) \operatorname{Re}[F_\theta^* e^{2i\omega t}] \frac{1}{\mu_o(1+m)} \end{cases} \quad (78) \\
A = A_s + A_T &\begin{cases} A_s = \frac{9\varepsilon_0 k_2 E_\infty^2}{20} \frac{(Rq-1)R}{(2R+1)^2 + a^2 \omega^2 (q+2)^2} \frac{1}{\mu_o(1+m)} \\ A_T = \frac{9\varepsilon_0 k_2 E_\infty^2}{20} (Rq-1) \operatorname{Re}[F_\theta^* e^{2i\omega t}] \frac{1}{\mu_o(1+m)} \end{cases}
\end{aligned}$$

As we know:

$$F_{\theta}^* = \frac{(R + iwa)}{((2R + 1) + ia w (q + 2))^2} = \frac{A + Bi}{(C + Di)^2} \frac{(C - Di)^2}{(C - Di)^2}$$

$$F_{\theta}^* = \frac{AC^2 - AD^2 + 2CDB + i(BC^2 - BD^2 - 2ACD)}{(C^2 + D^2)^2}$$

$$F_{\theta}^* = \frac{O_1 + iO_2}{(C^2 + D^2)^2}$$

$$\begin{cases} O_1 = R(2R + 1)^2 - R w^2 a^2 (q + 2)^2 + 2 w^2 a^2 (q + 2)(q + 1) \\ O_2 = a w (2R + 1)^2 - a^3 w^3 (q + 2)^2 - 2R a w (2R + 1)(q + 2) \end{cases}$$

$$F_{\theta}^* = |F_{\theta}^*| e^{i\theta}$$

$$|F_{\theta}^*| = \frac{\sqrt{O_1^2 + O_2^2}}{(C^2 + D^2)^2} = \frac{\sqrt{R^2 + a^2 w^2}}{(2R + 1)^2 + a^2 w^2 (q + 2)^2}$$

$$\sin(\theta_1) = \frac{\frac{O_2}{(C^2 + D^2)^2}}{|F_{\theta}^*|} = \frac{O_2}{\sqrt{R^2 + a^2 w^2} (2R + 1)^2 + a^2 w^2 (q + 2)^2} \quad (79)$$

$$\cos(\theta_1) = \frac{\frac{O_1}{(C^2 + D^2)^2}}{|F_{\theta}^*|} = \frac{O_1}{\sqrt{R^2 + a^2 w^2} (2R + 1)^2 + a^2 w^2 (q + 2)^2}$$

$$\sin(\theta_1) = \frac{aw \left[(2R + 1)(-2Rq - 2R + 1) - a^2 w^2 (q + 2)^2 \right]}{\sqrt{R^2 + a^2 w^2} (2R + 1)^2 + a^2 w^2 (q + 2)^2}$$

$$\cos(\theta_1) = \frac{R(2R + 1)^2 - a^2 w^2 (q + 2)^2 (Rq - 2R - 2)}{\sqrt{R^2 + a^2 w^2} (2R + 1)^2 + a^2 w^2 (q + 2)^2}$$

$$\begin{aligned}
A_T &= \text{Re}\left(\frac{9\varepsilon_0 k_2 E_\infty^2 b^5}{20\mu_o(1+m)}(Rq-1)\frac{\sqrt{R^2+a^2w^2}}{(2R+1)^2+a^2w^2(q+2)^2}\frac{R}{R}e^{i2wt}e^{\theta}\right) \\
A_T &= A_s \frac{\sqrt{R^2+a^2w^2}}{R} \cos(2wt + \theta_1) \\
u_{\theta\max} &= Ab^{-4} = (A_s + A_T)b^{-4} \Rightarrow A_s b^{-4} + A_T b^{-4} \\
\begin{cases} u_{\theta\max\text{steady}} &= \frac{9\varepsilon_0 k_2 E_\infty^2}{20} \frac{(Rq-1)Rb}{(2R+1)^2+a^2w^2(q+2)^2 \mu_o(1+m)} \\ u_{\theta\max\text{unsteady}} &= u_{\theta\max\text{steady}} \cdot \frac{\sqrt{R^2+a^2w^2}}{R} \cos(2wt + \theta_1) \end{cases}
\end{aligned} \tag{80}$$

$$\begin{aligned}
u_{ri} &= \left(\left(\frac{r}{a}\right) - \left(\frac{r}{a}\right)^3\right) u_{\theta\max} \cdot (3\cos^2(\theta) - 1) \\
u_{ro} &= \left(\left(\frac{a}{r}\right)^4 - \left(\frac{a}{r}\right)^2\right) u_{\theta\max} \cdot (3\cos^2(\theta) - 1) \\
u_{\theta i} &= \left(3\left(\frac{r}{a}\right) - 5\left(\frac{r}{a}\right)^3\right) u_{\theta\max} \cdot \left(-\frac{\sin(2\theta)}{2}\right), \quad u_{\theta o} = \left(\frac{a}{r}\right)^4 u_{\theta\max} \cdot \sin(2\theta)
\end{aligned} \tag{81}$$

In fact, velocity is divided into two parts. The part that is relevant to $T_{r\theta}^e$ and the part that includes T_{rr}^e and interface fluctuation and thus creates a fluctuating current. So far the velocity related to $T_{r\theta}^e$ has been specified. The pressure difference associated with this velocity is obtained through the following relationships.

$$-r^2(u_{ri}) = \left(\left(\frac{r^3}{a}\right) - \left(\frac{r^5}{a^3}\right)\right)u_{\theta\max} \cdot (3\cos^2(\theta) - 1)$$

$$\frac{\partial}{\partial r}() = \left(\left(\frac{3r^2}{a}\right) - \left(\frac{5r^4}{a^3}\right)\right)u_{\theta\max} \cdot (3\cos^2(\theta) - 1)$$

$$\frac{1}{r^2}() = \left(\left(\frac{3}{a}\right) - \left(\frac{5r^2}{a^3}\right)\right)u_{\theta\max} \cdot (3\cos^2(\theta) - 1)$$

$$\frac{\partial}{\partial r}() = \left(-\frac{10r}{a^3}\right)u_{\theta\max} \cdot (3\cos^2(\theta) - 1)$$

$$\frac{\partial u_{ri}}{\partial \theta} = \left(\left(\frac{r}{a}\right) - \left(\frac{r}{a}\right)^3\right)u_{\theta\max} \cdot (-3\sin(2\theta))$$

$$\sin(\theta)() = \left(\left(\frac{r}{a}\right) - \left(\frac{r}{a}\right)^3\right)u_{\theta\max} \cdot (-3\sin(2\theta))\sin(\theta)$$

$$\frac{\partial}{\partial \theta}() = \left(\left(\frac{r}{a}\right) - \left(\frac{r}{a}\right)^3\right)u_{\theta\max} \cdot (-3)(2\cos(2\theta)\sin(\theta) + \cos(\theta)\sin(2\theta)) \quad (82)$$

$$\frac{1}{r^2 \sin(\theta)}() = \left(\left(\frac{1}{ra}\right) - \left(\frac{r}{a^3}\right)\right)u_{\theta\max} \cdot (-3)(2\cos(2\theta) + 2\cos^2(\theta))$$

$$= \left(\left(\frac{1}{ra}\right) - \left(\frac{r}{a^3}\right)\right)u_{\theta\max} \cdot (-6)(3\cos^2(\theta) - 1)$$

$$u_{\theta i} \sin(\theta) = \left(3\left(\frac{r}{a}\right) - 5\left(\frac{r}{a}\right)^3\right)u_{\theta\max} \cdot \left(-\frac{\sin(2\theta)}{2}\right) \cdot \sin(\theta)$$

$$\frac{\partial}{\partial \theta}() = \left(3\left(\frac{r}{a}\right) - 5\left(\frac{r}{a}\right)^3\right)u_{\theta\max} \cdot (2\cos(2\theta)\sin(\theta) + \cos(\theta)\sin(2\theta))$$

$$\frac{-2}{r^2 \sin(\theta)}() = \left(3\left(\frac{1}{ra}\right) - 5\left(\frac{r}{a^3}\right)\right)u_{\theta\max} \cdot (6\cos^2(\theta) - 2)$$

$$= \left(3\left(\frac{1}{ra}\right) - 5\left(\frac{r}{a^3}\right)\right)u_{\theta\max} \cdot 2(3\cos^2(\theta) - 1)$$

$$-\nabla p = \mu \nabla^2 U :$$

$$\nabla = \frac{\partial}{\partial r} \vec{e}_r + \frac{1}{r} \frac{\partial}{\partial \theta} \vec{e}_\theta$$

$$\left\{ \begin{aligned} &\frac{\partial}{\partial r} \left(\frac{1}{r^2} \frac{\partial}{\partial r} (r^2 u_r) \right) + \frac{1}{r^2 \sin(\theta)} \frac{\partial}{\partial \theta} (\sin(\theta) \frac{\partial u_r}{\partial \theta}) - \frac{2}{r^2 \sin(\theta)} \frac{\partial}{\partial \theta} (u_\theta \sin(\theta)) \\ &\left\{ \frac{1}{r^2} \frac{\partial}{\partial r} (r^2 \frac{\partial u_\theta}{\partial r}) + \frac{1}{r^2} \frac{\partial}{\partial \theta} \left(\frac{1}{\sin(\theta)} \frac{\partial (u_\theta \sin(\theta))}{\partial \theta} \right) + \frac{2}{r^2} \frac{\partial u_r}{\partial \theta} \right. \end{aligned} \right. \quad (83)$$

$$\begin{aligned}\frac{\partial p_i}{\partial r} &= \mu_i u_{\theta \max} \cdot (3 \cos^2(\theta) - 1) \frac{-14r}{a^3} \\ p_i(r, \theta) &= \frac{-7r^2}{a^3} \mu_i u_{\theta \max} \cdot (3 \cos^2(\theta) - 1) + \Pi_i\end{aligned}\tag{84}$$

It should be noted that the same results would be achieved if the momentum equation was used in a radial direction. To obtain the pressure outside the droplet, we repeat the process above using external tangential and normal velocities.

$$\begin{aligned}r^2 u_{r\theta} &= \left(\frac{a^4}{r^2} - a^2\right) u_{\theta \max} \cdot (3 \cos^2(\theta) - 1) \\ \frac{\partial}{\partial r}() &= \left(\frac{-2a^4}{r^3}\right) u_{\theta \max} \cdot (3 \cos^2(\theta) - 1) \\ \frac{1}{r^2}() &= \left(\frac{-2a^4}{r^5}\right) u_{\theta \max} \cdot (3 \cos^2(\theta) - 1) \\ \frac{\partial}{\partial r}() &= \left(\frac{10a^4}{r^6}\right) u_{\theta \max} \cdot (3 \cos^2(\theta) - 1) \\ \frac{\partial u_r}{\partial \theta} &= \left(\left(\frac{a}{r}\right)^4 - \left(\frac{a}{r}\right)^2\right) u_{\theta \max} \cdot (-3 \sin(2\theta)) \\ \sin(\theta)() &= \left(\left(\frac{a}{r}\right)^4 - \left(\frac{a}{r}\right)^2\right) u_{\theta \max} \cdot (-3 \sin(2\theta)) \sin(\theta) \\ \frac{\partial}{\partial \theta}() &= \left(\left(\frac{a}{r}\right)^4 - \left(\frac{a}{r}\right)^2\right) u_{\theta \max} \cdot (-6)(3 \cos^2(\theta) - 1) \\ \frac{\sin(\theta)}{r^2} &= \left(\left(\frac{a^4}{r^6}\right) - \left(\frac{a^2}{r^4}\right)\right) u_{\theta \max} \cdot (-6)(3 \cos^2(\theta) - 1) \\ u_{\theta} \sin(\theta) &= u_{\theta \max} \cdot \left(\frac{a}{r}\right)^4 \cdot \sin(2\theta) \sin(\theta) \\ \frac{\partial}{\partial \theta} &= u_{\theta \max} \cdot \left(\frac{a}{r}\right)^4 \cdot 2 \cos(2\theta) \sin(\theta) + \cos(\theta) \sin(2\theta) \\ \frac{-2}{r^2 \sin(\theta)} &= \frac{-2a^4}{r^6} (2 \cos(2\theta) + 2 \cos^2(\theta)) \\ &= \frac{-4a^4}{r^6} (3 \cos^2(\theta) - 1)\end{aligned}\tag{85}$$

$$\frac{\partial p_o}{\partial r} = \mu_o \frac{6a^2}{r^4} u_{\theta \max} \cdot (3 \cos^2(\theta) - 1) \quad (86)$$

$$p_o(r, \theta) = -2\mu_o a^2 r^{-3} u_{\theta \max} \cdot (3 \cos^2(\theta) - 1) + \Pi_o$$

The difference in pressure on the interface is calculated as:

$$p_i(r, \theta) - p_o(r, \theta) = \frac{u_{\theta \max} \cdot (3 \cos^2(\theta) - 1)}{a} (-7\mu_i + 2\mu_o) \quad (87)$$

Given the coefficients in terms of maximum tangential velocities, the hydrodynamic stresses are:

$$\begin{aligned} T_{rr}^h \Big|_{net} &= (3 \cos^2(\theta) - 1) \left[\mu_o (-4Ab^{-5} - 2Bb^{-3}) - \mu_i (C + 3Db^2) \right] \\ T_{rr}^h \Big|_{net} &= (3 \cos^2(\theta) - 1) \left[2\mu_o (-2Ab^{-5}) - 2\mu_i (-2Ab^{-5}) \right] \\ T_{rr}^h \Big|_{net} &= (3 \cos^2(\theta) - 1) 4Ab^{-5} (\mu_i - \mu_o) \\ Ab^{-5} &= \frac{u_{\theta \max}}{b} \Rightarrow \frac{4u_{\theta \max}}{b} (\mu_i - \mu_o) (3 \cos^2(\theta) - 1) \end{aligned} \quad (88)$$

In order to obtain curvature, the total hydrodynamic stress on the interface is required. So that:

$$\begin{aligned} \sigma_{rr}^h &= T_{rr}^h - (p_o - p_i) = \frac{u_{\theta \max}}{b} (3 \cos^2(\theta) - 1) \left[-7\mu_i + 2\mu_o + 4\mu_i - 4\mu_o \right] \\ \sigma_{rr}^h &= -\frac{u_{\theta \max}}{b} (3 \cos^2(\theta) - 1) \left[3\mu_i + 2\mu_o \right] \end{aligned} \quad (89)$$

The velocities resulting from the fluctuation of the interface are obtained through the correction of boundary conditions. So that:

$$\begin{aligned} u_{ri} = u_{ro} &= \frac{\partial r}{\partial t} \\ T_{r\theta}^h \Big|_{net} &= 0. \end{aligned} \quad (90)$$

Since the general deformation is in two parts, $D_s + D_t$ for small deformation, one can write:

$$r = b \left\{ 1 + \frac{2}{3} (D_v + D_T) (3 \cos^2(\theta) - 1) \right\}$$

$$D_T = \text{Re}(H^* e^{2i\omega t}) \Rightarrow \frac{\partial r}{\partial t} = \frac{2b}{3} \text{Re}(2i\omega H^* e^{2i\omega t}) (3 \cos^2(\theta) - 1) \quad (91)$$

$$\frac{\partial r}{\partial t} = \frac{4b\omega}{3} \text{Re}(iH^* e^{2i\omega t}) (3 \cos^2(\theta) - 1)$$

For calculating the velocity constants the boundary conditions above are applied which result in

$$\text{I: } Cb + Db^3 = \frac{4b\omega}{3} \text{Re}(iH^* e^{2i\omega t}) (3 \cos^2(\theta) - 1)$$

$$\text{II: } Ab^{-4} + Bb^{-2} = \frac{4b\omega}{3} \text{Re}(iH^* e^{2i\omega t}) (3 \cos^2(\theta) - 1) \quad (92)$$

$$\text{III: } Cb + Db^3 = Ab^{-4} + Bb^{-2}$$

$$\text{IV: } \mu_o (-8Ab^{-5} - 3Bb^{-3}) = \mu_i (-3C - 8Db^2)$$

$$\text{V: } 2Ab^{-4} = -3Cb - 5Db^3$$

All constants are obtained as a function of A:

$$B = \frac{-A(16\mu_o + 19\mu_i)}{3b^2(2\mu_o + 3\mu_i)},$$

$$C = \frac{-A(19\mu_o + 16\mu_i)}{3b^5(2\mu_o + 3\mu_i)}, \quad (93)$$

$$D = \frac{A(3\mu_o + 2\mu_i)}{b^7(2\mu_o + 3\mu_i)}$$

$$Ab^{-4} + Ab^{-4} \frac{(-16\mu_o - 19\mu_i)}{3(2\mu_o + 3\mu_i)} = \frac{4b\omega}{3} \text{Re}(iH^* e^{2i\omega t})$$

$$Ab^{-4} \left(\frac{-10}{3} \frac{\mu_o + \mu_i}{(2\mu_o + 3\mu_i)} \right) = \frac{4b\omega}{3} \text{Re}(iH^* e^{2i\omega t})$$

$$Ab^{-4} = \frac{2b\omega \text{Re}(iH^* e^{2i\omega t})(2 + 3\overline{m})}{-5(1 + \overline{m})} \quad (94)$$

$$A = b^4 (2 + 3\overline{m}) U_T''(-3), U_T'' = \frac{2}{15} \frac{b\omega \text{Re}(iH^* e^{2i\omega t})}{(1 + \overline{m})}$$

The tangent velocities inside and outside the drop are:

$$\begin{aligned}
u_{\theta o} &= \sin(2\theta)Ar^{-4} = b^4(2+3\bar{m})U_T''(-3)r^{-4}\sin(2\theta) \\
u_{\theta o} &= -6U_T''\sin(\theta)\cos(\theta)b^4r^{-4}(2+3\bar{m}) \\
u_{\theta i} &= \frac{-\cos(\theta)\sin^2(\theta)}{r\sin(\theta)}(3Cr^2+5Dr^4) = -\frac{\sin(2\theta)}{2}(3Cr+5Dr^3) \\
\text{part I :}(3Cr) &= 3r \cdot \frac{-A(19\mu_o+16\mu_i)}{3b^5(2\mu_o+3\mu_i)} = \\
r \cdot b^4(2+3\bar{m})U_T''(3) &\frac{(19\mu_o+16\mu_i)}{b^5(2\mu_o+3\mu_i)} \\
U_T''3(19+16\bar{m})b^{-1}r & \\
\text{part II :}(5Dr^3) &= 5r^3 \frac{A(3\mu_o+2\mu_i)}{b^7(2\mu_o+3\mu_i)} = \\
5r^3 \frac{(3\mu_o+2\mu_i)}{b^7(2\mu_o+3\mu_i)} &b^4(2+3\bar{m})U_T''(-3) = \\
-15U_T''b^{-3}r^3(3+2\bar{m}) & \\
u_{\theta i} = -U_T'' \left[3(19+16\bar{m})b^{-1}r - 15(3+2\bar{m})b^{-3}r^3 \right] &\sin(\theta)\cos(\theta)
\end{aligned} \tag{95}$$

The normal velocities inside and outside the drop are:

$$\begin{aligned}
u_{ni} &= U_T'' \left[(19+16\bar{m})b^{-1}r - 3(3+2\bar{m})b^{-3}r^3 \right] (3\cos^2(\theta)-1) \\
u_{ro} &= U_T'' \left[(19\bar{m}+16)b^2r^{-2} - 3(3\bar{m}+2)b^4r^{-4} \right] (3\cos^2(\theta)-1)
\end{aligned} \tag{96}$$

The resultant normal electric stress on the interface due to the droplet fluctuation is:

$$T_{rr}^h \Big|_{net} = (3\cos^2(\theta)-1) \left[2\mu_o(-4Ab^{-5}-2Bb^{-3}) - 2\mu_i(C+3Db^2) \right] \tag{97}$$

The hydrodynamic pressure inside and outside the droplet and consequently the pressure difference on the interface are:

$$\begin{aligned}
\frac{\partial p_i}{\partial r} &= 14Dr(3\cos^2(\theta)-1), p_i(r,\theta) = \mu_i 7Dr^2(3\cos^2(\theta)-1) + \Pi_i \\
\frac{\partial p_o}{\partial r} &= -6Br^{-4}(3\cos^2(\theta)-1), p_o(r,\theta) = \mu_o 2Br^{-3}(3\cos^2(\theta)-1) + \Pi_o \\
p_i(r,\theta) - p_o(r,\theta) \Big|_{r=b} &= (3\cos^2(\theta)-1) \left[\mu_i 7Db^2 - \mu_o 2Bb^{-3} \right] + \Pi_i - \Pi_o
\end{aligned} \tag{98}$$

The total hydrodynamic stress perpendicular to the interface is:

$$\begin{aligned}
\sigma_r^h &= T_r^h - (p_o - p_i) = \\
&\mu_i 7Db^2 - \mu_o 2Bb^{-3} + 2\mu_o (-4Ab^{-5} - 2Bb^{-3}) - 2\mu_i (C + 3Db^2) \\
&\mu_i (Db^2 - 2C) + \mu_o (-8Ab^{-5} - 6Bb^{-3}) = \frac{A(89\mu_i\mu_o + 38\mu_i^2 + 48\mu_o^2)}{3b^5(2\mu_o + 3\mu_i)} \\
\sigma_r^h &= \frac{A\mu_o^2(89\bar{m} + 38\bar{m}^2 + 48)}{3b^5\mu_o(2 + 3\bar{m})} = \dots \tag{99} \\
&\frac{b^4(2 + 3\bar{m})U_T''(-3)\mu_o^2(89\bar{m} + 38\bar{m}^2 + 48)}{3b^5\mu_o(2 + 3\bar{m})} = \\
\sigma_r^h &= T_r^h - (p_o - p_i) = -U_T''b^{-1}\mu_o(19\bar{m} + 16)(2\bar{m} + 3)(3\cos^2(\theta) - 1)
\end{aligned}$$

4.2 Steady drop deformation

To study the deformation of the droplet in a stable state, the equilibrium of normal stresses can be investigated (Capillary equation):

$$\begin{aligned}
\sigma_{rr}^h \Big|_{net} + T_{rr}^e \Big|_{net} &= \gamma k \\
\sigma_{rr}^h \Big|_{net} &= -u_{\theta \max} b^{-1} (3 \cos^2(\theta) - 1) [3\mu_i + 2\mu_o] + \\
T_{rr}^e \Big|_{net} &= \frac{9E_\infty^2 \varepsilon_0 k_2}{4} \left\{ \frac{(R^2 - 2qR^2 + 1) + a^2 w^2 (q-1)^2}{(2R+1)^2 + a^2 w^2 (q+2)^2} \right\} \cos^2(\theta) + ws \\
u_{\theta \max \text{ steady}} &= \frac{9\varepsilon_0 k_2 E_\infty^2}{20} \frac{(Rq-1)Rb}{(2R+1)^2 + a^2 w^2 (q+2)^2} \frac{1}{\mu_o (1+m)} \\
\sigma_{rr}^h \Big|_{net} &= (3 \cos^2(\theta) - 1) \frac{-9\varepsilon_0 k_2 E_\infty^2}{20} \frac{(Rq-1)R}{(2R+1)^2 + a^2 w^2 (q+2)^2} \frac{(3\bar{m}+2)}{(1+m)} \\
T_{rr}^e \Big|_{net} &\propto \frac{[(R^2 - 2qR^2 + 1) + a^2 w^2 (q-1)^2] \cos^2(\theta) + (q-1)(R^2 + a^2 w^2)}{(2R+1)^2 + a^2 w^2 (q+2)^2} \\
&==== \\
&\frac{9\varepsilon_0 k_2 E_\infty^2}{4} \left[\frac{-\frac{3}{5} (Rq-1)R \frac{(3\bar{m}+2)}{(1+m)} + (R^2 - 2qR^2 + 1) + a^2 w^2 (q-1)^2}{(2R+1)^2 + a^2 w^2 (q+2)^2} \right] \\
\Phi_v &= \left[\frac{-\frac{3}{5} (Rq-1)R \frac{(3\bar{m}+2)}{(1+m)} + (R^2 - 2qR^2 + 1) + a^2 w^2 (q-1)^2}{(2R+1)^2 + a^2 w^2 (q+2)^2} \right] \\
\text{Left : } &\frac{9\varepsilon_0 k_2 E_\infty^2}{4} \Phi_v \cos^2(\theta) + cons = \gamma k
\end{aligned} \tag{100}$$

In order to find the deformation, we consider steady stresses terms on the left side of the equation (time-dependent stresses have no stable term). The droplet radius r is defined as $r = R + \xi(\theta)$, then the curvature relation for the sphere is obtained from the following equation. Below $\xi(\theta) = Rf(x)$ and $x = \cos(\theta)$ are the assumptions.

$$\begin{aligned}
k &= \frac{2}{R} - \frac{2\xi}{R^2} - \frac{1}{R^2} \left\{ \frac{1}{\sin(\theta)} \frac{\partial}{\partial \theta} (\sin(\theta) \frac{\partial \xi}{\partial \theta}) \right\} \\
k &= \frac{1}{R} \left\{ 2 - 2f - \frac{d}{dx} \left[(1-x^2) \frac{df}{dx} \right] \right\}
\end{aligned} \tag{101}$$

The above equation is the second order Legendre equation. To solve this equation with respect to the power series, it is assumed that the answer to the problem is in a form of $f(x) = \sum_{n=0}^{\infty} a_n x^n$. And the convergence range is between -1 and 1. Substituting this series in the Capillary equation yields

$$\begin{aligned}
f(x) &= \sum_{n=0}^{\infty} a_n x^n \\
k &= \frac{\gamma}{R} \left\{ 2 - 2f - \frac{d}{dx} \left[(1-x^2) \frac{df}{dx} \right] \right\} = \alpha x^2 + \beta x + \text{const} \\
2 - 2f - f''(1-x^2) + 2xf' &= \alpha x^2 + \beta x + \text{const} \\
f(x) &= \sum_{n=0}^{\infty} a_n x^n, f'(x) = \sum_{n=1}^{\infty} a_n n x^{n-1}, f''(x) = \sum_{n=2}^{\infty} a_n n(n-1) x^{n-2} \\
2 - 2 \sum_{n=0}^{\infty} a_n x^n - \sum_{n=2}^{\infty} a_n n(n-1) x^{n-2} + \sum_{n=2}^{\infty} a_n n(n-1) x^n + 2 \sum_{n=1}^{\infty} a_n n x^n &= \dots \\
2 - 2a_0 - 2a_1 x - 2a_2 x^2 - 2 \sum_{n=3}^{\infty} a_n x^n - 2a_2 - 6a_3 x & \\
-12a_4 x^2 - \sum_{n=5}^{\infty} a_n n(n-1) x^{n-2} + 2a_2 x^2 + \sum_{n=3}^{\infty} a_n n(n-1) x^n + & \\
2a_1 x + 4a_2 x^2 + 2 \sum_{n=3}^{\infty} a_n n x^n & \\
\sum_{n=5}^{\infty} a_n n(n-1) x^{n-2} = \sum_{n=3}^{\infty} a_{n+2} (n+2)(n+1) x^n & \\
\sum_{n=3}^{\infty} [-a_{n+2} (n+2)(n+1) - 2a_n + a_n n(n-1) + 2a_n n] x^n & \\
\sum_{n=3}^{\infty} [-a_{n+2} (n+2)(n+1) + a_n (n^2 + n - 2)] x^n + 2 - 2a_0 - 2a_2 - 6a_3 x & \\
-12a_4 x^2 + 4a_2 x^2 &
\end{aligned} \tag{102}$$

Given that there is no x^4 on the right side,

$$\begin{aligned}
a_4 &= 0.0 \\
4 \frac{a_2 \gamma}{R} &= \alpha \Rightarrow a_2 = \frac{\alpha R}{4\gamma} \\
-6 \frac{a_3 \gamma}{R} &= \beta \Rightarrow a_3 = \frac{-\beta R}{6\gamma}
\end{aligned} \tag{103}$$

The radius of the droplet in the form of Legendre polynomials is defined as

$$\begin{aligned}
r &= B \cdot \frac{3x^2 - 1}{2}, \quad x^2 : \frac{3B}{2} = a_2 \Rightarrow B = \frac{2a_2}{3} \\
x^0 : \frac{-B}{2} &= a_0 = \frac{-a_2}{3}, \quad r = \frac{a_2}{3} (3x^2 - 1), \quad a_{n+2} = a_n \frac{n-1}{n+1} \geq 3
\end{aligned} \tag{104}$$

$$\begin{aligned}
\frac{9\varepsilon_0 k_2 E_\infty^2}{4} \Phi_\nu &= \frac{4a_2 \gamma}{R} = \frac{8D\gamma}{R} \\
D_s &= \frac{9\varepsilon_0 k_2 E_\infty^2}{32} \Phi_\nu = \frac{9\varepsilon_0 k_2 \bar{E}_\infty^2}{16} \Phi_\nu
\end{aligned} \tag{105}$$

For frequency of zero, the frequency response for the zero frequency should be calculated and also the sum of the responses should be introduced as zero frequency. Therefore, we will have a total of two to 9/32 or 16.9, so with the replacement of $\bar{E} = E_\infty / \sqrt{2}$, D_s is achieved. By doing this, it is not necessary to calculate the frequency part at $w = 0$ to get the answer at zero frequency. The deformation function Φ changes in frequency when Φ_ν is zero, so $D = 0$ and as a result of the shape of the droplet remains spherical. Therefore, the droplet will oscillate around its spherical shape in terms of frequency w . The droplet remains spherical in a specific frequency. In order to obtain this critical frequency, the expression Φ is equal to zero. So that:

$$\begin{aligned}
\Phi_\nu &= 0.0 \Rightarrow \\
v_c &= \frac{\sqrt{5(1+\bar{m})(16qR^2 + 19R^2 q\bar{m} - 6R - 9R\bar{m} - 5R^2 - 5R^2\bar{m} - 5 - 5\bar{m})}}{5(1+\bar{m})b|q-1|}
\end{aligned} \tag{106}$$

The condition for the existence of an answer to the critical frequency of the positive is the phrase inside the radical. So:

$$\begin{aligned}
& R^2 \left[q(19\bar{m} + 16) - 5(1 + \bar{m}) \right] - 3R(3\bar{m} + 2) - 5(1 + \bar{m}) \geq 0.0 \div R; \\
& R \left[q(19\bar{m} + 16) - 5(1 + \bar{m}) \right] - 3(3\bar{m} + 2) - \frac{5(1 + \bar{m})}{R} \\
& Rq(19\bar{m} + 16) - 5R(1 + \bar{m}) - 3(3\bar{m} + 2) - \frac{5(1 + \bar{m})}{R} \\
& Rq - \frac{5(R + \frac{1}{R})(1 + \bar{m})}{(19\bar{m} + 16)} - \frac{3(3\bar{m} + 2)}{(19\bar{m} + 16)} \geq 0.0 \\
& Rq \geq \frac{5(R + \frac{1}{R})(1 + \bar{m})}{(19\bar{m} + 16)} + \frac{3(3\bar{m} + 2)}{(19\bar{m} + 16)} \geq 1 + \alpha \tag{107} \\
& \alpha = \frac{5(R + \frac{1}{R})(1 + \bar{m}) + 9\bar{m} + 6 - 19\bar{m} - 16}{(19\bar{m} + 16)} \Rightarrow \\
& \alpha = \frac{5(1 + \bar{m})}{(19\bar{m} + 16)} \left(R + \frac{1}{R} - 2 \right) \Rightarrow \frac{5(1 + \bar{m})}{(19\bar{m} + 16)R} (R - 1)^2 \\
& Rq \geq 1 + \frac{5(1 + \bar{m})(R - 1)^2}{(19\bar{m} + 16)R}
\end{aligned}$$

When $q = 1$, that is, the electrical diffusivity of the droplet and the surrounding area is the same and more frequencies are needed to keep the droplet in a spherical state. Also, when $Rq > 1$, the increase in the frequency the deformation of the droplet increases. In $Rq = 1$ and $\Phi_v = (q - 1/q + 2)^2$ indicates that the drop shape is independent of the applied frequency. As the obtained relation for the critical frequency shows, three different classes for the fluids under investigation can be defined (through the drawing of q diagram in R). According to Figure 19, three types of areas are defined as

$$\begin{aligned}
A : Rq \leq 1, \frac{\partial D_v}{\partial \nu} \leq 0.0, D_v \geq 0.0 \\
B : 1 < Rq < 1 + \frac{5(1+\bar{m})(R-1)^2}{(19\bar{m}+16)R}, \frac{\partial D_v}{\partial \nu} > 0.0, D_v > 0.0 \\
C : Rq \geq 1 + \frac{5(1+\bar{m})(R-1)^2}{(19\bar{m}+16)R}, \frac{\partial D_v}{\partial \nu} > 0.0, \begin{cases} \nu > \nu_c & D_v > 0.0 \\ \nu < \nu_c & D_v < 0.0 \end{cases}
\end{aligned} \tag{108}$$

As seen in the figure, in the very high electrical conductivity ratio, q is toward $5(1+\bar{m})/(16+19\bar{m})$ and the AB line towards zero is desired. For both AB and BC lines, BC leads to infinity in a low conductivity resulting in q goes toward infinity. Therefore, the rate of deformation of the droplet depends on the ratio R , q and λ . But the effect of \bar{m} is negligible, so that between the zero viscosity and the infinity, the difference is very small in the BC line. The deformation rate is obtained at zero and infinite frequencies as follows:

$$\begin{aligned}
\nu = 0.0 \Rightarrow \Phi_0 &= \frac{-3 R (Rq - 1)(2 + 3\bar{m})}{5(1 + \bar{m})} + R^2 - 2qR^2 + 1 \\
&\quad (2R + 1)^2 \\
\nu \rightarrow \infty \Rightarrow \Phi_\infty &= \frac{q^2 - 2q + 1}{q^2 + 4q + 4} = \left(\frac{q-1}{q+2}\right)^2
\end{aligned} \tag{109}$$

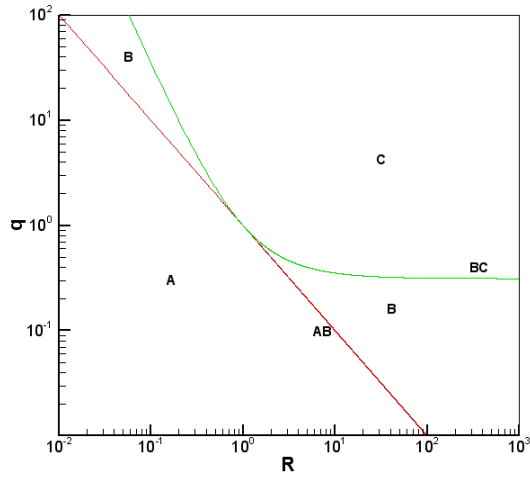


Figure 19. Different areas associated with the deformation of the drop at a critical frequency.

Table 1 shows the electrical properties related to the graphs displayed in Figure 20.

Table 1. Electrical properties related to Figure 20.					
System	R	q	\bar{m}	Φ_0	Φ_∞
a	0.1	3	0.1	0.72	0.16
b	10	0.2	0.1	0.10987	0.1322
c	100	1	0.1	-0.55491	0
d	100	3	0.1	-2.16603	0.16

As shown in Figure 20, the a diagram, which belongs to the A-domain, always has the prolate shape and decreases with increasing frequency of deformation. The b diagram, which belongs to region B, has the same trend, but at lower frequency has smaller deformation compared to region A. The graphs c, d both belong to region C, where the droplet is oblate at a zero frequency, but as the frequency increases, the deformation decreases until finally reach zero. This point is the same as

the critical frequency. As the frequency increases, the amount of deformation from $\Phi_v < 0$ goes to $\Phi_v > 0$, indicating that the droplet is prolate and increases along the path with increasing deformation frequency.

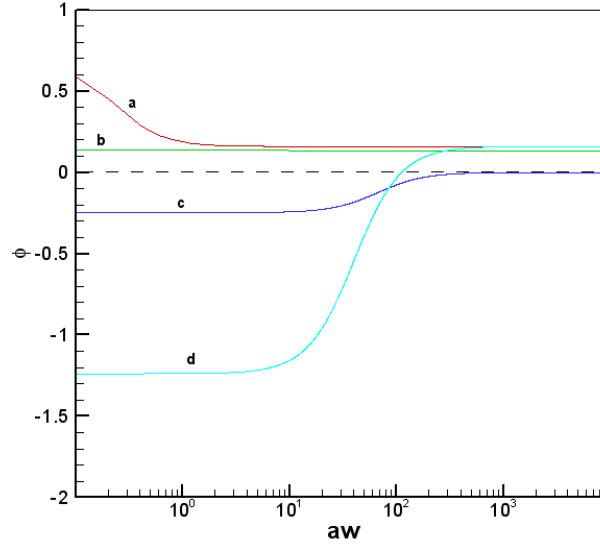


Figure 20. Deformation form with increasing frequency for different areas.

4.3 Transient droplet deformation:

To investigate general deformation and oscillatory deformation, it is necessary to neutralize the general oscillatory normal stress on the interface by surface tension. Considering transient parts, we will have normal stresses as

$$\begin{aligned}
 \text{I: } \sigma_{rr}^h &= -u_{\theta_{\max}} b^{-1} (3 \cos^2(\theta) - 1) [3\mu_i + 2\mu_o] \\
 \text{II: } \sigma_{rr}^h &= -U_T'' b^{-1} \mu_o (19\bar{m} + 16)(2\bar{m} + 3)(3 \cos^2(\theta) - 1)
 \end{aligned} \tag{110}$$

$$\begin{aligned}
U_T^u &= \frac{2}{15} \frac{bw \operatorname{Re}(iH^* e^{2iwt})}{(1+m)} \cdot T_{rr}^e \Big|_{unsteady} = \frac{9E_\infty^2 \varepsilon_0 k_2}{4} \operatorname{Re}[F_r^* e^{2iwt} \cos^2(\theta)] + wt \\
u_{\theta \max unsteady} &= u_{\theta \max steady} \cdot \frac{\sqrt{R^2 + a^2 w^2}}{R} \cos(2wt + \theta_1) \\
u_{\theta \max unsteady} &= \frac{9\varepsilon_0 k_2 E_\infty^2}{20} (Rq - 1) \operatorname{Re}[F_\theta^* e^{2iwt}] \frac{b}{\mu_o (1+m)}
\end{aligned} \tag{111}$$

coefficients : $\cos^2(\theta)$:

$$\begin{aligned}
I &\rightarrow -b^{-1} u_{\theta \max} 3[3\mu_i + 2\mu_o] \\
&\quad - \frac{9\varepsilon_0 k_2 E_\infty^2}{20} (Rq - 1) \operatorname{Re}[F_\theta^* e^{2iwt}] \frac{b b^{-1} 3[3\mu_i + 2\mu_o]}{\mu_o (1+m)} \\
II &\rightarrow -U_T^u b^{-1} \mu_o (19\bar{m} + 16)(2\bar{m} + 3)3 \\
&\quad - \frac{2}{15} \frac{bw \operatorname{Re}(iH^* e^{2iwt})}{(1+m)} b^{-1} \mu_o (19\bar{m} + 16)(2\bar{m} + 3)3 \\
III &\rightarrow \frac{9E_\infty^2 \varepsilon_0 k_2}{4} \operatorname{Re}[F_r^* e^{2iwt}] \\
&\quad \text{-----} \operatorname{Re}[(\dots) e^{2iwt}] \\
&\quad \left(\frac{9E_\infty^2 \varepsilon_0 k_2}{4} \left[F_r^* - \frac{3}{5} (Rq - 1) F_\theta^* \frac{3\bar{m} + 2}{(1+m)} \right] - \frac{6}{15} w \frac{(19\bar{m} + 16)(2\bar{m} + 3)}{(1+m)} \right) \\
&\quad \cos^2(\theta) \operatorname{Re} \left[\frac{9E_\infty^2 \varepsilon_0 k_2}{4} \left[F_r^* - \lambda_1 (Rq - 1) F_\theta^* \right] - 8w \mu_o i \lambda_2 H^* \right] e^{2iwt} \\
&\quad \left\{ \begin{aligned} \lambda_1 &= \frac{3}{5} \frac{3\bar{m} + 2}{(1+m)}, \lambda_2 = \frac{(19\bar{m} + 16)(2\bar{m} + 3)}{20(1+m)} \\ \gamma k &= \frac{\gamma 8 D_T}{R}, D_T = \operatorname{Re}(H^* e^{2iwt}) \end{aligned} \right.
\end{aligned} \tag{112}$$

$$\begin{aligned}
\frac{9E_\infty^2 \varepsilon_0 k_2}{4} \left[F_r^* - \lambda_1 (Rq - 1) F_\theta^* \right] &= \left(\frac{8\gamma}{R} + 8w \mu_o i \lambda_2 \right) H^* \\
9E_\infty^2 \varepsilon_0 k_2 \left[F_r^* - \lambda_1 (Rq - 1) F_\theta^* \right] &= \frac{32H^* \gamma}{R} \left(\frac{w \mu_o i \lambda_2 R}{\gamma} + 1 \right) \\
K = \frac{w \mu_o R}{\gamma}, H^* &= \frac{9E_\infty^2 \varepsilon_0 k_2}{32\gamma} \frac{F_r^* - \lambda_1 (Rq - 1) F_\theta^*}{1 + Ki \lambda_2}
\end{aligned} \tag{113}$$

$$h^* = \frac{F_r^* - \lambda_1(Rq - 1)F_\theta^*}{1 + Ki \lambda_2}, H^* = \frac{9E_\infty^2 \varepsilon_0 k_2}{32\gamma} h^* \quad (114)$$

$$D_T = \text{Re}(H^* e^{2iwt}) = \frac{9E_\infty^2 \varepsilon_0 k_2}{32\gamma} \text{Re}(h^* e^{2iwt}),$$

$$1 + Ki \lambda_2 = \sqrt{1 + K^2 \lambda_2^2} \exp(i \alpha_1),$$

$$h^* = F_r^* + \lambda_1(-Rq + 1)F_\theta^* \exp(-i \alpha_1), \alpha_1 = \tan^{-1}(K \lambda_2)$$

$$A = a_1 + i b_1 \begin{cases} a_1 = \frac{R(2R + 1) + w^2 a^2 (q + 2)}{(2R + 1)^2 + w^2 a^2 (q + 2)^2} \\ b_1 = \frac{aw(1 - Rq)}{(2R + 1)^2 + w^2 a^2 (q + 2)^2} \end{cases}$$

$$F_r^* = A^2(5 - 2q) - 4A + 1 = \alpha_1 + i \beta_1 \quad (115)$$

$$F_r^* = \alpha_1 + i \beta_1 \begin{cases} \alpha_1 = 2qb_1^2 - 2qa_1^2 - 4a_1 + 5a_1^2 - 5b_1^2 + 1 \\ \beta_1 = 10a_1b_1 - 4a_1b_1q - 4b_1 \end{cases}$$

$$F_\theta^* = \frac{(R + iwa)}{((2R + 1) + iaw(q + 2))^2} = \alpha_2 + i \beta_2 \begin{cases} \alpha_2 = \frac{O_1}{(\alpha'^2 + \beta'^2)} \\ \beta_2 = \frac{O_2}{(\alpha'^2 + \beta'^2)} \end{cases}$$

$$\begin{cases} O_1 = R(2R + 1)^2 - R w^2 a^2 (q + 2)^2 + 2w^2 a^2 (q + 2)(q + 1) \\ O_2 = aw(2R + 1)^2 - a^3 w^3 (q + 2)^2 - 2Raw(2R + 1)(q + 2) \end{cases}$$

$$(\alpha'^2 + \beta'^2) = [(2R + 1)^2 + w^2 a^2 (q + 2)^2]^2$$

where D_t is a function of H^* and e^{2iwt} , none of which is a function of the angle, and since we have a derivative of the curvature with respect to the angle, then D_t has the same form as D_s . To acquire a relationship for D_t ,

$$h^* = (\alpha_1 + i \beta_1) - \lambda_1 (Rq - 1)(\alpha_2 + i \beta_2)$$

$$\text{real part} : \alpha_1 + \alpha_2 \lambda_1 (Rq - 1)$$

$$\text{imaginary part} : \beta_1 + \beta_2 \lambda_1 (Rq - 1)$$

$$h^* = \text{Re} \left[\frac{(\text{Re}^2 + \text{IM}^2)^{\frac{1}{2}}}{\sqrt{1 + K^2 \lambda_2^2}} \cdot \exp(-i \alpha_1) \cdot \exp(i \alpha_2) \cdot \exp(2i \omega t) \right], \quad (116)$$

$$\alpha_2 = \tan^{-1} \left(\frac{\text{IM}}{\text{Re}} \right), \quad I = (\text{Re}^2 + \text{IM}^2)^{\frac{1}{2}}, \quad \alpha_{\text{total}} = \alpha_2 - \alpha_1 + 2\omega t$$

$$D_{\text{Transient}} = \frac{9E_{\infty}^2 \varepsilon_0 k_2 b}{32\gamma} \cdot \frac{I}{\sqrt{1 + K^2 \lambda_2^2}} \cos(\alpha_{\text{total}})$$

$$D_{\text{Total}} = D_S + D_T = \frac{9E_{\infty}^2 \varepsilon_0 k_2 b}{32\gamma} \cdot \Phi_v + \frac{9E_{\infty}^2 \varepsilon_0 k_2 b}{32\gamma} \cdot \frac{I}{\sqrt{1 + K^2 \lambda_2^2}} \cos(\alpha_{\text{total}})$$

$$D_{\text{Total}} = \frac{9E_{\infty}^2 \varepsilon_0 k_2 b}{32\gamma} \left[\Phi_v + \frac{I \cos(\alpha_{\text{total}})}{\sqrt{1 + K^2 \lambda_2^2}} \right], \quad (117)$$

$$\Phi_{\text{Total}} = \Phi_v + \frac{I \cos(\alpha_{\text{total}})}{\sqrt{1 + K^2 \lambda_2^2}}$$

$$D_{\text{Total}} = \frac{9E_{\infty}^2 \varepsilon_0 k_2 b}{32\gamma} \Phi_{\text{Total}}, \quad \frac{D_T}{D_S} = \frac{I \cos(\alpha_{\text{total}})}{\Phi_v \sqrt{1 + K^2 \lambda_2^2}}$$

$$U_T^{\text{II}} = \frac{2 \text{bw} \text{Re}(iH^* e^{2i\omega t})}{15(1+m)} = \frac{2 \text{bw} \text{Re}(\exp(i \frac{\pi}{2}) H^* e^{2i\omega t})}{15(1+m)}$$

$$U_T^{\text{II}} = \frac{2\text{bw}}{15(1+m)} \cdot \frac{9E_{\infty}^2 \varepsilon_0 k_2 b}{32\gamma} \cdot \frac{I}{\sqrt{1 + K^2 \lambda_2^2}} \cos(\alpha_{\text{total}} + \frac{\pi}{2}) \quad (118)$$

$$\cos(\alpha_{\text{total}} + \frac{\pi}{2}) = -\sin(\alpha_{\text{total}})$$

$$U_T^{\text{II}} = \frac{-3 E_{\infty}^2 \varepsilon_0 k_2 b}{80 \mu_o} \frac{2KI}{\sqrt{1 + K^2 \lambda_2^2}} \sin(\alpha_{\text{total}})$$

The dimensionless number K represents the oscillatory hydrodynamic stress ($\omega \mu_o$) and $\frac{\gamma}{b}$ the

Capillary pressure on the surface of the droplet. When $\frac{\gamma}{b}$ is constant and the frequency goes to

infinity, the value D_t/D_s goes to zero, which indicates that the drop does not respond to radial oscillation stresses. Figure 21 shows the overall deformation relative to w_t . For higher K values, the oscillation of interface is very low, and, conversely, for smaller values, the general deformation takes a more oscillating state, so that in e mode it is greater than D_s and the droplet fluctuates between the prolate and the oblate states. Drop oscillation is twice the voltage fluctuation. When K approaches zero (eg, c), the maximum and minimum oscillation values occur where the electric field is maximized and minimized. Meanwhile, u_T^{II} has a phase difference of 90 degrees with D_t . It should be noted that for conductive drops in the dielectric field, the electrical resistivity of the droplet is very small and the electrical resistance of the surrounding fluid is very high, thus $R = 0$, $X_2 = \infty$ and the electric charge on the droplet is:

$$\sigma = \frac{3\varepsilon_0 k_2 E_\infty \cos(\theta)}{\sqrt{1+a^2 w^2 (q+2)^2}} \cos(\omega t - \theta_t), \theta_t = \tan^{-1}(aw(q+2)) \quad (119)$$

If the conductive drop is placed in the alternating field with a frequency of zero, then the rate of deformation of the droplet in a stable state is:

$$\sigma = 3\varepsilon_0 k_2 E_\infty \cos(\theta) \quad (120)$$

In the above relationship, moving electrical charge on the interface due to the flow of fluid flow and the electrical conductivity of the interface layer is not considered. From this relations, we obtained the stable deformation of the droplet as follows:

$$\begin{aligned} D_s \Big|_{\nu=0, R=0} &= \frac{9\varepsilon_0 k_2 (\overline{E_\infty}^2 b)}{16\gamma} \Phi_\nu \\ D_s &= m_\nu \overline{E_\infty}^2 b, m_\nu = \frac{9\varepsilon_0 k_2}{16\gamma} \Phi_\nu \end{aligned} \quad (121)$$

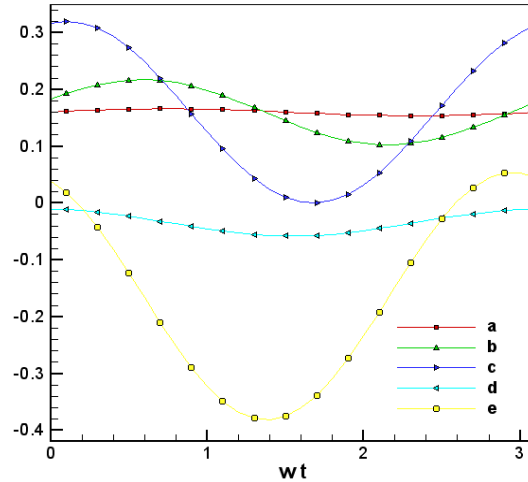


Figure 21. Total deformation function in terms of time for $R=100$, $\lambda = 0.1$, $aw=1E4$,
a) $k=10$, b) $k=1$, and c) $k=0.1$, d) $aw=1E2$, $k=10$, e) $aw=1E2$, $k=1$

As mentioned earlier, for $Rq < 1$, the environment is silicon oil (system 1) as shown in Table 2. An increase in frequency reduces the deformation of the droplet. As the frequency increases to 60 Hz, the drop deformation decreases compared to that of zero frequency. For a conductive drop (system 2), water that comes with an additive, there is no difference between the frequency of 60 and zero, and the shape of the drop is prolate. In (system 3), where $Rq > 1$, for example, a droplet of silicone oil, then the deformation of the droplet at a zero frequency is oblate and at a frequency of 60, the prolate. According to the relations obtained in this system, there is certainly a critical frequency in which the degree of deformation is zero. If the ratio m_v/m_{60} is plotted in terms of the frequency for system 3 then $\nu_c = 1.6063 Hz$ is obtained in which the droplet remains in a spherical state (Figure 22), and after almost frequency of 5 results in infinite frequency, which has the same deformation as that in the frequency of 60. In addition, the proposed relationship for the critical frequency indicates that this frequency does not depend on the diameter of the droplet. An increase in the electric field causes an increase in the deformation of the droplet until the other surface tension is able to balance the normal stresses and the moment of separation begins.

Table 2. The three studied cases (systems).								
N.System (NM3)	phasesD/C	$\gamma(Nm^{-1})$	\bar{m}	K ₂	q	$\chi_1(\Omega m)$	a(s)	R
1	(NM3)	5.5E-3	1.2	2.77	2.3	1E9	2.4E-2	<0.03
N: oxidized castor oil		$\rho = 0.98gr / cm^2$		$\mu = 65(kg / ms)$				
M3: siliconoil(200F)		$\rho = 0.98gr / cm^2$		$\mu = 54(kg / ms)$				
N.System (YN)	phasesD/C	$\gamma(Nm^{-1})$	\bar{m}	K ₂	q	$\chi_1(\Omega m)$	a(s)	R
2	(YN)	13E-3	1E-4	6.30	12.7	1E4	5.6E-7	1E-5
Y: distilled water		$\rho = 1gr / cm^2$		$\mu = 1E^{-6}(kg / ms)$				
(N): oxidized castoroil		$\rho = 0.98gr / cm^2$		$\mu = 65(kg / ms)$				
N.System (MiT)	phasesD/C	$\gamma(Nm^{-1})$	\bar{m}	K ₂	q	$\chi_1(\Omega m)$	a(s)	R
3	(MiT)	3.9	3E-2	6.04	0.46	3E10	1.6	14
Mi: siliconoil(500F)		$\rho = 1gr / cm^2$		$\mu = 0.5(kg / ms)$				
(T): sextolphthalete		$\rho = 1.04gr / cm^2$		$\mu = 174(kg / ms)$				

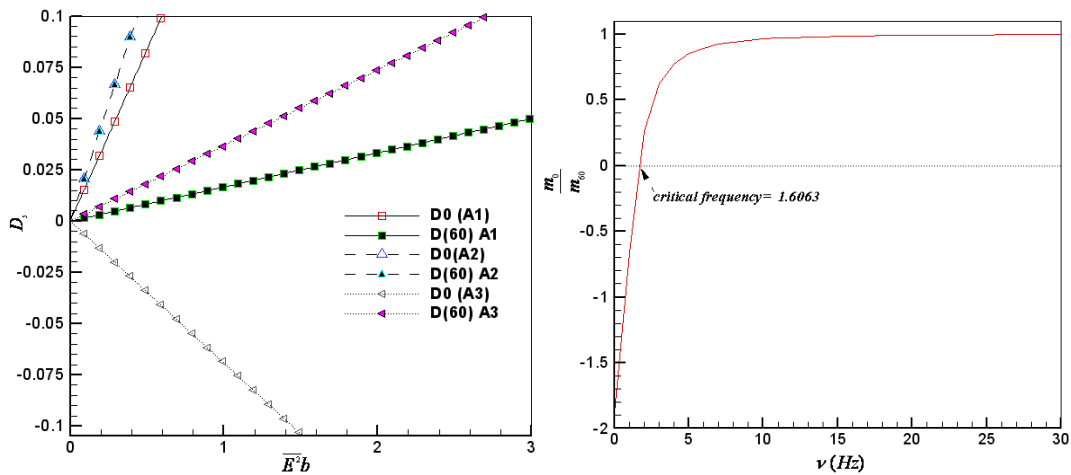


Figure 22. Deformation rate of the field in two modes of zero and 60 (left) and deformation ratio at each frequency to deformation at a frequency of 60 (right).

4.4 Falling drops

The relationships presented in previous sections are true for stationary droplets, considering the probability of errors such as:

1. Assumptions in the boundary conditions.
2. The effect of free current in space that is set to zero but may in fact still exist in the environment.
3. The effect of the ion distribution layer on the interface.
4. Error in electric and hydrodynamic constants such as electrical conductivity, diffusibility, surface tension and etc.
5. The effect of the convection term on the Navier Stokes equation.

When the drop falling or bubble is rising, the fluid hydrodynamics of the surrounding area and the electric field affect them together. This means that in the absence of an electric field, it is possible to imagine the deformation of the droplet, vortex, and fluid rotation. It should be noted that in the equations in this chapter, if the viscosity ratio is very high, it can be an indication of a particle, and if the viscosity ratio is to zero, it should have a bubble. For a falling drop, we can solve the problem from the point of view (coordinates corresponding to the drop). That is, assume that the droplet is constant, but the surrounding fluid in the infinity moves upward; as a result:

$$\begin{aligned}
 u_{r_0} &= U_{\infty} \cos(\theta) , u_{\theta_0} = -U_{\infty} \sin(\theta) \\
 \begin{cases} \frac{\partial \psi}{\partial \theta} = r^2 U_{\infty} \cos(\theta) \sin(\theta) \\ \frac{\partial \psi}{\partial r} = r U_{\infty} \sin^2(\theta) \end{cases} &\Rightarrow \psi_{\infty} = \frac{1}{2} r^2 U_{\infty} \sin^2(\theta) \quad (122)
 \end{aligned}$$

In Stokes regime, thus $\nabla^4 \psi = 0$. Given the form of the received external stream function, it is justified to assume that the stream function is assumed to be $\psi = G(r) \sin^2(\theta)$.

$$\begin{aligned}
\psi(r, \theta) &= G(r) \sin^2(\theta), \nabla^2 = \psi_{rr} + \frac{1-x^2}{r^2} \psi_{xx} \\
\nabla^2 &= G''(1-x^2) + \frac{1-x^2}{r^2} (-2G) = (1-x^2) \left[G'' - \frac{2G}{r^2} \right] \\
\frac{\partial \nabla^2 \psi}{\partial r} &= (1-x^2) \left[G''' - 2 \left(\frac{-2G}{r^3} + \frac{G'}{r^2} \right) \right] \\
\frac{\partial^2 \nabla^2 \psi}{\partial r^2} &= (1-x^2) \left[G'''' - 2 \left(\frac{-2G'}{r^3} + \frac{6G}{r^4} + \frac{G''}{r^2} + \frac{-2G'}{r^3} \right) \right] \\
\frac{\partial^2 \nabla^2 \psi}{\partial x^2} &= -2 \left[G'' - \frac{2G}{r^2} \right]
\end{aligned} \tag{123}$$

$$\begin{aligned}
\nabla^4 \psi &= (1-x^2) \left[G'''' - \frac{2G''}{r^2} + \frac{4G'}{r^3} + \frac{4G'}{r^3} - \frac{12G}{r^4} - \frac{2G''}{r^2} + \frac{4G}{r^4} \right] \\
\nabla^4 \psi &= (1-x^2) \left[G'''' - \frac{4G''}{r^2} + \frac{8G'}{r^3} - \frac{8G}{r^4} \right] = 0 \times r^4 \\
r^4 G'''' - 4r^2 G'' + 8rG' - 8G &= 0.0 \\
\lambda(\lambda-1)(\lambda-2)(\lambda-3) - 4\lambda(\lambda-1) + 8\lambda - 8 &= 0.0 \\
\lambda &= -1, 1, 2, 4
\end{aligned} \tag{124}$$

The above equation is a Cauchy-Euler equation which according to the roots obtained, the bases of the answer are as follows.

$$\begin{aligned}
\psi &= (Ar^4 + Br^2 + Cr + Dr^{-1}) \sin^2(\theta) \\
\begin{cases} u_r = \frac{(Ar^4 + Br^2 + Cr + Dr^{-1})}{r^2 \sin(\theta)} 2 \sin(\theta) \cos(\theta) \\ u_r = (Ar^2 + B + Cr^{-1} + Dr^{-3}) 2 \cos(\theta) \end{cases} \\
\begin{cases} u_\theta = \frac{-(4Ar^3 + 2Br + C - Dr^{-2})}{r \sin(\theta)} \sin^2(\theta) \\ u_\theta = -(4Ar^2 + 2B + Cr^{-1} - Dr^{-3}) \sin(\theta) \end{cases}
\end{aligned} \tag{125}$$

Due to the fact that the velocity inside the droplet must be limited, therefore, C and D are zero for the internal stream function. Meanwhile, when we move away from the droplet, the speed must be limited so that the coefficient A is zero for the external stream function.

$$\begin{aligned}
\psi_i'' &= (A_i r^4 + B_i r^2) \sin^2(\theta) \\
\psi_o'' &= (B_o r^2 + C_o r + D_o r^{-1}) \sin^2(\theta)
\end{aligned} \tag{126}$$

According to the obtained form for the flow and velocity function, we will have:

$$\begin{aligned}
u_{ri} &= (A_i r^2 + B_i) 2 \cos(\theta) \\
u_{\theta i} &= -(4A_i r^2 + 2B_i) \sin(\theta) \\
u_{ro} &= (B_o + C_o r^{-1} + D_o r^{-3}) 2 \cos(\theta) \\
u_{\theta o} &= -(2B_o + C_o r^{-1} - D_o r^{-3}) \sin(\theta)
\end{aligned} \tag{127}$$

Now boundary conditions are applied:

$$\begin{aligned}
BC_1: r \rightarrow \infty & \begin{cases} u_{ro} = U_{fall} \cos(\theta) = -2B_o \cos(\theta) \\ u_{\theta o} = -U_{fall} \sin(\theta) = -2B_o \sin(\theta) \end{cases} \Rightarrow B_o = \frac{U_{fall}}{2} \\
BC_2: r \rightarrow b & \begin{cases} u_{ri} = 0.0 \rightarrow A_i b^2 + B_i = 0.0 \\ u_{ro} = 0.0 \rightarrow (B_o + C_o b^{-1} + D_o b^{-3}) = 0.0 \end{cases} \\
BC_3: u_{\theta i} = u_{\theta o} & \Rightarrow (4A_i b^2 + 2B_i) = (2B_o + C_o b^{-1} - D_o b^{-3})
\end{aligned} \tag{128}$$

Three unknowns are obtained as a function of A_i :

$$\begin{aligned}
B_i &= -A_i b^2, \quad D_o b^{-4} = \frac{U_{fall}}{4b} - A_i b, \\
C_o &= -B_o b - D_o b^{-2} = \frac{b}{2} (2A_i b^2 - 3B_o)
\end{aligned} \tag{129}$$

It should be noted that the tangential electric stress on the interface is zero and the tangential hydrodynamics stresses are:

$$T_{r\theta}^h = \mu \left\{ r \frac{\partial}{\partial r} \left(\frac{u_\theta}{r} \right) + \frac{1}{r} \frac{\partial u_r}{\partial \theta} \right\}$$

outside :

$$\frac{u_\theta}{r} = -(2B_o r^{-1} + C_o r^{-2} - D_o r^{-4}) \sin(\theta)$$

$$\frac{\partial}{\partial r} () = -(-2B_o r^{-2} - 2C_o r^{-3} + 4D_o r^{-5}) \sin(\theta)$$

$$r() = -(-2B_o r^{-1} - 2C_o r^{-2} + 4D_o r^{-4}) \sin(\theta)$$

$$\frac{\partial u_r}{\partial \theta} = -(B_o + C_o r^{-1} + D_o r^{-3}) 2 \sin(\theta)$$

$$\frac{1}{r} () = -(B_o r^{-1} + C_o r^{-2} + D_o r^{-4}) 2 \sin(\theta)$$

$$T_{r\theta out}^h = -\mu_o [6D_o r^{-4}] \sin(\theta)$$

(130)

inside :

$$\frac{u_\theta}{r} = -(4A_i r + 2B_i r^{-1}) \sin(\theta)$$

$$\frac{\partial}{\partial r} () = -(4A_i - 2B_i r^{-2}) \sin(\theta)$$

$$r() = -(4A_i r - 2B_i r^{-1}) \sin(\theta)$$

$$\frac{\partial u_r}{\partial \theta} = -(A_i r^2 + B_i) 2 \sin(\theta)$$

$$\frac{1}{r} () = -(A_i r + B_i r^{-1}) 2 \sin(\theta)$$

$$T_{r\theta in} = -\mu_i [6A_i r] \sin(\theta)$$

$$T_{r\theta net}^h = -6 \sin(\theta) [\mu_o D_o r^{-4} - \mu_i A_i r]$$

$$BC_3 : [T_{r\theta}^h] = 0.0 \rightarrow \mu_o D_o b^{-4} - \mu_i A_i b = 0.0$$

$$\mu_o \left(\frac{u_{fall}}{4b} - A_i b \right) = \mu_i A_i b \Rightarrow \mu_o \frac{u_{fall}}{4b} = A_i b (\mu_i + \mu_o)$$

(131)

$$A_i = \frac{u_{fall}}{4b^2 (m+1)}$$

$$\begin{aligned}
B_i &= -A_i b^2 = -\frac{u_{fall}}{4(m+1)} \\
D_o &= \frac{u_{fall} b^3}{4} - A_i b^5 = \frac{u_{fall} b^3}{4} \frac{\bar{m}}{(m+1)} \\
C_o &= -B_o b - D_o b^{-2} = \frac{-u_{fall} b}{2} - \left[\frac{u_{fall} b}{4} - \frac{u_{fall} b}{4(m+1)} \right] \dots \\
&\frac{u_{fall} b}{4} \left(-3 + \frac{1}{(m+1)} \right) = \frac{-3u_{fall} b}{4} \frac{\frac{2}{3} + \bar{m}}{(m+1)}
\end{aligned} \tag{132}$$

Therefore, internal and external flow functions are obtained for falling drops without affecting EHD, and the sum of these functions with electrohydrostatic steam functions results in the general formula of the flow function. Therefore, the second stream function is related to the case that we have falling but not an electric field and the drop falls. And the first one is for a state that we have just an electric field.

$$\begin{aligned}
\psi_i &= (A_i r^4 + B_i r^2) \sin^2(\theta) = (A_i r^4 - A_i b^2 r^2) \sin^2(\theta) \\
&= A_i b^4 \left(\frac{r^4}{b^4} - \frac{r^2}{b^2} \right) \sin^2(\theta)
\end{aligned} \tag{133}$$

$$\psi_i^{II} = \frac{u_{fall} b^2}{4(m+1)} \left[\frac{r^4}{b^4} - \frac{r^2}{b^2} \right] \sin^2(\theta)$$

$$\psi_o^{II} = (B_o r^2 + c_o r + D_o r^{-1}) \sin^2(\theta)$$

$$\psi_o^{II} = \left[\frac{u_{fall}}{2} r^2 - \frac{3u_{fall} b}{4} \frac{\frac{2}{3} + \bar{m}}{(m+1)} r + \frac{u_{fall} b^3}{4} \frac{\bar{m}}{(m+1)} r^{-1} \right] \sin^2(\theta) \tag{134}$$

$$\psi_o^{II} = u_{fall} b^2 \left[\frac{1}{2} \left(\frac{r}{b} \right)^2 - \frac{3}{4} \frac{\frac{2}{3} + \bar{m}}{(m+1)} \left(\frac{r}{b} \right) + \frac{1}{4} \frac{\bar{m}}{(m+1)} \left(\frac{b}{r} \right) \right] \sin^2(\theta)$$

$$\begin{aligned}
\psi_i &= \psi_i^I + \psi_i^{II}, \quad \psi_o = \psi_o^I + \psi_o^{II} \\
\psi_i &= u_{\theta_{\max}} b^2 \left[\left(\frac{r}{b}\right)^3 - \left(\frac{r}{b}\right)^5 \right] \sin^2(\theta) \cos(\theta) + \frac{u_{fall} b^2}{4(m+1)} \left[\frac{r^4}{b^4} - \frac{r^2}{b^2} \right] \sin^2(\theta) \\
\psi_o &= u_{\theta_{\max}} b^2 \left[\left(\frac{b}{r}\right)^2 - 1 \right] \sin^2(\theta) \cos(\theta) + \dots \\
& u_{fall} b^2 \left[\frac{1}{2} \left(\frac{r}{b}\right)^2 - \frac{3}{4} \frac{\frac{2}{3} + \bar{m}}{(m+1)} \left(\frac{r}{b}\right) + \frac{1}{4} \frac{\bar{m}}{(m+1)} \left(\frac{b}{r}\right) \right] \sin^2(\theta)
\end{aligned} \tag{135}$$

We continue calculations based on the AC current and considering its steady state, but before that, a summary of the relationships is presented in Table 3.

Table 3. Analytical relationships obtained up to this section	
EHD	Falling
$u_{ni} = (Cr + Dr^3)(3\cos^2(\theta) - 1)$	$u_{ni} = (A_i r^2 + B_i) 2\cos(\theta)$
$u_{\theta i} = \frac{-\sin(2\theta)}{2} (3Cr + 5Dr^3)$	$u_{\theta i} = -(4A_i r^2 + 2B_i) \sin(\theta)$
$u_{no} = (Ar^{-4} + Br^{-2})(3\cos^2(\theta) - 1)$	$u_{no} = (B_o + C_o r^{-1} + D_o r^{-3}) 2\cos(\theta)$
$u_{\theta o} = \sin(2\theta) Ar^{-4}$	$u_{\theta o} = -(2B_o + C_o r^{-1} - D_o r^{-3}) \sin(\theta)$

$A = u_{\theta_{\max}} b^4,$ $B = -u_{\theta_{\max}} b^2$ $C = u_{\theta_{\max}} b^{-1},$ $D = -u_{\theta_{\max}} b^{-3}$	$B_o = \frac{u_{fall}}{2}, B_i = -A_i b^2, D_o b^{-4} = \frac{u_{fall}}{4b} - A_i b$ $D_o b^{-4} = \frac{u_{fall}}{4b} - A_i b$ $C_o = \frac{b}{2} (2A_i b^2 - 3B_o)$
$u_{\theta_{\max steady}} = A_s b^{-4} = \frac{9\varepsilon_0 k_2 E_\infty^2}{20\mu_o (1+m)} \frac{(Rq-1)Rb}{(2R+1)^2 + a^2 w^2 (q+2)^2}, A_i = \frac{u_{fall}}{4b^2 (m+1)}$	

With the above relations, we now look at the normal hydrodynamic stress on the interface σ_{rr}^h . To do this, we first specify the normal hydrodynamic stresses for the inside and outside of the droplet as well as the pressure gradient on the interface.

$$T_{rr}^h = 2\mu \frac{\partial u_r}{\partial r} \begin{cases} \text{outside} : (-C_o r^{-2} - 3D_o r^{-4}) \cdot 2 \cos(\theta) \\ \text{inside} : (2A_i r) \cdot 2 \cos(\theta) \end{cases}$$

$$T_{rr}^h \begin{cases} -4(C_o r^{-2} + 3D_o r^{-4}) \cdot \mu_o \cos(\theta) \\ 8\mu_i A_i r \cos(\theta) \end{cases} \quad (136)$$

$$T_{rr}^h \Big|_{net} = -4 \cos(\theta) \left[(C_o r^{-2} + 3D_o r^{-4}) \cdot \mu_o + 2\mu_i A_i r \right]$$

The hydraulic stress is:

$$C_o b^{-2} = \frac{-3u_{fall}}{4b} \frac{\frac{2}{3} + \bar{m}}{(m+1)}, 3D_o b^{-4} = \frac{3u_{fall}}{4b} \frac{\bar{m}}{(m+1)}, A_i b = \frac{u_{fall}}{4b(m+1)} \quad (137)$$

$$T_{rr}^h \Big|_{net} = \frac{2u_{fall} \mu_o}{b} \frac{(-\bar{m} + 1)}{(m+1)} \cos(\theta)$$

Introducing the dimensionless number w, the ratio of the maximum effect of the electric field velocity due to the electric field and the steady-state velocity which results in the falling drop and the form of the flow function is expressed as

$$\begin{aligned}
W &= \frac{u_{\theta\max} 4(\bar{m} + 1)}{u_{fall}} \\
\psi_i &= W \left[\left(\frac{r}{b}\right)^3 - \left(\frac{r}{b}\right)^5 \right] \sin^2(\theta) \cos(\theta) + \left[\frac{r^4}{b^4} - \frac{r^2}{b^2} \right] \sin^2(\theta) \\
\psi_o &= W \left[\left(\frac{b}{r}\right)^2 - 1 \right] \sin^2(\theta) \cos(\theta) \\
&+ \left[\frac{1}{2} \left(\frac{r}{b}\right)^2 - \frac{3}{4} \frac{\frac{2}{3} + \bar{m}}{(\bar{m} + 1)} \left(\frac{r}{b}\right) + \frac{1}{4} \frac{\bar{m}}{(\bar{m} + 1)} \left(\frac{b}{r}\right) \right] \sin^2(\theta)
\end{aligned} \tag{138}$$

Calculating the pressure on the interface for inside the drop:

$$\begin{aligned}
u_{ri} &= (A_i r^2 + B_i) 2 \cos(\theta) \\
r^2(\cdot) &= (A_i r^4 + B_i r^2) 2 \cos(\theta) \\
\frac{\partial}{\partial r}(\cdot) &= (4A_i r^3 + 2B_i r) 2 \cos(\theta) \\
\frac{1}{r^2}(\cdot) &= (4A_i r + 2B_i r^{-1}) 2 \cos(\theta) \\
\frac{\partial}{\partial r}(\cdot) &= (4A_i - 2B_i r^{-2}) 2 \cos(\theta) \\
\frac{\partial u_r}{\partial \theta} &= -(A_i r^2 + B_i) 2 \sin(\theta) \\
\sin(\theta)(\cdot) &= -(A_i r^2 + B_i) 2 \sin^2(\theta) \\
\frac{\partial}{\partial \theta}(\cdot) &= -4(A_i r^2 + B_i) \sin(\theta) \cos(\theta) \\
\frac{1}{r^2 \sin(\theta)}(\cdot) &= -4(A_i + B_i r^{-2}) \cos(\theta) \\
u_\theta \sin(\theta) &= -(4A_i r^2 + 2B_i) \sin^2(\theta) \\
\frac{\partial}{\partial \theta}(\cdot) &= -2(4A_i r^2 + 2B_i) \sin(\theta) \cos(\theta) \\
\frac{-2}{r^2 \sin(\theta)}(\cdot) &= 4(4A_i + 2B_i r^{-2}) \cos(\theta) \\
(20A_i) \cos(\theta) &= \mu_i \cdot \frac{\partial P_i}{\partial r} \Rightarrow p_i(r, \theta) = \mu_i (20A_i r) \cos(\theta) + \Pi_i
\end{aligned} \tag{139}$$

Calculating the pressure on the interface for outside the drop:

$$\begin{aligned}
u_{ro} &= (Bo + C_o r^{-1} + D_o r^{-3})2 \cos(\theta) \\
r^2(\cdot) &= (Bor^2 + C_o r^1 + D_o r^{-1})2 \cos(\theta) \\
\frac{\partial}{\partial r}(\cdot) &= (2Bor + C_o - D_o r^{-2})2 \cos(\theta) \\
\frac{1}{r^2}(\cdot) &= (2Bor^{-1} + C_o r^{-2} - D_o r^{-4})2 \cos(\theta) \\
\frac{\partial}{\partial r}(\cdot) &= (-2Bor^{-2} - 2C_o r^{-3} + 4D_o r^{-5})2 \cos(\theta) \\
\frac{\partial u_r}{\partial \theta} &= -(Bo + C_o r^{-1} + D_o r^{-3})2 \sin(\theta) \\
\sin(\theta)(\cdot) &= -(Bo + C_o r^{-1} + D_o r^{-3})2 \sin^2(\theta) \\
\frac{\partial}{\partial \theta}(\cdot) &= -4(Bo + C_o r^{-1} + D_o r^{-3}) \sin(\theta) \cos(\theta) \\
\frac{1}{r^2 \sin(\theta)}(\cdot) &= -4(Bor^{-2} + C_o r^{-3} + D_o r^{-5}) \cos(\theta) \\
u_\theta \sin(\theta) &= -(2B_o + C_o r^{-1} - D_o r^{-3}) \sin^2(\theta) \\
\frac{\partial}{\partial \theta}(\cdot) &= -2(2B_o + C_o r^{-1} - D_o r^{-3}) \sin(\theta) \cos(\theta) \\
\frac{-2}{r^2 \sin(\theta)}(\cdot) &= 4(2B_o r^{-2} + C_o r^{-3} - D_o r^{-5}) \cos(\theta) \\
(-4C_o r^{-3}) \cos(\theta) &= \mu_o \cdot \frac{\partial P_o}{\partial r} \Rightarrow p_o(r, \theta) = 2\mu_o (C_o r^{-2}) \cos(\theta) + \Pi_o
\end{aligned} \tag{140}$$

Calculating the pressure difference on the interface:

$$\begin{aligned}
-(p_o - p_i) &= p_i - p_o = \cos(\theta) \left[\mu_i (20A_i b) - 2\mu_o (C_o b^{-2}) \right] + \Pi_i - \Pi_o \\
p_i - p_o &= \frac{5u_{fall} \mu_i}{b(1+m)} - \frac{\mu_o \left[\frac{u_{fall}}{2(1+m)} - \frac{3}{2} u_{fall} \right]}{b} \\
p_i - p_o &= \frac{u_{fall}}{4b(1+m)} [26\mu_i + 4\mu_o] \cos(\theta) + \Pi_i - \Pi_o
\end{aligned} \tag{141}$$

Calculating the resultant hydrodynamics on the interface:

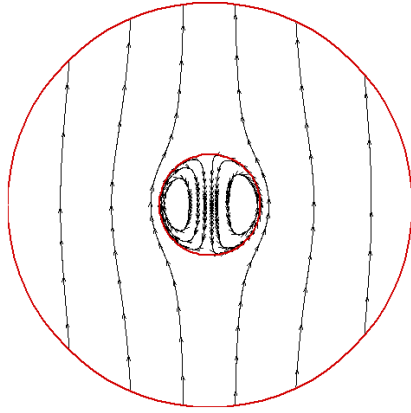
$$\begin{aligned}
\sigma_{rr}^h &= T_{rr}^h - (p_o - p_i) = \\
&= \frac{2u_{fall}\mu_o}{b} \frac{(-m+1)}{(m+1)} \cos(\theta) + \frac{u_{fall}}{4b(1+m)} [26\mu_i + 4\mu_o] \cos(\theta) + \Pi_i - \Pi_o \\
\sigma_{rr}^h)_{net}^{II} &= \frac{u_{fall}}{b(1+m)} \left[2\mu_o - 2\mu_i + \frac{26}{4}\mu_i + \mu_o \right] \cos(\theta) + \Pi_i - \Pi_o \\
\sigma_{rr}^h)_{net}^{II} &= \frac{u_{fall}}{b(1+m)} \left[3\mu_o + \frac{9}{2}\mu_i \right] \cos(\theta) + \Pi_i - \Pi_o
\end{aligned} \tag{142}$$

To obtain a droplet shape, we use the balance of normal stresses by the force of the capillary. So that:

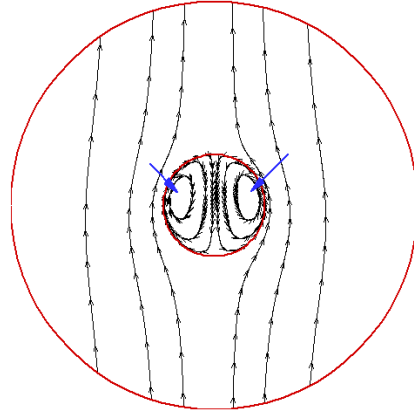
$$\begin{aligned}
T_{rr}^e + \sigma_{rr}^h &= \gamma k \\
I: \sigma_{rr}^h)_{net} &= -u_{\theta max} b^{-1} (3 \cos^2(\theta) - 1) [3\mu_i + 2\mu_o] + \Pi_i - \Pi_o \\
II: \sigma_{rr}^h)_{net}^{II} &= \frac{u_{fall}}{b(1+m)} \left[3\mu_o + \frac{9}{2}\mu_i \right] \cos(\theta) + \Pi_i - \Pi_o \\
\frac{9\varepsilon_0 k_2 E_\infty^2}{4} \Phi_\nu \cos^2(\theta) + \beta \cos(\theta) + \Pi_i - \Pi_o &= \gamma K \\
\beta &= \frac{u_{fall}}{b(1+m)} \left[3\mu_o + \frac{9}{2}\mu_i \right]
\end{aligned} \tag{143}$$

If it is not Falling, then B = 0 and consequently a3 = 0, and all the coefficients inside the series are zero and the iteration is not repeated. Of course, when B is not zero, we have a cut-off cutoff error, and all the coefficients inside the series are dependent on B.

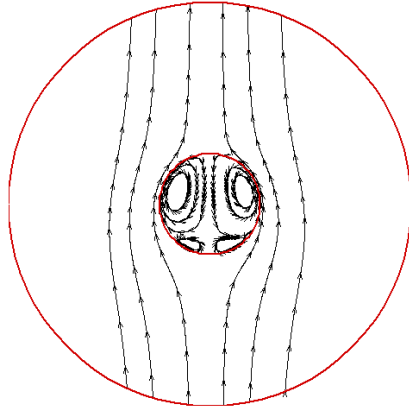
$$\begin{aligned}
r &= b [1 + f(x)], f(x) = \sum_{n=0}^{\infty} a_n x^n \\
-6a_3 \frac{\gamma}{R} &= \beta \Rightarrow a_3 = \frac{-R\beta}{6\gamma} \\
4a_2 \frac{\gamma}{R} &= \frac{9\varepsilon_0 k_2 E_\infty^2}{4} \Phi_\nu \Rightarrow a_2 = \frac{9}{16} \frac{\varepsilon_0 k_2 E_\infty^2 \Phi_\nu R}{\gamma} = \frac{9}{16} C a_e \cdot \Phi_\nu \\
a_0 &= \frac{-a_2}{3}
\end{aligned} \tag{144}$$



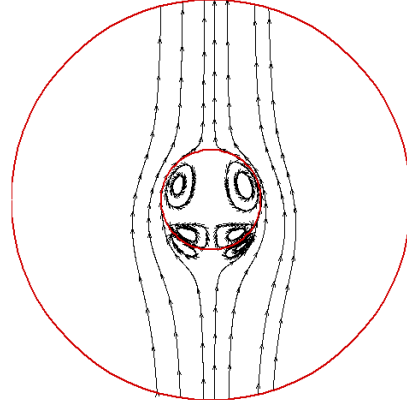
$W=0.0$



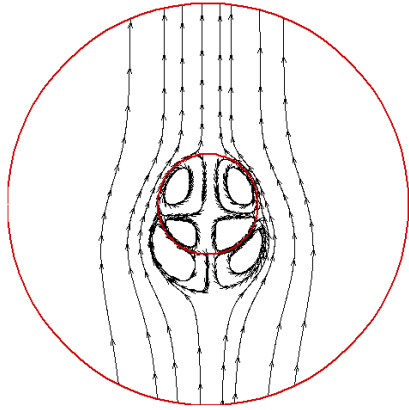
$W=1.0$



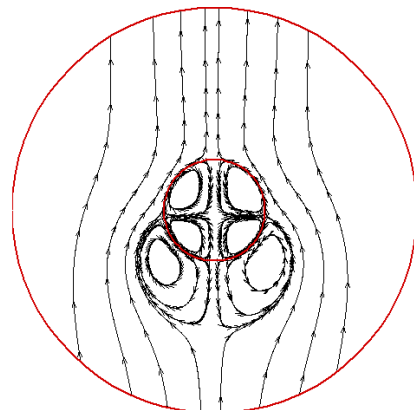
$W=1.5$



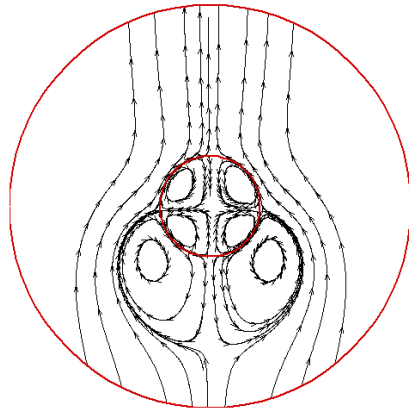
$W=2.0$



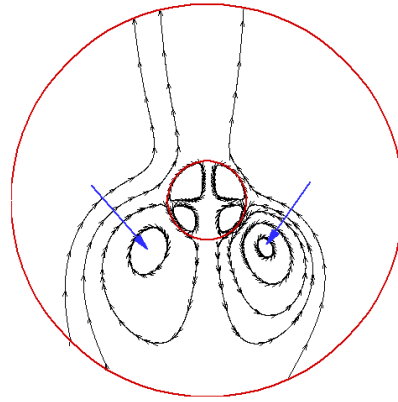
$W=4.0$



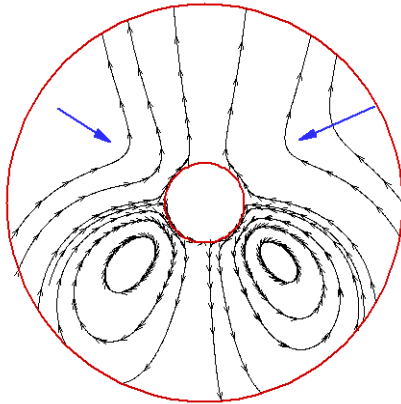
$W=8.0$



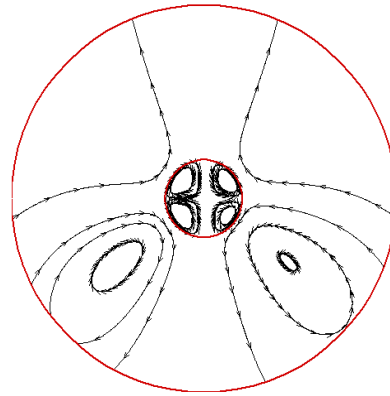
W=12



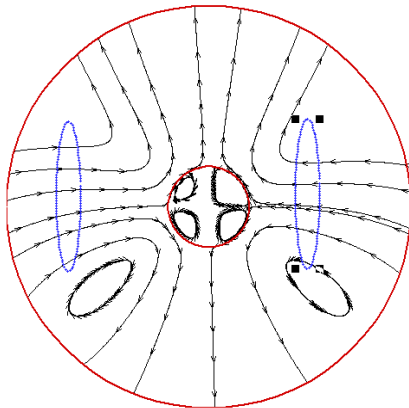
W=30



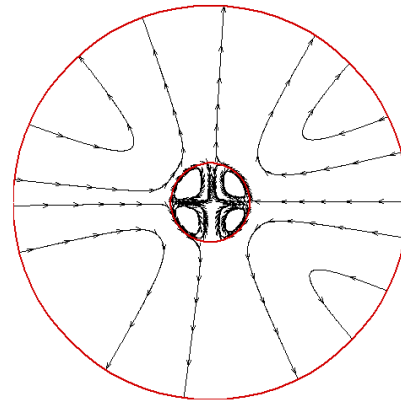
W=70



W=150



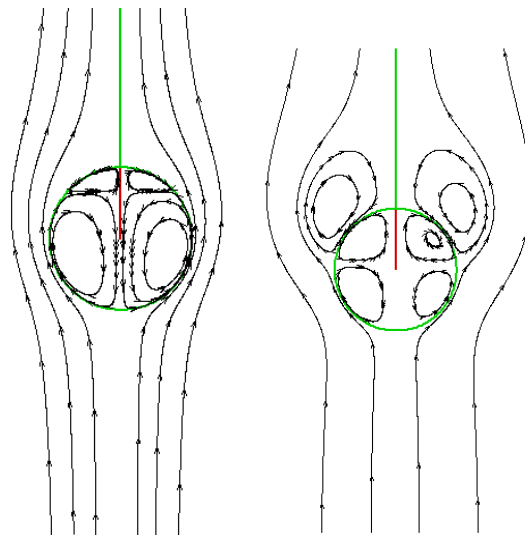
W=300



W=∞

Figure 23. How to move the fluid around and inside the droplet for system 2 based on the increase of the dimensionless number W .

As stated, W is a non-zero number that represents the importance of the ratio of the electric field to the motion of the droplet. Figure 23 and Figure 24 show this dependence. In very high W numbers, the electric field is dominant and in low numbers the effect of the electric field is negligible. The positive value of this number means the movement of the fluid from the poles to the corners and for the negative values is reversed. For $W > 10$, the shape of the vortices within the drop is not much different from the state of the electric field. In Figure 23, two vortices are initially formed within the droplet. As w increases, the vortex center moves from the center of the droplet and shifts to the higher. Because $Rq < 1$, the electric current seeks to move the fluid from the corners toward the pole. So in the upper hemisphere, the droplet behaves like a falling drop, while in the lower hemisphere EHD seeks to move fluid from $\theta = \pi/2, 3\pi/2$ to $\theta = \pi$. The fall of the droplet causes the fluid to flow from the bottom up and these two behave in the opposite of each other. And this is a factor for creating a negative gradient at the bottom of the drop and thus forming a vortex. With increasing w or the electric field, the power of the current flowing from the EHD has increased and the center of the vectors is shifted to the outside. Ultimately, the electric field is overcome, and the vortices are converted to open vortex. Figure 24 is for $Rq > 1$. The results are exactly the same as the previous one.



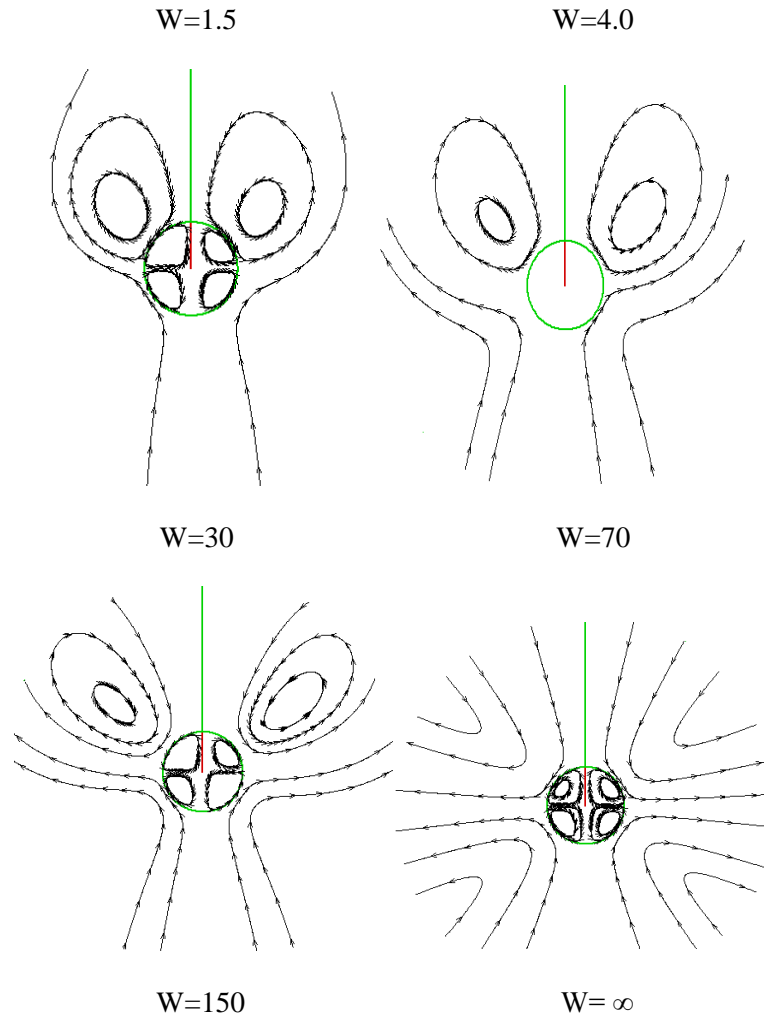


Figure 24. Movement of fluid around and within the droplet for system 3 based on the increase of the dimensionless number W .

Figure 25 shows the shape of the deformed droplet in three cases. The figure on left shows the pure electric field effect, the figure on the right shows the pure falling effect and the figure in the middle shows both effects. Figure 26 shows that the form obtained from the analytical solution corresponds to numerical results. Figure 27 shows the comparison of the number of polynomials considered in the power series to solve the curvature equation, and therefore, 80 sentences seem to be sufficient to examine the shape of the droplet.

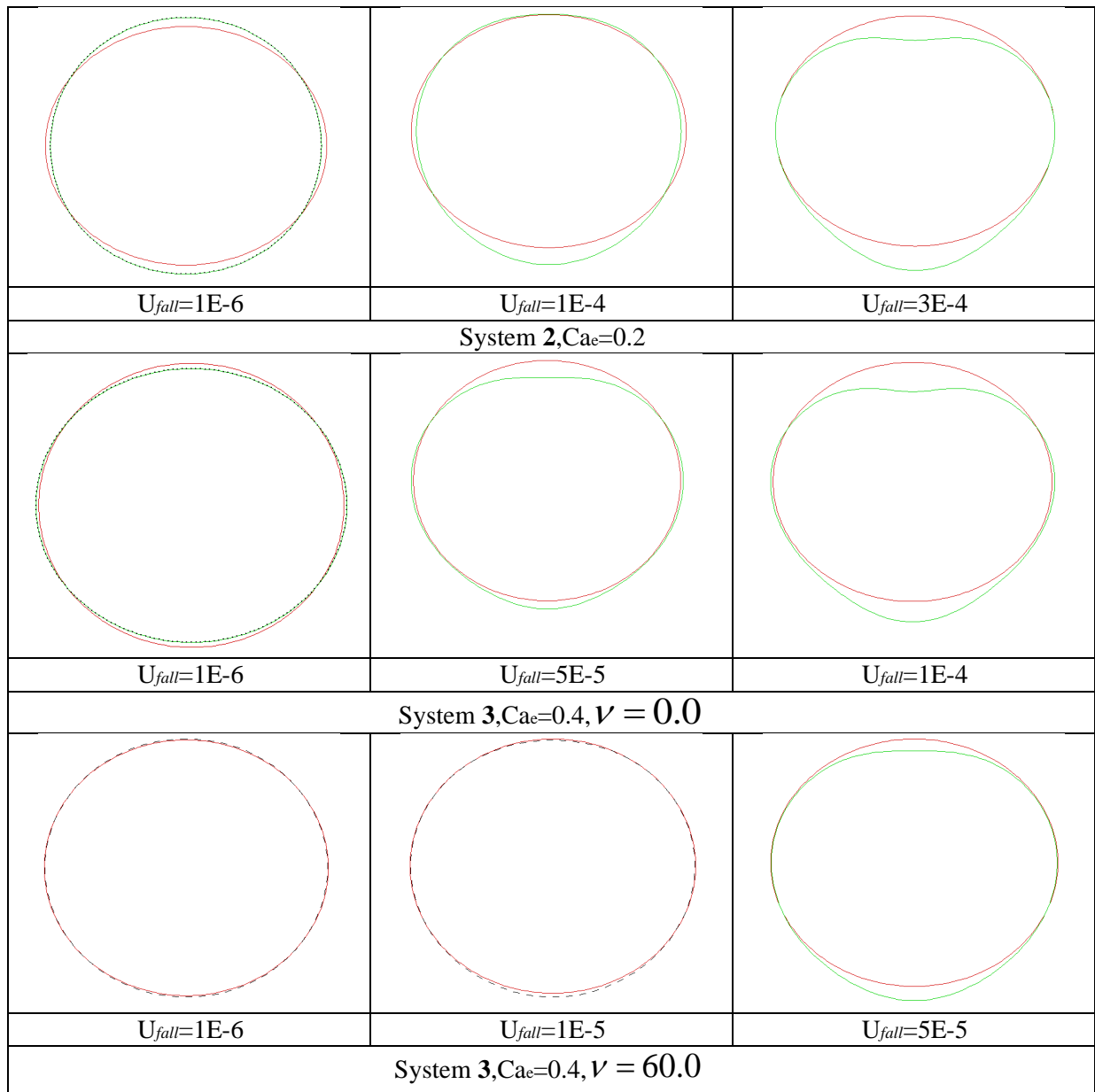
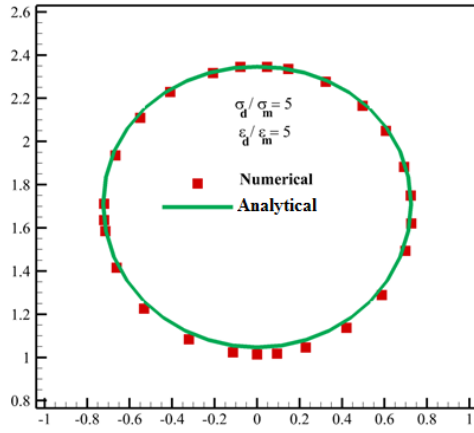
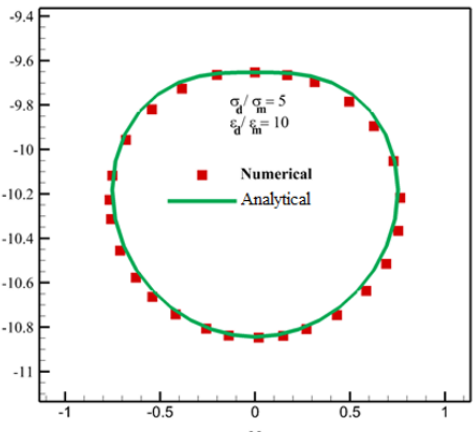


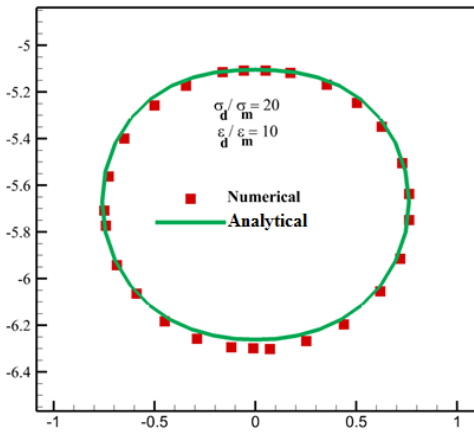
Figure 25. Drop deformation in the two systems, effects of EHD and falling.



C=5 and Q=5



C=5 and Q=10



C=20 and Q=10

Figure 26. Comparison of the analytical solution calculated in this study against the current direct numerical solution using Gerris.

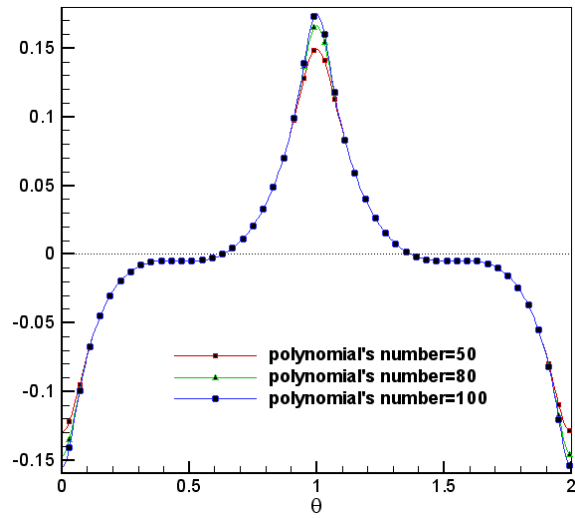


Figure 27. The number of necessary series terms to reach the converted solution for the deformation function

5 Chapter 5: Coalescence of Two Falling Drops

As presented in Figure 28, the coalescence of two falling drops has been studied numerically to investigate the effects of the electric field on their interactions compared to those of without the electric field effects.

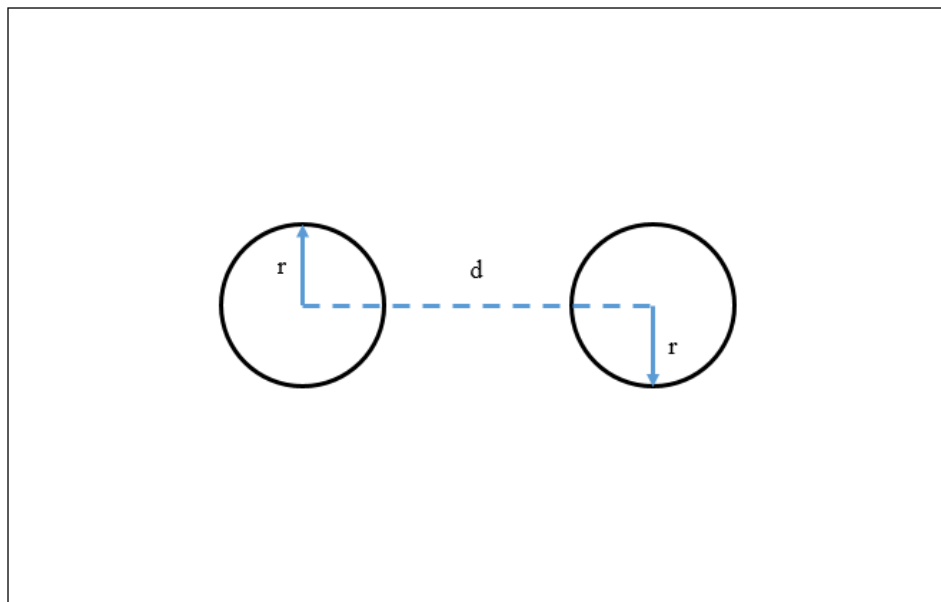


Figure 28. The geometry for two drops.

5.1 Coalescence of two falling without electric field effects

In the first case, the coalescence of two falling drops has been studied without considering the electrical field effects. The two falling drops descend without having any effects on each other as they are not influenced by an external electric field. As can be seen in Figure 29 the two drops falling down up to the end of the domain with no influence on each other's behavior

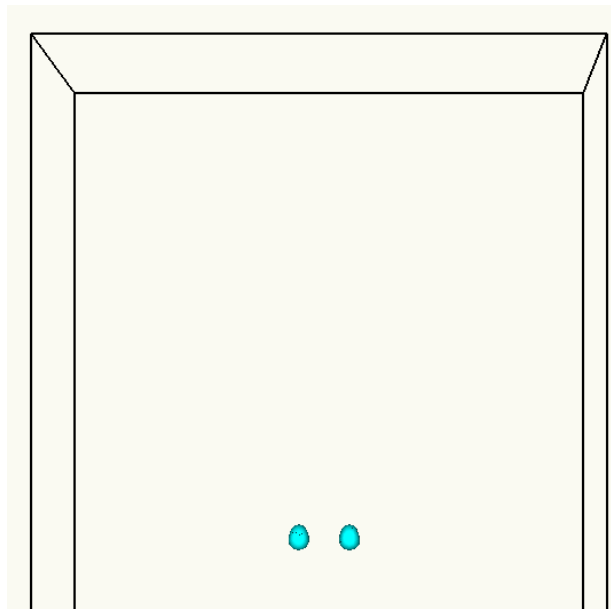


Figure 29. The coalescence of two falling drops without the electrical field effects.

5.2 Coalescence of two falling drops under electric field effects

5.2.1 Distance effects

The coalescence of two falling drops has been influenced by external electrical field effects. The drops fall at different distances from each other. As shown in Figure 30 the drops at the shorter distances from each other have more effect on each other and coalescence is a shorter time as here the results are shown at $t=2$.

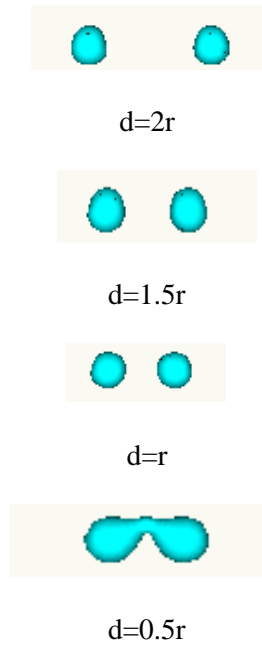
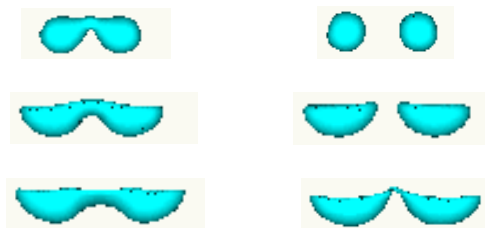


Figure 30. The coalescence of two falling drops under electric fields at different distances from each other at $Ca_E = 0.4$ and $t=2$.

Figure 31 shows the coalescence of two falling drops under electric fields at different distances and different time sequences. As seen the two drops located closer to each other initially coalesces stronger under electric field compared to those at the further distance at the beginning.



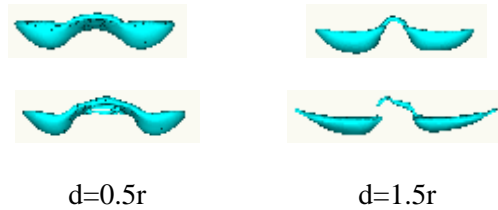


Figure 31. The coalescence of two falling drops under electric fields at different distances from each other at $Ca_E = 0.4$ and $t=2$ to $t=6$.

5.2.2 Electric field strength effects

Figure 32 depicts the coalescence of two falling drops under electric fields at different distances from each other at various electric fields at two electric fields. As the results show, by increasing the electric field the two drops influence on each other so strongly so that at $t=3$ upward they start merging each other which shows the much stronger coalesce of the drops under stronger electric field although they were located at the same distance apart from each other initially.

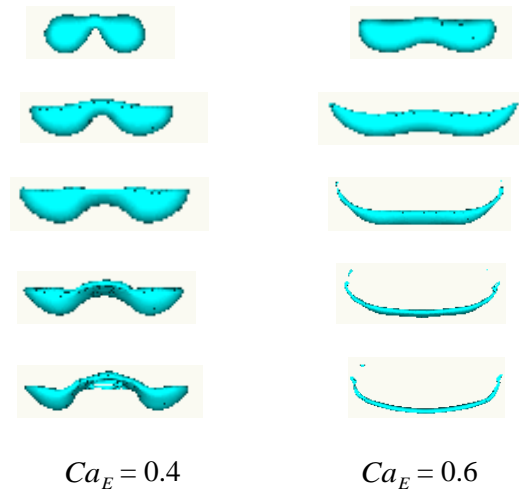


Figure 32. The coalescence of two falling drops under electric fields at different distances from each other at different electric fields, $d=0.5r$ and $t=2$ to $t=6$.

Figure 33 displays the coalescence of two falling drops under different electric fields which are initially separated from each at $d=r$ at $t=4$. As seen from the results as the strength of the electric

field grows, the two drops coalesce much stronger up to the point they get completely merged into each other.

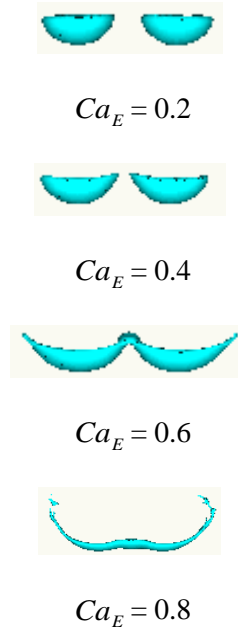


Figure 33. The coalescence of two falling drops under different electric fields at $d=r$ and $t=4$.

5.3 Near Wall Deformation of Falling Droplets under the Effect of Electric Field

Figure 34 shows the computational domain used in the current work along with the boundary conditions. The dimensions of the domain and drop are shown in the figure. The width of the computational domain is $40R$ with the height of $160R$. A spherical droplet with density and viscosity of ρ_1 , μ_1 and radius R falls under the action of gravity g . The initial velocity of the drop is zero. The surrounding medium has a viscosity of μ_2 and density of ρ_2 . The subscript 1 refers to

drop and 2 is for the outside medium. Wall boundary conditions are on left and right sides of the domain and symmetry boundary conditions are applied on the rest of the boundaries.

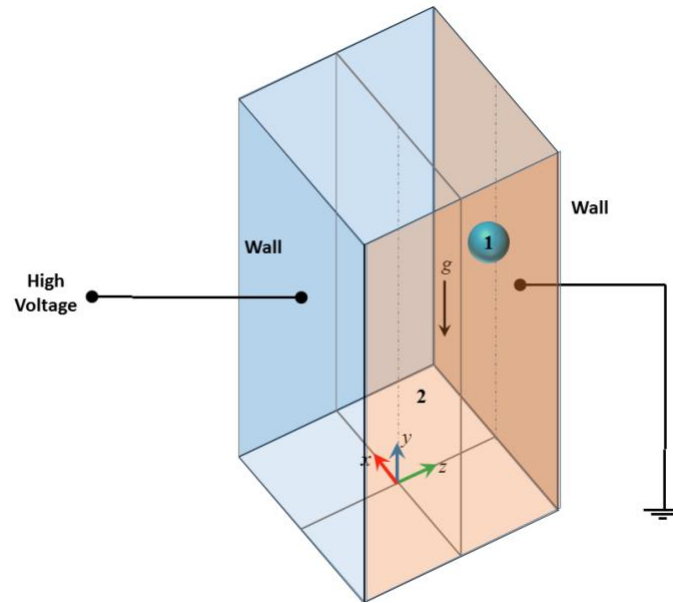


Figure 34. The schematic of the problem and the boundary conditions.

Figure 35 depicts the wall effect on the falling droplet for $Ga = 40$, $Bo = 5$, $\rho_r = 2$, $\mu_r = 10$. Figure 35a shows that the drop feels the repulsive force from the wall due to the wall shear and as a result, the right side of the drop pushed upward. The drop is compressed horizontally (along larger diameter) deforms toward oblate shape compared to the ellipsoidal form that drop has under symmetrical boundary condition. As seen the wall boundary condition slows down the process of drop deformation toward the bowl-like shape which is the beginning of the drop breakup. Figure 35b shows the results of the falling drop deformation with wall boundary conditions under the electric field. As seen under EHD force the falling drop takes the oblate shape which is tilted because of wall shear. Wall repulsive force on drop push the right side of the drop upward which

will be combined by the EHD force compressed drop more and deform it toward initial spherical shape which noticeably delays the transformation of the drop to bowl-like shape and after drop breakup.

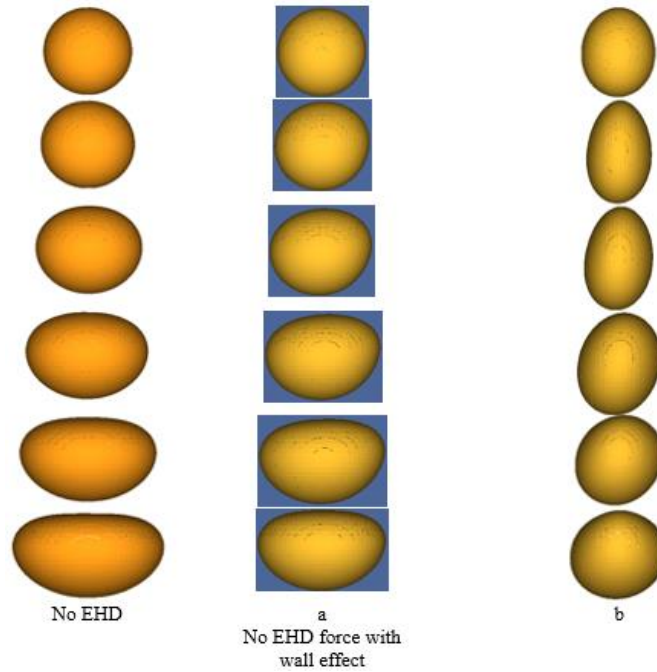


Figure 35. The Effects of EHD on drop for, $Ga = 40$, $Bo = 5$, $Ca_E = 0.11$, $\rho_r = 2$, $\mu_r = 10$ for (a) wall boundary condition applied and (b) $Q=25$, $C= 5$ from $t=1$ to $t=6$.

Figure 36 shows the wall effect on the falling droplet for $Ga = 40$, $Bo = 5$, $\rho_r = 5$, $\mu_r = 10$. Again similarly, the drop is compressed horizontally and its right side pushed upward under the shear wall which takes an oblate form and after this behavior slows down and becomes volatile as at $t=5$ and 6 the right side tilts downward. Figure 36b shows the drop influenced by the electric field and as seen the drop takes the oblate form and also becomes tilted due to the wall effects improving the oblate form and after $t=4$ the deformation changes and the drop side faces the wall pulls downward.

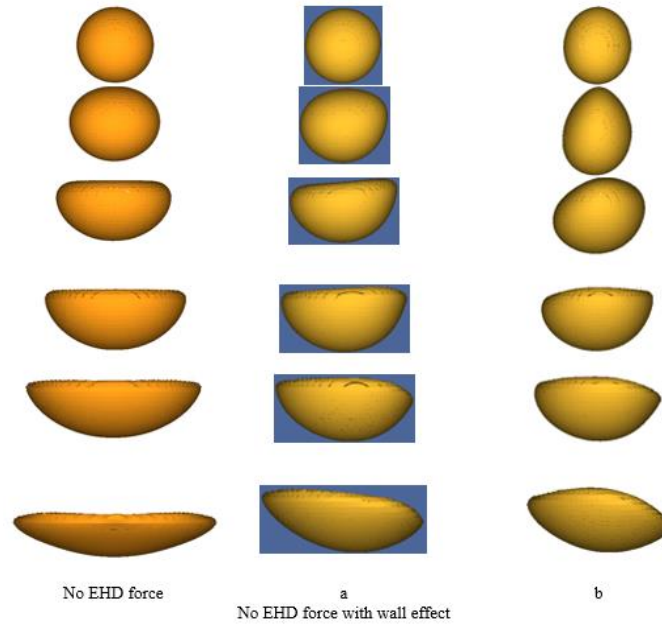


Figure 36. The effects of EHD on drop for, $Ga = 40$, $Bo = 5$, $Ca_E = 0.11$, $\rho_r = 5$, $\mu_r = 10$ for (a) for (a) wall boundary condition applied and (b) $Q=25$, $C= 5$ from $t=1$ to $t=6$.

Figure 37 shows the results for the falling drop under wall effect (Figure 37b) and electric field for $Q=25$, $k=5$ (Figure 37c). In Figure 37b, at $t=5$ the drop slightly tilted by the repulsive force from the wall boundary. At $t=6$, the drop's side faced to the wall pushed away from the wall as the symmetry shape of the drop under symmetry boundary condition distorted. Because of the wall effect the core of the drop becomes less perforated which delays the breaking up process. At $t=7$ and 8 also the drop feels the wall repulsive force due to the wall shear as the side faced the wall is pushed away toward the symmetrical shape the drop structure at those times deflected. Under wall effect, the higher portion of the drop core is left less perforated with thicker and stronger ligament which again slows down the process of the further drop breakup toward small fragmentation and then small droplets. Figure 37c shows the breaking up process under wall affects and EHD force. The electric field combined with wall shear effect the drop becomes distorted with the higher rate as the multiple holes grow rapidly forming a network of attached ligaments which thereafter into

many droplets. Also, the drop structure pushed stronger away from the wall and the ligaments and bridges form closer to the wall transform into smaller droplet faster as the regions near the wall more drops and weaker ligaments form.

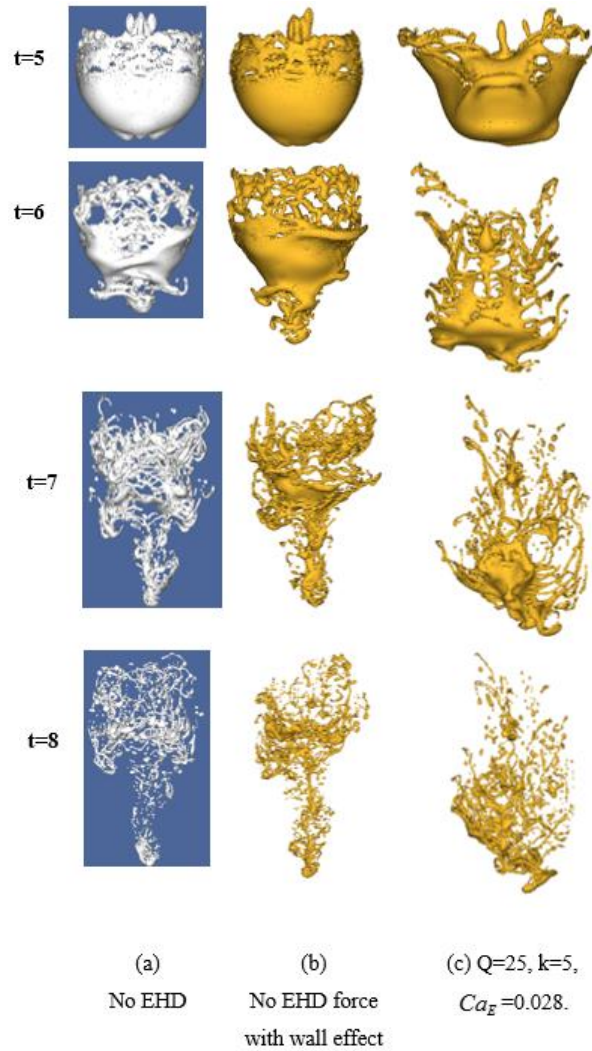


Figure 37. Deformation of the falling drop under (a) wall effect and no EHD force (b) EHD force.

6 Chapter 6: Conclusion and recommendations

6.1 Conclusion

In this dissertation, a three-dimensional study of the deformation of a single falling droplet surrounded by another liquid under the effect of the electric field has been studied analytically and numerically. In addition, the effects of EHD on the coalescence of two falling drops have been investigated and their interactions under influence of EHD force have been studied numerically. An open-source volume-of-fluid solver, Gerris has been used for numerical modeling using direct numerical simulation (DNS). The analytical solutions have been compared for various values of electrical conductivity and permittivity against DNS results. The comparison of the analytical solutions and the numerical results show a great agreement between them. The analytical modeling of drop deformation has been presented in detail and also the DNS results are compared for both electric and fluid fields against analytical and previously published experimental data [38].

Extensive numerical studies have been performed in order to come up with a powerful numerical method that not only can capture the complicated physical nature of the two-phase-flow falling drop deformation but also to be computationally cost-effective. To avoid issues of turbulence modeling, DNS has been used for simulation of this complicated problem as it solves the whole computational domain directly without any simplification for accurate results. Using Gerris provides a significant tool in investigating the EHD-multiphase problems as it uses the adaptive mesh and a smaller number of grids for capturing the drop's deformation perfectly and is tremendously cost-effective in terms of computational cost.

Contrary to most of the previously published work that studied the drop deformation surrounded in a medium with a similar density, the gravitational force has been implemented to the Gerris code in this study; the drop deformation has also been studied under the gravitational effect to represent

the real-life problems. As the results showed, under the effect of gravity, the drop undergoes various deformations before it goes to fragmentation. These deformations can be managed by using the external electric force in order to speed up or slow down its behavior.

The analytical solution has been developed for modeling the small deformation of the falling drop under the effect of the electric field. This analytical method provides an easy, fast, accurate and cost-effective solution in analyzing the drop behavior for small deformation. The developed analytical method produced a user-friendly solution for prediction of the drop deformation rather than performing a complex, high-cost and time consuming experimental study. In addition, the analytical solution can be used for investigating the deformation for various physical parameters much easier and quicker compared to the limited cases of experimental work that makes the investigation much more difficult as each change in physical parameters needs a new set-up for measuring the data.

The wall effect is also studied in order to investigate its influence on the falling drop behavior. The results have been presented for the drop deformation under the wall effect with and without combination with the external electric field. Results revealed that the shear wall effects impose a force on drop behavior which causes the drop to form the oblate and prolate shapes, which results in speeding up and slowing down its bowl-shape formation. This shear force can be reinforced by its combination with the electric force which significantly affects the drop deformation in expediting and delaying its deformation toward final fragmentation.

The coalescence and interaction of the two drops under gravity and electric force have been studied numerically. As the results showed, without an EHD force the two falling drops have no interaction with each other as they descend toward the bottom of the computational domain in spite of their deformations. The application of the EHD force showed that the two falling drops start interacting with each other which leads to their coalescence. The interaction and coalescence are affected significantly by the strength of the electric field. Within the investigated parameter range, it was

found, as the strength of the electric field grows, the two drops' coalescence becomes much stronger up to the point that they get completely merged into each other. In addition, the effects of the distance on their coalescence and interaction have been presented using the numerical solution; the two drops which are initially at a farther distance from each other have a weaker effect on each other compared to those that are in a closer distance from each other and this interaction can be improved by using the electric force.

The results showed that electric force can be a significant external force in controlling the drop deformation and fragmentation. The numerical results revealed that the electric field can expedite or delay the bowl-like shape formation of the drop which is the initial stage of the drop to go to the bag formation stage and eventually to its fragmentation.

A main focus of the work was on the contribution of an electric field, which induces a deformation, to the behavior of a falling drop since falling/rising of a drop itself can deform the drop. It was found that the latter is dependent on the hydrodynamic properties of both continuous and dispersed phases while the former is hinged to the electrical properties of these distinct phases. The results reveal that depending on the direction of the imposed electric field, deformation can be halted or promoted with respect to the different flow regimes. While a drop can turn into a cup shape due to falling, the electric field can be strong enough to generate sufficient electrical stresses to revert the drop to its initial shape. Comparing the electrical stresses contours around the interface of the drop as well as viscous stresses, it is found that pressure gradient can be determinative factors in assessing at which conditions electrical behavior is dominant compared to solely hydrodynamic induced deformation. While in a low Reynolds number or a low Weber number analytical results specify the different forces implemented on the interface, a high Weber or Reynold number results specify the Plateau-Rayleigh instability arising at the tips of the drop results in rupturing the drop, resulting in rupturing the drop and generating satellite drops.

It was found that DNS has the potential to resolve the mechanism in a short timescale. It is worth mentioning that circulation inside the droplet, as a result of balancing viscous and electrical stresses, plays a significant role in drop behavior particularly in the turbulent regime; in turbulent flow regime, vortices inside and outside the drop undergo severe time-dependent interaction, which are the phenomena difficult to be captured by the available analytical techniques.

6.2 Recommendations

Following the importance of electric field on deformation, coalescence or rupturing of the droplet, which depends on different parameters, more investigations are needed for practical applications such as emulsions which consist of the population of droplets (rather than a single droplet case) within the continuous phase e.g., water in oil emulsions as follows :

- 1- Check the effect of electricity on the stability of the emulsion.
- 2- Conducting a numerical simulation to see how one/two droplets or multiple drops interact with each other inside the dielectric medium to give an idea of how the droplets (suppose conductive ones-water) behave in the emulsion.
- 3- How much they can be deformed,
- 4- How much they are likely to attract each other because of the dipole-dipole attraction,
- 5- How EHD-induced vortices can change the motion of these droplets and become them closer together and addresses many important issues in terms of the rheology of droplets in an emulsion.
- 6- Improving and extending the analytical solution for a high range of Capillary number

This work definitely improves the idea behind making an emulsion. Effect of the electric field for making an emulsion can be explained as below. Today's research regarding the emulsion synthesis can be divided into parts 1) size of the dispersed droplet (making nano-emulsion by the typical

processes such as homogenizer, microfluid or porous membrane have limitation. In the case of homogenizer, where shear force is used to break the droplet (dispersed phase), it depends on many factors (viscosity of the continuous phase, rotational speed, turbulent energy, or in case of membrane /microfluidic, the limitation in terms of the manufacturing process to make nano-sized channel or pores and so on). The electric field is a promising technique which enables us to break the dispersed phase to satellite droplets (the same was done for electrospinning [49] or even mixing the two viscous oils). If one considers the two oils where one is less dense than the second, we can have two layers of oils. When we apply the electric field on the interface between these two liquids, the instability propagates as a wave which finally leads to mixing one into another. One can replace one of that oil by water phase to make w/o or o/w emulsions. Depending on the applied electric field and properties (hydrodynamic, electrical, and chemical) of those two phases, different types of emulsion can be made. Note that, after breaking the dispersed phases to tiny droplets, these droplets want to coalesce again to reduce the free energy and decreasing the surface area, then stabilizers (surfactant or particles) are used to hold these droplets inside the continuous phase and prevent merging (break up of emulsion-separation). Here how electric field can affect the interface by the presence of a surfactant or in another scenario charged particles is another important thing which has not been investigated yet. Even neutral hydrophobic/hydrophilic particles at the interface of o/w show charges which create Columbic force or dipole-dipole interaction, for which the amount of each force needs to be measured.

References

- [1] G. I. Taylor, "The Shape and Acceleration of a Drop in a High-Speed Air Stream," *Sci. Pap. Sir G.I. Taylor*, pp. 457–467, 1693.
- [2] M. Pilch and C. A. Erdman, "USE OF BREAKUP TIME DATA AND VELOCITY HISTORY DATA TO PREDICT THE MAXIMUM SIZE OF STABLE FRAGMENTS FOR ACCELERATION-INDUCED BREAKUP OF A LIQUID DROP 1 . INTRODUCTION The work presented here was part of an effort originally initiated to address the questio," *Int. J. Multiph. Flow*, vol. 13, no. 6, pp. 741–757, 1987.
- [3] J. O. Hinze, "Fundamentals of the hydrodynamic mechanism of splitting in dispersion processes," *AIChE J.*, vol. 1, no. 3, pp. 289–295, Sep. 1955.
- [4] M. P. Norin, "The atomisation of liquid fuels," *J. Franklin Inst.*, vol. 257, no. 4, p. 339, 2003.
- [5] Faeth G.M., L.-P. H., and P.-K. W., "Structure and breakup properties of sprays," *Int. J. Multiph. Flow*, vol. 21, pp. 99–127, 1995.
- [6] H. J. Herrmann, F. K. Wittel, and F. Kun, "Fragmentation," *Phys. A Stat. Mech. its Appl.*, vol. 371, no. 1, pp. 59–66, Jan. 2006.
- [7] J. R. Melcher and G. I. Taylor, "Electrohydrodynamics: A Review of the Role of Interfacial Shear Stresses," *Annu. Rev. Fluid Mech.*, vol. 1, no. 1, pp. 111–146, Jan. 2003.
- [8] M. Ryan *et al.*, "Experimental Results of an Electrostatic Injector," no. October, 2014.
- [9] W. Lehr and W. Hiller, "Electrostatic atomization of liquid hydrocarbons," *J. Electrostat.*, vol. 30, no. C, pp. 433–440, 1993.
- [10] G. H. Amine-Eddine and J. S. Shrimpton, "On simulations investigating droplet diameter-charge distributions in electrostatically atomized dielectric liquid sprays," *Int. J. Numer. Methods Fluids*, vol. 72, no. 10, pp. 1051–1075, Aug. 2013.
- [11] J. S. Shrimpton, "ATOMIZATION, COMBUSTION, AND CONTROL OF CHARGED HYDROCARBON SPRAYS," *At. Sprays*, vol. 11, no. 4, pp. 365–396, 2014.
- [12] H. Paknemat, A. R. Pishavar, and P. Pournaderi, "Numerical simulation of drop deformations and breakup modes caused by direct current electric fields," *Phys. Fluids*, vol. 24, no. 10, p. 102101, Oct. 2012.
- [13] P. K. Notz and O. A. Basaran, "Dynamics of drop formation in an electric field," *J. Colloid Interface Sci.*, vol. 213, no. 1, pp. 218–237, 1999.
- [14] J. H. Jung, H. OOh, and S. S. Kim, "Numerical simulation of the deposition pattern in multiple.pdf," *Power Technol.*, vol. 198, pp. 439–444, 2010.

- [15] B. P. Van Poppel, O. Desjardins, and J. W. Daily, “A ghost fluid, level set methodology for simulating multiphase electrohydrodynamic flows with application to liquid fuel injection,” *J. Comput. Phys.*, vol. 229, no. 20, pp. 7977–7996, 2010.
- [16] J. M. López-Herrera, S. Popinet, and M. A. Herrada, “A charge-conservative approach for simulating electrohydrodynamic two-phase flows using volume-of-fluid,” *J. Comput. Phys.*, vol. 230, no. 5, pp. 1939–1955, 2011.
- [17] J. C. Baygents, N. J. Rivette, and H. A. Stone, “Electrohydrodynamic deformation and interaction of drop pairs,” *J. Fluid Mech.*, vol. 368, pp. 359–375, Aug. 1998.
- [18] “Studies in electrohydrodynamics. I. The circulation produced in a drop by an electric field,” *Proc. R. Soc. London. Ser. A. Math. Phys. Sci.*, vol. 291, no. 1425, pp. 159–166, Apr. 1966.
- [19] “Particle behaviour in shear and electric fields I. Deformation and burst of fluid drops,” *Proc. R. Soc. London. Ser. A. Math. Phys. Sci.*, vol. 267, no. 1328, pp. 45–61, Apr. 1962.
- [20] S. Torza, R. G. Cox, and S. G. Mason, “Electrohydrodynamic Deformation and Burst of Liquid Drops,” *Philos. Trans. R. Soc. A Math. Phys. Eng. Sci.*, vol. 269, no. 1198, pp. 295–319, Feb. 1971.
- [21] O. O. Ajayi, “A Note on Taylor’s Electrohydrodynamic Theory,” *Proc. R. Soc. A Math. Phys. Eng. Sci.*, vol. 364, no. 1719, pp. 499–507, Dec. 1978.
- [22] J. C. Baygents and D. A. Saville, “The circulation produced in a drop by an electric field: A high field strength electrokinetic model,” in *AIP Conference Proceedings*, 1990, vol. 197, pp. 7–17.
- [23] O. Vizika and D. A. Saville, “The electrohydrodynamic deformation of drops suspended in liquids in steady and oscillatory electric fields,” *J. Fluid Mech.*, vol. 239, no. 1, pp. 1–21, 1992.
- [24] W. A. Macky, “Some Investigations on the Deformation and Breaking of Water Drops in Strong Electric Fields,” *Proc. R. Soc. A Math. Phys. Eng. Sci.*, vol. 133, no. 822, pp. 565–587, Oct. 1931.
- [25] C. T. O’Konski and H. C. Thacher, “The Distortion of Aerosol Droplets by an Electric Field,” *J. Phys. Chem.*, vol. 57, no. 9, pp. 955–958, Sep. 1953.
- [26] O. A. Basaran, T. C. Scott, and C. H. Byers, “Drop oscillations in liquid-liquid systems,” *AIChE J.*, vol. 35, no. 8, pp. 1263–1270, Aug. 1989.
- [27] N. A. Pelekasis, J. A. Tsamopoulos, and G. D. Manolis, “Equilibrium shapes and stability of charged and conducting drops,” *Phys. Fluids A Fluid Dyn.*, vol. 2, no. 8, pp. 1328–1340, Aug. 1990.

- [28] J. R. Carruthers and L. R. Testardi, "Materials Processing in the Reduced-Gravity Environment of Space," *Annu. Rev. Mater. Sci.*, vol. 13, no. 1, pp. 247–278, Aug. 1983.
- [29] M. Mutoh, "A study on the drop formation of continuous liquid jet by an electrical method," *Phys. Fluids*, vol. 14, no. 4, pp. 1380–1388, Apr. 2002.
- [30] J. Zeng and F. T. Korsmeyer, "Principles of droplet EHDs for lab-on-a-chip," *Lab Chip*, vol. 4, no. 4, pp. 265–277, 2004.
- [31] J.-W. Ha and S.-M. Yang, "Rheological responses of oil-in-oil emulsions in an electric field," *J. Rheol. (N. Y. N. Y.)*, vol. 44, no. 2, pp. 235–256, Mar. 2000.
- [32] J. R. Melcher and G. I. Taylor, "Electrohydrodynamics: A Review of the Role of Interfacial Shear Stresses," *Annu. Rev. Fluid Mech.*, vol. 1, no. 1, pp. 111–146, Jan. 1969.
- [33] D. A. Saville, "ELECTROHYDRODYNAMICS: The Taylor-Melcher Leaky Dielectric Model," *Annu. Rev. Fluid Mech.*, vol. 29, no. 1, pp. 27–64, Jan. 1997.
- [34] P. A. Arp, R. T. Foister, and S. G. Mason, "Some electrohydrodynamic effects in fluid dispersions," *Adv. Colloid Interface Sci.*, vol. 12, no. 4, pp. 295–356, 1980.
- [35] Stéphane Popinet, "An accurate adaptive solver for surface-tension-driven interfacial flows," *J. Comput. Phys.*, vol. 228, pp. 5838–5866, 2009.
- [36] S. Popinet, "Gerris: a tree-based adaptive solver for the incompressible Euler equations in complex geometries," *J. Comput. Phys.*, vol. 190, no. 2, pp. 572–600, Sep. 2003.
- [37] B. J. K. D. and Z. C., "A Continuum Method for Modeling Surface Tension," *J. Comput. Phys.*, vol. 100, pp. 335–354, 1992.
- [38] D. Bhaga and M. E. Weber, "Bubbles in viscous liquids: Shapes, wakes and velocities," *J. Fluid Mech.*, vol. 105, pp. 61–85, 1981.
- [39] M. K. Tripathi, "Rising bubbles and falling drops," *iith.ac.in*, no. February, 2015.
- [40] J. Hua, L. K. Lim, and C.-H. Wang, "Numerical simulation of deformation/motion of a drop suspended in viscous liquids under influence of steady electric fields," *Phys. Fluids*, vol. 20, no. 11, p. 113302, Nov. 2008.
- [41] "Studies in electrohydrodynamics. I. The circulation produced in a drop by an electric field," *Proc. R. Soc. London. Ser. A. Math. Phys. Sci.*, vol. 291, no. 1425, pp. 159–166, Apr. 1966.
- [42] G. Tomar *et al.*, "Two-phase electrohydrodynamic simulations using a volume-of-fluid approach," *J. Comput. Phys.*, vol. 227, no. 2, pp. 1267–1285, Dec. 2007.

- [43] J. D. Sherwood, "Breakup of fluid droplets in electric and magnetic fields," *J. Fluid Mech.*, vol. 188, pp. 133–146, 1988.
- [44] J. Han and G. Tryggvason, "Secondary breakup of axisymmetric liquid drops. I. Acceleration by a constant body force," *Phys. Fluids*, vol. 11, no. 12, pp. 3650–3667, Dec. 1999.
- [45] X.-K. Cao, Z.-G. Sun, W.-F. Li, H.-F. Liu, and Z.-H. Yu, "A new breakup regime of liquid drops identified in a continuous and uniform air jet flow," *Phys. Fluids*, vol. 19, no. 5, p. 057103, May 2007.
- [46] N. BREMOND and E. VILLERMAUX, "Bursting thin liquid films," *J. Fluid Mech.*, vol. 524, pp. 121–130, Feb. 2005.
- [47] R. Subramanian and M. A. Jog, "Enhancement of Heat Transfer by an Electric Field for a Drop Translating at Intermediate Reynolds Number," *J. Heat Transfer*, vol. 127, no. 10, p. 1087, Oct. 2005.
- [48] M. Chipot and P. Quittner, *Handbook of Differential Equations: Stationary Partial Differential Equations, Volume 1*. Elsevier North Holland, 2004.
- [49] J. Doshi and D. H. Reneker, "Electrospinning process and applications of electrospun fibers," *J. Electrostat.*, vol. 35, no. 2–3, pp. 151–160, Aug. 1995.

VITA

ESMAIL GHASEMISAHEBI

Born, Sary, Iran

- 2004–2009 B.Sc., Mechanical Engineering
University of Mazandaran
Babol, Iran
- 2011–2013 M.Sc, Mechanical Engineering
University of Idaho
Moscow, Idaho
- 2015–2017 Engineering Management
Florida International University
Miami, Florida
- 2013–2019 Ph.D. Mechanical Engineering
Florida International University
Miami, Florida
- Teaching Assistant
Florida International University
Miami, Florida

PUBLICATIONS AND PRESENTATIONS

Esmail Ghasemisahebi: Entropy generation in transitional boundary layers, LAP LAMBERT Academic Publishing, 2013.

E Ghasemi, H Bararnia, S Soleimanikutanaei, CX Lin, Simulation of deformation and fragmentation of a falling drop under electric field, Powder Technology 325(2018)301-308.

E Ghasemi, H Bararnia, S Soleimanikutanaei, CX Lin, Direct numerical simulation and analytical modeling of electrically induced multiphase flow, International Journal of Mechanical Sciences, 142–143 (2018) 397-406.

E Ghasemi, S Soleimani, CX Lin, Secondary reactions of turbulent reacting flows over a film-cooled surface, International Communications in Heat and Mass Transfer 55, 2014,93-101.

E Ghasemi, S Soleimani, CX Lin, RANS simulation of methane-air burner using local extinction approach within eddy dissipation concept by OpenFOAM, International

Communications in Heat and Mass Transfer 54,2014, 96-102.

E.Ghasemi, D. M. McEligot, K. Nolan, J. Crepeau, A. Siahpush, R. S. Budwig, Effects of adverse and favorable pressure gradients on entropy generation in a transitional boundary layer region under the influence of freestream turbulence, *Int. J. Heat. Mass. Transfer* , 77 (2014) 475-488 .

E.Ghasemi, D. M. McEligot, K. Nolan, J. Crepeau, A.Tokuhiro, R. S. Budwig, Entropy generation in transitional boundary layer region under the influence of freestream turbulence using transitional RANS models and DNS, *Int. Comm. Heat. Mass. Transfer* , 41 (2013) 10–16 .

E. Ghasemi, Soheil Soleimani,C.X. Lin, Secondary reactions of turbulent reacting flows over a film-cooled surface using OpenFOAM, doi:10.2514/6.2014-2257.

E. Ghasemi, S Soleimani, CX Lin, Control of turbulent combustion flow inside a gas turbine combustion chamber using plasma actuators, *ASME Power and Energy Conference 2015*.

E. Ghasemi, et al, Numerical Study of Transport Membrane Condenser Heat Exchangers". 8 (2016), IMECE2016-67882.

E. Ghasemi, et al, Study of falling droplets under effects of electric field". IMECE, 2017, Tampa, FL.

E. Ghasemi. et al. Near wall deformation and dynamics of falling droplets under the effect of electric field. IMECE, 2017, Tampa, FL.

E. Ghasemi. et al. Modeling of Shell and Tube Transport Membrane Condenser Heat Exchangers in Low Grade Waste and Heat and Water Recovery Applications. 8 (2016), IMECE2016-67906